

**Evolution of Adiabatic Shear Bands in
High Strength Steels at High Shear-Strain Rates**

by

Elvis Cepus

A thesis of the University of Manitoba

in fulfillment of the

thesis requirement for the degree of

Master of Science

in

Mechanical Engineering

Winnipeg, Manitoba, Canada 1995

© Elvis Cepus 1995



National Library
of Canada

Acquisitions and
Bibliographic Services Branch

395 Wellington Street
Ottawa, Ontario
K1A 0N4

Bibliothèque nationale
du Canada

Direction des acquisitions et
des services bibliographiques

395, rue Wellington
Ottawa (Ontario)
K1A 0N4

Your file *Votre référence*

Our file *Notre référence*

The author has granted an irrevocable non-exclusive licence allowing the National Library of Canada to reproduce, loan, distribute or sell copies of his/her thesis by any means and in any form or format, making this thesis available to interested persons.

L'auteur a accordé une licence irrévocable et non exclusive permettant à la Bibliothèque nationale du Canada de reproduire, prêter, distribuer ou vendre des copies de sa thèse de quelque manière et sous quelque forme que ce soit pour mettre des exemplaires de cette thèse à la disposition des personnes intéressées.

The author retains ownership of the copyright in his/her thesis. Neither the thesis nor substantial extracts from it may be printed or otherwise reproduced without his/her permission.

L'auteur conserve la propriété du droit d'auteur qui protège sa thèse. Ni la thèse ni des extraits substantiels de celle-ci ne doivent être imprimés ou autrement reproduits sans son autorisation.

ISBN 0-612-13016-9

Canada

Name *Evolution of Adiabatic Shear Bands in High Strength Steels at High Shear-Strain Rates*

Dissertation Abstracts International is arranged by broad, general subject categories. Please select the one subject which most nearly describes the content of your dissertation. Enter the corresponding four-digit code in the spaces provided.

Metallurgy

0743

U·M·I

SUBJECT TERM

SUBJECT CODE

Subject Categories

THE HUMANITIES AND SOCIAL SCIENCES

COMMUNICATIONS AND THE ARTS

Architecture	0729
Art History	0377
Cinema	0900
Dance	0378
Fine Arts	0357
Information Science	0723
Journalism	0391
Library Science	0399
Mass Communications	0708
Music	0413
Speech Communication	0459
Theater	0465

EDUCATION

General	0515
Administration	0514
Adult and Continuing	0516
Agricultural	0517
Art	0273
Bilingual and Multicultural	0282
Business	0688
Community College	0275
Curriculum and Instruction	0727
Early Childhood	0518
Elementary	0524
Finance	0277
Guidance and Counseling	0519
Health	0680
Higher	0745
History of	0520
Home Economics	0278
Industrial	0521
Language and Literature	0279
Mathematics	0280
Music	0522
Philosophy of	0998
Physical	0523

Psychology	0525
Reading	0535
Religious	0527
Sciences	0714
Secondary	0533
Social Sciences	0534
Sociology of	0340
Special	0529
Teacher Training	0530
Technology	0710
Tests and Measurements	0288
Vocational	0747

LANGUAGE, LITERATURE AND LINGUISTICS

Language	
General	0679
Ancient	0289
Linguistics	0290
Modern	0291
Literature	
General	0401
Classical	0294
Comparative	0295
Medieval	0297
Modern	0298
African	0316
American	0591
Asian	0305
Canadian (English)	0352
Canadian (French)	0355
English	0593
Germanic	0311
Latin American	0312
Middle Eastern	0315
Romance	0313
Slavic and East European	0314

PHILOSOPHY, RELIGION AND THEOLOGY

Philosophy	0422
Religion	
General	0318
Biblical Studies	0321
Clergy	0319
History of	0320
Philosophy of	0322
Theology	0469

SOCIAL SCIENCES

American Studies	0323
Anthropology	
Archaeology	0324
Cultural	0326
Physical	0327
Business Administration	
General	0310
Accounting	0272
Banking	0770
Management	0454
Marketing	0338
Canadian Studies	0385
Economics	
General	0501
Agricultural	0503
Commerce-Business	0505
Finance	0508
History	0509
Labor	0510
Theory	0511
Folklore	0358
Geography	0366
Gerontology	0351
History	
General	0578

Ancient	0579
Medieval	0581
Modern	0582
Black	0328
African	0331
Asia, Australia and Oceania	0332
Canadian	0334
European	0335
Latin American	0336
Middle Eastern	0333
United States	0337
History of Science	0585
Law	0398
Political Science	
General	0615
International Law and Relations	0616
Public Administration	0617
Recreation	0814
Social Work	0452
Sociology	
General	0626
Criminology and Penology	0627
Demography	0938
Ethnic and Racial Studies	0631
Individual and Family Studies	0628
Industrial and Labor Relations	0629
Public and Social Welfare	0630
Social Structure and Development	0700
Theory and Methods	0344
Transportation	0709
Urban and Regional Planning	0999
Women's Studies	0453

THE SCIENCES AND ENGINEERING

BIOLOGICAL SCIENCES

Agriculture	
General	0473
Agronomy	0285
Animal Culture and Nutrition	0475
Animal Pathology	0476
Food Science and Technology	0359
Forestry and Wildlife	0478
Plant Culture	0479
Plant Pathology	0480
Plant Physiology	0817
Range Management	0777
Wood Technology	0746
Biology	
General	0306
Anatomy	0287
Biostatistics	0308
Botany	0309
Cell	0379
Ecology	0329
Entomology	0353
Genetics	0369
Limnology	0793
Microbiology	0410
Molecular	0307
Neuroscience	0317
Oceanography	0416
Physiology	0433
Radiation	0821
Veterinary Science	0778
Zoology	0472
Biophysics	
General	0786
Medical	0760

EARTH SCIENCES

Biogeochemistry	0425
Geochemistry	0996

Geodesy	0370
Geology	0372
Geophysics	0373
Hydrology	0388
Mineralogy	0411
Paleobotany	0345
Paleoecology	0426
Paleontology	0418
Paleozoology	0985
Palynology	0427
Physical Geography	0368
Physical Oceanography	0415

HEALTH AND ENVIRONMENTAL SCIENCES

Environmental Sciences	0768
Health Sciences	
General	0566
Audiology	0300
Chemotherapy	0992
Dentistry	0567
Education	0350
Hospital Management	0769
Human Development	0758
Immunology	0982
Medicine and Surgery	0564
Mental Health	0347
Nursing	0569
Nutrition	0570
Obstetrics and Gynecology	0380
Occupational Health and Therapy	0354
Ophthalmology	0381
Pathology	0571
Pharmacology	0419
Pharmacy	0572
Physical Therapy	0382
Public Health	0573
Radiology	0574
Recreation	0575

Speech Pathology	0460
Toxicology	0383
Home Economics	0386

PHYSICAL SCIENCES

Pure Sciences	
Chemistry	
General	0485
Agricultural	0749
Analytical	0486
Biochemistry	0487
Inorganic	0488
Nuclear	0738
Organic	0490
Pharmaceutical	0491
Physical	0494
Polymer	0495
Radiation	0754
Mathematics	0405
Physics	
General	0605
Acoustics	0986
Astronomy and Astrophysics	0606
Atmospheric Science	0608
Atomic	0748
Electronics and Electricity	0607
Elementary Particles and High Energy	0798
Fluid and Plasma	0759
Molecular	0609
Nuclear	0610
Optics	0752
Radiation	0756
Solid State	0611
Statistics	0463

Applied Sciences

Applied Mechanics	0346
Computer Science	0984

Engineering	
General	0537
Aerospace	0538
Agricultural	0539
Automotive	0540
Biomedical	0541
Chemical	0542
Civil	0543
Electronics and Electrical	0544
Heat and Thermodynamics	0348
Hydraulic	0545
Industrial	0546
Marine	0547
Materials Science	0794
Mechanical	0548
Metallurgy	0743
Mining	0551
Nuclear	0552
Packaging	0549
Petroleum	0765
Sanitary and Municipal	0554
System Science	0790
Geotechnology	0428
Operations Research	0796
Plastics Technology	0795
Textile Technology	0994

PSYCHOLOGY

General	0621
Behavioral	0384
Clinical	0622
Developmental	0620
Experimental	0623
Industrial	0624
Personality	0625
Physiological	0989
Psychobiology	0349
Psychometrics	0632
Social	0451



**EVOLUTION OF ADIABATIC SHEAR BANDS IN HIGH STRENGTH
STEELS AT HIGH SHEAR-STRAIN RATES**

BY

ELVIS CEPUS

**A Thesis submitted to the Faculty of Graduate Studies of the University of Manitoba
in partial fulfillment of the requirements of the degree of**

MASTER OF SCIENCE

© 1995

**Permission has been granted to the LIBRARY OF THE UNIVERSITY OF MANITOBA
to lend or sell copies of this thesis, to the NATIONAL LIBRARY OF CANADA to
microfilm this thesis and to lend or sell copies of the film, and LIBRARY
MICROFILMS to publish an abstract of this thesis.**

..

**The author reserves other publication rights, and neither the thesis nor extensive
extracts from it may be printed or other-wise reproduced without the author's written
permission.**

"To travel hopefully is a better thing than to arrive, and the true success is to labour."

Robert Louis Stevenson

"Who is the happier man, he who has braved the storm of life and lived, or he who has stayed securely on shore and merely existed?"

Hunter S. Thompson

"Imagination is more important than knowledge."

Albert Einstein

ACKNOWLEDGMENTS

Patience was a commodity required in massive abundance in order for this work to final come to fruition. However much I may try, I can never express adequately the debt of gratitude I owe to a great many people. To my family, for the constant encouragement and occasional push which initiated the final effort in this thesis - thank you. To my present employer Steve Bagaric, for gracefully granting me the time and resources required that allowed me to contemplate finishing - a more understanding employer does not exist. And finally, to Dr. Bassim for having the infinite patience and tolerance that mentoring any thesis requires, in addition to shouldering the extra strain of guiding me to my completion in absentia. His guidance and tutelage was, and will forever be, a source of incalculable experience. Thank you.

While working on this thesis many people played a beneficial role in its final outcome. To all the metallurgists that taught me; Dr. Cahoon, Dr. Chaturvedi and Dr. Tandon. Thank you for collectively introducing me to a fascinating field of study. To the metallurgist who inspired me, Dr. Spiro Yannacopoulos, you just *may* be ultimately responsible for this entire adventure! If I could have a brother, I would hope him to be like you. To the technicians Don Mardis, Jon VanDorp and Fred Kapitoler. Excellent help and good friends. Dr. C.D. Liu for his pleasant and knowledgeable outlook, helping me see, even set-back, in a better light. Dr. Ken Westra, who showed me what I should expect from the *experience*. Interesting people are hard to come by - harder still are some of the titles you suggested I read. Thank you to everyone. If I failed to mention you it was due to my own ignorance, not a lack of gratitude.

I closing, thank you to the Natural Sciences and Engineering Research Council (NSERC) for their support and interest during this project.

TABLE OF CONTENTS

Acknowledgments	iii
Table of Contents	iv
List of Figures	v
List of Tables.....	vi
Nomenclature	vii
Abstract.....	viii
Chapter 1 Literature Review	1
1.1. Objective of the Present Research.....	1
1.2. Introduction	1
1.3. Mechanical Behavior at High Strain Rates	2
1.3.1. Introduction	2
1.3.2. The Effect of Strain Rate on Material Behavior	3
1.3.3. The Load Instability Model	7
1.3.4. The Shear Band Width Models.....	10
1.3.5. Clifton Shear Band Analysis	14
1.3.6. Dynamic stress strain relationships	16

1.4. Material Behavior at High Strain Rates	20
1.4.1. Introduction.....	20
1.4.2. Quasi-Static Versus Dynamic Deformation	20
1.4.3. The Deformed Shear Band	22
1.4.4. The Transformed Shear Band.....	23
1.4.5. Formation of a Transformed Shear Band	25
1.4.6. Temperature Requirements	27
1.4.7. Microstructure and Morphology of the Transformed Shear Band ...	28
1.5. Various High Strain Rate Techniques	36
1.5.1. Rod Impact.....	37
1.5.2. Expanding Ring	37
1.5.3. Flyer Plate Impact.....	38
1.5.4. Torsional Impact.....	38
Chapter 2 Design and Implementation of a Torsional Split-Hopkinson Bar.....	39
2.1. Introduction	39
2.2. Hopkinson Bar Theory	39
2.3. Design of a Split-Hopkinson Bar	47

2.3.1.	The Loading System	47
2.3.2.	Specimen Mount	49
2.3.3.	Strain Gage Placement	51
2.3.3.1.	Wave Characteristic Diagram.....	51
2.3.4.	Criteria For the Design of the Load Length	54
2.3.4.1.	Velocity of the Impulse.....	54
2.3.4.2.	Specimen Fracture Criteria	58
2.3.5.	The Clamp/Release Mechanism	61
2.3.6.	Final Mechanical Design.....	65
2.4.	Electronic Instrumentation / Data Acquisition.....	68
2.4.1.	Equipment Calibration.....	70
2.5.	Calculating Stress, Strain and Strain Rate	73
2.5.1.	Theoretical Limits on Strain Rate	78
2.5.2.	Practical Limits on Strain Rate	80
Chapter 3	Procedure For Evaluation	83
3.1.	Experimental Procedure.....	83
3.1.1.	Specimen Heat Treatment	85

3.1.2. Experimental Apparatus Instructions	88
3.1.3. Low Temperature Testing Procedure	90
3.1.4. Varying Experiment Strain Rates.....	91
3.1.5. Post-Test Specimen Analysis Preparation	91
Chapter 4 Validation and Experimental Results.....	95
4.1. Equipment Functionality	95
4.2. Pre-Test Specimen Microstructure.....	95
4.3. Stress - Strain Behavior.....	101
4.4. Room Temperature Dynamic Torsion Tests.....	101
4.4.1. Stress Strain Curves	101
4.4.2. Mechanical Properties	107
4.4.3. Morphology of the ASB Region.....	110
4.4.3.1. Unetched Specimens.....	110
4.4.3.2. Etched Specimens.....	115
4.5. Low Temperature Dynamic Torsion Tests.....	119
4.5.1. Stress Strain Curves.....	119
4.5.2. Mechanical Properties	119

4.5.3. Morphology of the ASB Region.....	124
4.5.3.1. Unetched Specimens.....	124
4.5.3.2. Etched Specimens.....	124
Chapter 5 Discussion of Results.....	132
5.1. Equipment Appraisal	132
5.2. Yield Characteristics.....	132
5.3. Heat Treatment/Microstructural Effects.....	133
5.3.1. Room Temperature Tests	133
5.3.2. Low Temperature Tests	137
5.4. Shear Band Characteristics	139
5.5. Constitutive Modeling	143
Chapter 6Conclusions	147
References	149

LIST OF FIGURES

Figure 1: Effect of Strain Rate on Strength - Mild Steel [16].	4
Figure 2: Effect of Strain Rate on Strength - Structural Steel [17].	4
Figure 3: Stress-Strain Curves for HY-100 steel at Room Temperature [11]	6
Figure 4: Illustration of equation 17 [9].	19
Figure 5: Uniform elastic-plastic deformation in torsion [82].	21
Figure 6: High-speed photograph of ASB formation [23].	21
Figure 7: Example of a white etched ASB optical micrograph [23].	24
Figure 8: Thermal diffusivity vs. Critical longitudinal strain, showing material parameters influence on shear band type [21].	26
Figure 9: Various configurations of the Hopkinson bar [76].	42
Figure 10: Typical set-up of a torsional Hopkinson bar [76].	43
Figure 11: Behavior of the loading and unloading pulses upon clamp release.	48
Figure 12: The jacking mechanism.	48
Figure 13: Specimen slot at end of the bars.	50
Figure 14: Photo of specimen and specimen slot.	50
Figure 15: Lagrangian or time-displacement diagram superposed on a typical split-Hopkinson set-up [73].	53

Figure 16: Tracking the wave inversion effect in order to calculate shear wave velocity.	56
Figure 17: Transmitted pulse trace.	57
Figure 18: Sketch of the clamping mechanism.	62
Figure 19: Photograph of the clamping system.	63
Figure 20: Force diagram of the clamping mechanism.	65
Figure 21: Sketch of the Hopkinson bar set-up.	66
Figure 22: Enlarged view of the Hopkinson bar - loading side.	67
Figure 23: Calibration Curves for the Hopkinson bar.	72
Figure 24: The Incident, Reflected and Transmitted Pulses.	74
Figure 25: Strain Rate vs. Test Time.	74
Figure 26: Specimen diagram. Dimensions in mm.	84
Figure 27: Illustration of the γ angle on a post-test specimen.	93
Figure 28: SEM Micrograph of Specimen A.	98
Figure 29: SEM Micrograph of Specimen B.	98
Figure 30: SEM Micrograph of Specimen C.	99
Figure 31: SEM Micrograph of Specimen D.	99
Figure 32: SEM Micrograph of Specimen E.	100

Figure 33: Typical Shape for a Stress Strain Curve [82].	102
Figure 34: Stress - Strain Curve for A.	104
Figure 35: Stress - Strain Curve for B.	104
Figure 36: Stress - Strain Curve for C.	105
Figure 37: Stress - Strain Curve for D.	105
Figure 38: Stress - Strain Curve for E.	106
Figure 39: Stress - Strain Curve for all 5 Room Temperature Curves.	106
Figure 40: The effect of Specimen hardness on Failure Strain	108
Figure 41: The effect of yield strength on the shear band width, at room temperature.	109
Figure 42: The unetched ASB for A.	112
Figure 43: The unetched ASB for B.	112
Figure 44: The unetched ASB for C.	113
Figure 45: The unetched ASB for D.	113
Figure 46: The unetched ASB for E.	114
Figure 47: The etched ASB for A.	116
Figure 48: The etched ASB for B.	116
Figure 49: The etched ASB for C.	117

Figure 50: The etched ASB for D.	117
Figure 51: The etched ASB for E.....	118
Figure 52: Stress - Strain Curve for A, -30°C.....	121
Figure 53: Stress - Strain Curve for B, -30°C.....	121
Figure 54: Stress - Strain Curve for C, -30°C.....	122
Figure 55: Stress - Strain Curve for D, -30°C.....	122
Figure 56: Stress - Strain Curve for E, -30°C.....	123
Figure 57: Stress - Strain Curves for all 5 samples, -30°C	123
Figure 58: The unetched ASB for A, -30°C.	126
Figure 59: The unetched ASB for B, -30°C.....	126
Figure 60: The unetched ASB for C, -30°C.....	127
Figure 61: The unetched ASB for D, -30°C.	127
Figure 62: The unetched ASB for E, -30°C.....	128
Figure 63: The etched ASB for A, -30°C.	129
Figure 64: The etched ASB for B, -30°C.	129
Figure 65: The etched ASB for C, -30°C.	130
Figure 66: The etched ASB for D, -30°C.	130

Figure 67: The etched ASB for E, -30°C.....	131
Figure 68: The effect of tempering temperature on shear band width.....	134
Figure 69: The effect of hardness on shear band width.	135
Figure 70: Room temperature correlation with Dodd and Bai's model.	145
Figure 71: -30°C correlation with Dodd and Bai	146

LIST OF TABLES

Table 1: Physical properties of AISI 4340 steel [57].....	11
Table 2. Composition of SPS-Plus and AISI 4340, wt %	84
Table 3: Pre-Test Statistical Data on Test Samples.....	87
Table 4: A complete summary of the room temperature data accumulated.....	107
Table 5: A complete summary of the -30°C data accumulated	119
Table 6: Mean and standard deviation values for room temperature and -30°X data	125
Table 7: Data used for calculation of the Shear Band Width.....	144

NOMENCLATURE

γ = shear strain [Mpa]

τ = shear stress [MPa]

β = the fraction of heat that appears as work [dimensionless]

ρ = density of the material [kg/m^3]

c = specific heat capacity [J/kgK]

J = mechanical equivalent of heat [J]

B = strength coefficient [kPa]

T = temperature [K]

$\dot{\gamma}^{OP}$ = the homogeneous plastic strain rate

$1/\xi$ = the wavelength of the inhomogeneity

λ = thermal conductivity

$\partial\tau/\partial T$ = variation of flow stress with temperature at a constant plastic γ and $\dot{\gamma}$

τ_r = represents the resistance of the material to plastic deformation

$\partial\tau_r/\partial\gamma_p$ = strain hardening rate

ABSTRACT

The high strain rate properties of materials are of great importance in studies dealing with high speed manufacturing or machining [1-3]. However, the most dominant proponent of high strain rate studies remains the military due to the fact that ballistic impact of airborne projectiles, with armor penetration is a very common form of high strain rate deformation. The interest is due to the very high costs associated with military equipment and the danger to military personnel within these vehicles.

Under sufficiently high rates of deformation, the failure mode is markedly different from that found in quasi-static studies. Impact loading at a strain rate in the range of 500 1/s practically guarantees that an adiabatic shear band (ASB), or an immensely deformed, highly localized region of deformation, will be formed. The reason for this will be discussed later, but suffice it to say that upon the formation of the ASB the material can be considered to have undergone failure for all intents and purposes.

Typically, studies of high strain-rate deformation belong to one of two schools of thought; the mechanical approach or the metallurgical approach. As their names imply, the mechanical approach is concerned mainly with the material properties under high strain rates, including, the stress-strain curve. The metallurgical approach concerns itself with why the material behaves as it does, and directs a majority of its attention towards analysis of the adiabatic shear band.

In the present study a torsionally modified split-Hopkinson bar was designed, built and tested. As a part of the equipment validation, two series of experiments were conducted; room temperature and -30°C. The experiments were done on SPS-Plus steel

at five different heat treatment conditions and hardnesses. Analysis was then conducted to determine the relationship between selected material parameters and material hardness.

It is shown in this thesis, that a reliable and reproducible means of obtaining high strain rate torsional tests has been developed. Moreover, it has been shown that for quenched and tempered steels the size of the adiabatic shear band is directly related to the strength of the material. It has been shown, for example, that higher relative tempering temperatures result in the formation of a wider adiabatic shear band during high strain rate testing than was observed in samples tempered at a lower temperature.

All samples except the 640°C tempered steels displayed very ductile deformation surfaces and easily provided information from which local strain could be calculated. The transformed shear bands in the 640°C tempered specimen formed transformed shear bands which were discretely bounded by the matrix and could not provide information pertaining to local strain.

CHAPTER 1

LITERATURE REVIEW

1.1. OBJECTIVE OF THE PRESENT RESEARCH

The literature review covers a wide range of details concerned high strain testing procedures and related material phenomena. With the information presented a torsionally modified split-Hopkinson bar design was chosen and executed based on its effectiveness and reliability in the production of high strain rate data and post-mortem samples. To verify the effectiveness of the design five heat treatments of high-strength steel were tested and analyzed. In addition, the resulting ASB formations in each of the tested high strain rate samples was to be studied.

1.2. INTRODUCTION

The behavior of materials, specifically steels, under high rates of strain is markedly differently than that of materials which have been quasi-statically deformed. The three most recognizable differences are as follows. Firstly under high strain rates, mechanical properties such as strength and ductility undergo changes and are reflected in the stress-strain curve. Secondly, the failure mode nullifies any aspect of quasi-static analysis or conventional elastic-plastic mechanics that may apply to low strain rate material deformation. And thirdly, the formation of one of two types of adiabatic shear band takes place.

There are a variety of methods used to obtain the high strain rates necessary to realize the modified mechanical and material properties mentioned above, some of which will be discussed later in this chapter.

The first goal of this review is to cite typical mechanical and material performance characteristics at high rates of strain such that the experimental results and observations acquired in this thesis may be compared and validated. The second goal is to provide a rationale for having chosen the torsional configuration of the split-Hopkinson or Kolsky bar.

1.3. MECHANICAL BEHAVIOR AT HIGH STRAIN RATES

1.3.1. Introduction

Research in the processes involving shear band formation can be categorized into two schools of thought, the mechanical / macroscopic interests and the metallurgical / microstructural interests. This section includes a brief review of both of these theories and the type of data produced by the high strain rate apparatus.

Previously conducted research has shown that a few of the more significant determining factors in the susceptibility and type of shear banding that a material exhibits are the following; the strain rate exponent, strain rate sensitivity, work hardening coefficient, thermal conductivity, material hardness, microstructure and content of imperfections such as inclusions [5-15, 24, 25, 30, 36, 61,]. The significance of most of the aforementioned properties or parameters are aptly illustrated through the role each plays in their respective constitutive equation. In addition, the

constitutive equations serve to identify critical points in the stress-strain behavior during high strain-rate loading.

1.3.2. The Effect of Strain Rate on Material Behavior

In the study of steel at high rates of strain the most obvious differences as compared to quasi-static testing are the mechanical properties portrayed by the material. This is the reason for wanting an effective and consistent means of acquiring and interpreting high strain rate data.

The marked differences are best illustrated in previously published research. Lewis and Campbell [16] show rather clearly the effects of altering strain rate when testing EN2A type mild steel, Figure 1. Figure 2 shows the strain-rate effect for various structural steels.

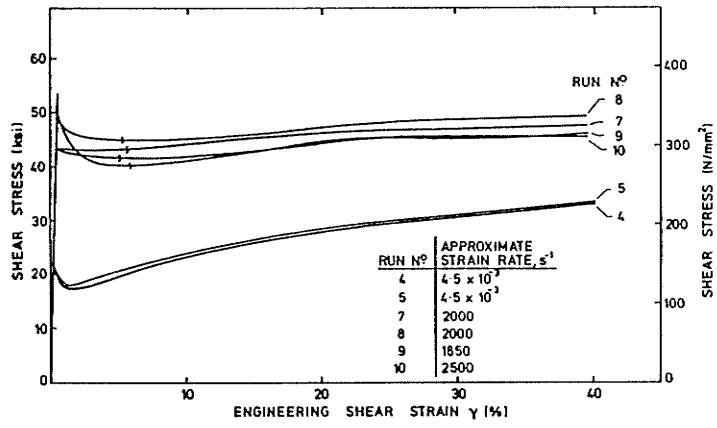


Figure 1: Effect of Strain Rate on Strength - Mild Steel [16].

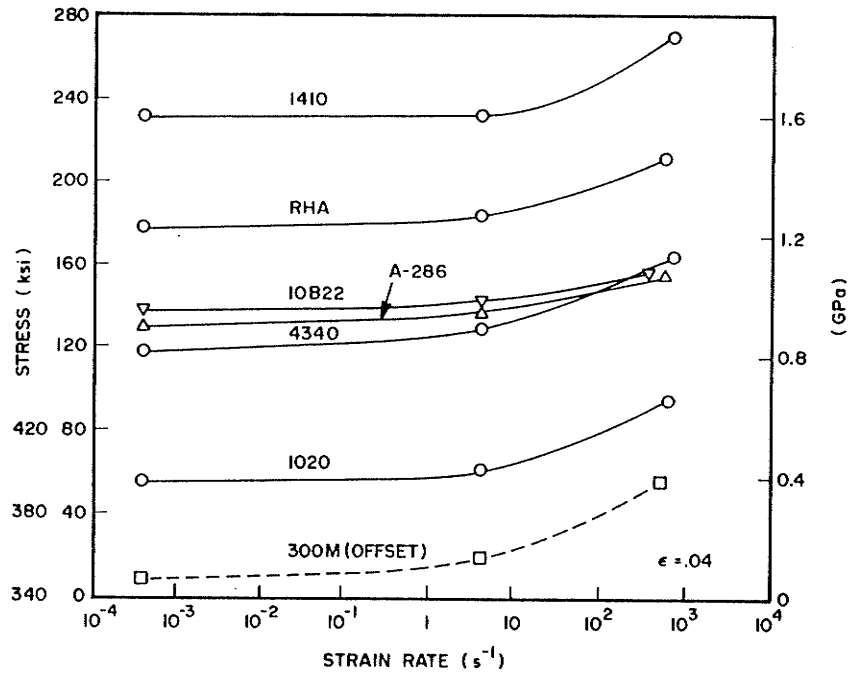


Figure 2: Effect of Strain Rate on Strength - Structural Steel [17].

As shown, In Figures 3 and 2 the lower strain rate tested material is less than 40% as strong as that studied at a higher strain rate tested samples. Though slight changes in the high strain rate range of the test results in a slight shift of the curves, the initial jump from the quasi-static to the dynamic regime represents the most dramatic difference. A second, and perhaps more subtle, difference is the change from the isothermal to the adiabatic deformation process as illustrated in Figure 3 and in [17, 18]. Close observation reveals that for the low $\dot{\gamma}$ isothermal curves there is a steady increase in the strength of the material, whereas for the high $\dot{\gamma}$ adiabatic curves there is a slight but noticeable drop in material strength. This is because at low strain rates the rate of heat generation is far less than the rate of heat dissipation, and hence the sample stays at essentially room temperature - being tested isothermally. When deformed at low strain rates the well understood strengthening mechanisms common to steel such as strain hardening dominate and there is an increase in strength. However, at high rates of strain the rate of heat generation is far greater than the rate of dissipation. This results in an overall material softening due to thermal effects and ultimately localized failure due to the formation of shear bands, as will be discussed later. The end result is the softening displayed by the stress-strain curve.

Another effect much more clearly illustrated in [11], is a reduction in ductility at high strain rates. Figure 3 shows this effect for HY-100 steel. The most likely reason for this is due to the fact that for steels deformed at high strain rates the majority of the deformation takes place over a very narrow region of material which does not have the same capacity for deformation as the entire gauge section, regardless of the different deformation mechanisms which may be in effect within the adiabatic shear band.

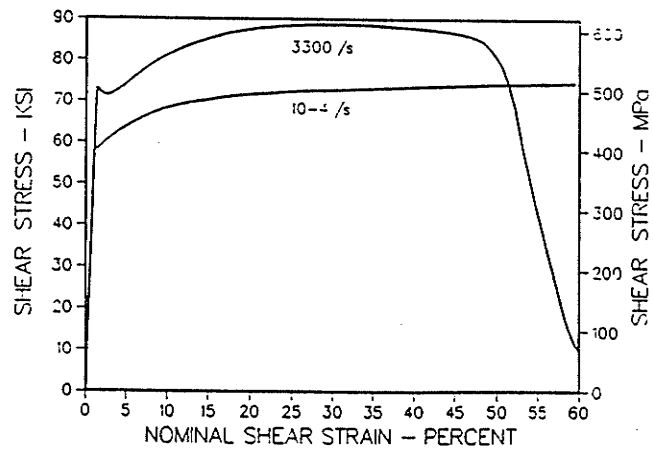


Figure 3: Stress-Strain Curves for HY-100 steel at Room Temperature. [11]

These results indicate that the behavioral characteristics of steels (regardless of specific type) at high rates of strain are significantly different from those observed during low strain rate studies and warrant a closer investigation using appropriately constructed equipment.

1.3.3. The Load Instability Model

The most commonly used model for load instability studies in dynamic shear was first introduced by Recht in 1964 [60] based on Baron's mechanical equation of state [19] from 1965. Recht proposed that "catastrophic shear", as he referred to it, would occur at the point in the dynamic stress-strain curve where its slope, $(d\sigma/d\epsilon)_a$ is equal to zero. The equation was originally intended as a general model for steel under tensile loading but is easily modified for shear analysis, and starts as follows;

$$\frac{d\tau}{d\gamma} = \left(\frac{\partial \tau}{\partial \gamma} \right)_{T, \dot{\gamma}} + \left(\frac{\partial \tau}{\partial \dot{\gamma}} \right)_{T, \gamma} \frac{d\dot{\gamma}}{d\gamma} + \left(\frac{\partial \tau}{\partial T} \right)_{\gamma, \dot{\gamma}} \frac{dT}{d\gamma} \quad (1)$$

Where: τ = shear stress

γ = shear strain

T = temperature

Since the point of interest is where in the stress-strain curve has a slope equal to zero, the first term may be set equal to zero. Also, the strain rate is assumed to be generally constant through the deformation process and can also be left out. The resulting equation is then;

$$\frac{d\tau}{d\gamma} = -\left(\frac{\partial\tau}{\partial T}\right)_{\gamma,\dot{\gamma}} \frac{dT}{d\gamma} \quad (2)$$

From this point in the derivation onwards, many different interpretations and assumptions have been made. In 1973 Culver used Barons [19];

$$\frac{dT}{d\gamma} = \left(\frac{\beta}{\rho c J}\right) B \gamma^n \quad (3)$$

and the limiting strain as a function of the work hardening exponent;

$$\tau = B \gamma^n \quad (4)$$

Where: β = the fraction of heat that appears as work [dimensionless]

ρ = density of the material [kg/m^3]

c = specific heat capacity [J/kgK]

J = mechanical equivalent of heat

B = strength coefficient [kPa]

T = temperature [K]

n = work hardening exponent

Variables not defined are described previously. Using (3) and rearranging (4) then substituting and rearranging (2) which gives the equation dictating the required strain required for instability to occur.

$$\gamma_i = \frac{n_T \rho c J}{\beta (\partial\sigma/\partial T)} \frac{\sigma_T}{\sigma_d} \quad (5)$$

The strain ratio σ_r/σ_d is simply the quotient of the isothermal stress and the dynamic stress. Typically this value will not affect the final result by more than 15% and is, as a result, often ignored in first order approximations. The constant, n , has not been found to vary between isothermal quasi-static tests and dynamic tests.

A simplified approach to this derivation was executed by Staker in 1981 [70] and greatly streamlines the mathematics involved by proposing that,

$$\frac{dT}{d\gamma} = \frac{\tau}{C} \quad (6)$$

which is based on the assumption that due to the high strain rate, the entire amount energy produced by the deformation contributes to the heating. In this expression, C is the volume specific heat in $\text{kPa}/^\circ\text{C}$. Using this assumption and also equation (4) results in equation (7) which is essentially the same as (5) though somewhat simplified.

$$\gamma_i = \frac{-Cn}{\left(\frac{\partial\tau}{\partial T}\right)_{\gamma,\dot{\gamma}}} \quad (7)$$

The ρcJ value in (5) is essentially the same as C in (7) and since σ_r/σ_d would increase the result by a maximum of 15% and β decrease it by 10% the two essentially cancel out and leave the same equation as in (7). Similar studies have been done by Clifton et al [12], Culver [58] and Timothy and Hutchings [27]. In all cases, the only remaining terms are a specific heat term, the temperature dependence of the flow stress and the work hardening exponent. Perusal of Table 1 shows that though the specific heat term is constant, n and $\partial\tau/\partial T$ are of equal importance in the relation, and both of them have a standard deviation of approximately 24% within their columns. The large variation in

tensile strength with respect to the tempering time indicates the effects that the material parameters have on the materials performance. In summary, increasing the strain hardening exponent, n and/or reducing the temperature dependence of the flow stress value will increase the amount of strain that the sample can undergo before reaching its adiabatic instability point.

1.3.4. The Shear Band Width Models

A commonly modeled and often studied feature of adiabatic shear banding is the actual width of the resulting localized shear region. Many approaches and techniques have been attempted, each with its own benefits, drawbacks and required experimental data [20, 21, 33]. An *a priori* and post-mortem relation are covered in this section. In each case the width of the shear band is related to at least one material parameter or property. The difference between the two was that the first attempts to predict the width using every significant experimental variable in its derivation, where the second was a simple power relation utilizing only one material property and two dimensionless parameters.

Table 1: Physical properties of AISI 4340 steel [57]

Tempering temperature, °C	Tensile strength, MPa	<i>n</i>	$\frac{\partial \tau}{\partial T}$, kPa/°C	<i>C</i>, kPa/°C
204	1951	0.055	-1986	3600
260	1800	0.043	-1800	3600
316	1662	0.042	-1613	3600
482	1234	0.055	-1117	3600
649	883	0.092	-620	3600

Dodd and Bai's model for dimple shear, taking into account strain rate, heat resulting from plastic work and thermal conductivity [17] gives,

$$\rho \frac{\partial^2 \gamma}{\partial t^2} = \frac{\partial^2 \tau}{\partial y^2} \quad (8)$$

$$\beta \tau \frac{\partial \gamma}{\partial t} = \rho c \frac{\partial T}{\partial t} - \lambda \frac{\partial^2 T}{\partial y^2} \quad (9)$$

where y is the displacement along the axis perpendicular to the shear band length. The derivation of equation (9) was not based on any specific material type. After a few derivations and rearrangements the following equation can be obtained,

$$\delta = \left(\frac{\lambda T_*}{\tau_* \dot{\gamma}_*} \right)^{1/2} \quad (10)$$

where δ is the shear band half width, where the * subscripts indicate quantities characteristic within the band. As can be seen, the most significant material properties are the thermal conductivity, λ , the flow stress, τ_* , the temperature within the shear band, T_* , which in transformed shear bands is taken to be either the transformation or melting temperature. The only difficulty that remains is whether or not the quantity, $\dot{\gamma}_*$, has a certain characteristic strain rate for a given material. The problem can be easily circumvented at high strain rates since the viscosity of the material becomes important and the following is valid,

$$\dot{\gamma}_* \approx \tau_* / \eta. \quad (11)$$

In this expression, η is the coefficient of viscosity. Substitution of $\dot{\gamma}_*$ further simplifies (10) to the form

$$d = t_*^{-1} (khT_*)^{1/2} \quad (12)$$

This relation then implies that shear band width is a material characteristic and should be fairly insensitive to specific aspects of the loading condition such as strain rate. The only limitation of the model is that the material tested must fail within the ductile regime and not approach brittle fracture, where the model become less accurate. Based on published results [7, 18] and predicted values, the trends, if not the actual values, are very good and intuitively correct. This is very promising, considering the simple expression used to obtain these values.

A far simpler and less scientific approach was taken by Marchand and Duffy in 1988 [11] which nonetheless relates the width of the shear band to at least one known material property, the local strain after adiabatic thermoplasticity.

$$\gamma_{local} = aw^b \quad (13)$$

For Marchand and Duffy, experiments using HY-100 steel with $a=125.8$ and $b=-0.867$, the results fit their experimental data very well. Though not covered in the paper, it is conceivable that the variables a and b encompass other material variables such as density, specific heat, melting temperature, viscosity, strain rate sensitivity and the strain hardening coefficient.

As mentioned earlier, equation (13) appears to be dependent on test conditions and equation (12) is not. The $\dot{\gamma}_{\text{local}}$ can probably be equated to another constitutive equation including only material parameters similar to the ones used in equation (12), thereby making the two relations far more similar in appearance - quite possibly mathematically identical.

1.3.5. Clifton Shear Band Analysis

In 1978 Clifton presented a detailed analysis of shear localization for a rate-sensitive material loaded in simple shear, unlike the rate-insensitive equations (5) and (7). Derivation of the relation will not be covered here as the equation is only being used to demonstrate the effect that various material parameters, including strain rate sensitivity, have on the point at which shear instability occurs. If the quantity given by the following equation is positive the deformation process is then unstable.

$$-m\dot{\gamma}^{OP} \left[\frac{1}{\tau_r} \left(\frac{\partial \tau_r}{\partial \gamma^p} \right) + \frac{\beta}{\rho c} \left(\frac{\partial \tau}{\partial T} \right) \right] - \frac{\lambda \xi^2}{\rho c} \quad (14)$$

where m is the strain rate sensitivity parameter given as:

$$m = \frac{\partial \ln \dot{\gamma}^p}{\partial \ln \tau} \quad (15)$$

and $\dot{\gamma}^{OP}$ = the homogeneous plastic strain rate

$1/\xi$ = the wavelength of the inhomogeneity

λ = thermal conductivity

ρ = mass density

c = specific heat of the material

$\partial\tau/\partial T$ = variation of flow stress with temperature at a constant plastic γ and $\dot{\gamma}$

τ = applied shear stress

τ_f = represents the resistance of the material to plastic deformation

$\partial\tau_f/\partial\gamma_p$ = strain hardening rate

β = factor of plastic work translated into heat

The above equation assumes that instability initiates at some physical flaw in the form of a pit or groove. The ξ term represents the flaw size as the inverse of its wavelength. Examining the effect of each term in (14) will give a relative measure of its contribution towards material instability.

The Clifton analysis has labeled the thermal conductivity as the least important term in the relation. Nonetheless, a larger value will increase the stability of the material. The inverse of the wavelength also affects the point at which instability occurs, but would not cause a material which otherwise did not undergo shear localization to form a shear band. The first two terms in the square brackets are the most significant and vary the greatest depending on the material and its heat treatment condition. For this reason their relative magnitudes are very important. The strain hardening rate, $\partial\tau_f/\partial\gamma_p$, is taken as the crucial variable in whether or not localization will occur. A large strain hardening rate value will indicate a stable deformation process, while a very small value will make the positive second term the most dominant. In Clifton's work, where a cold rolled steel (CRS) and hot rolled steel (HRS) were compared the CRS had a much lower strain hardening rate than the HRS and, hence, was more likely to form shear bands. The last important parameter to be considered is the strain-rate sensitivity. Since both of the terms are multiplied by this value, a small

value of m , implying a high strain rate sensitivity, indicates increased stability. Thus, shear bands should occur more readily in steels than in aluminum. Temperature variations greatly influence the second term, $\partial\tau/\partial T$, specifically at low temperatures where the specific heat drops significantly, resulting in unstable material behavior. This effect has been noticed by many researchers to be valid.

1.3.6. Dynamic stress strain relationships

In this section, two separate models for dynamic stress-strain relations are covered. The first is a simple power law which utilizes the hardening exponent. The second is based on an exponential relation that, though does not include a hardening exponent, utilizes dimensionless hardening and softening parameters.

The first model to be discussed was used by Marchand and Duffy in 1988 [64]. Their dynamic stress-strain curves quite closely followed the power law,

$$\tau = \tau_y \left(\frac{\gamma}{\gamma_y} \right)^{\eta'} \quad (16)$$

where τ_y and γ_y represent the initial values of yield stress and strain respectively. In this expression, η' is the hardening exponent. Yield drops cannot be included in the modeling when using this relationship. The second equation is as follows;

$$\bar{\tau} = \bar{\tau}_o (1 + \alpha\bar{\gamma}) \exp(-\kappa\bar{\gamma}) \quad (17)$$

where $\bar{\tau}_0$ is the constant representing the shear yield stress, α is a dimensionless hardening parameter, and κ is a dimensionless softening parameter. $\bar{\tau}$ and $\bar{\gamma}$ represent effective or equivalent shear stress based on the Von Mises or "J₂" flow criterion. The behavior of equation (17) is shown in Figure 4, $\bar{\gamma}_i$ can be simply determined using the α and β parameters:

$$\bar{\gamma}_i = \frac{1}{\alpha \cdot \beta} \quad (18)$$

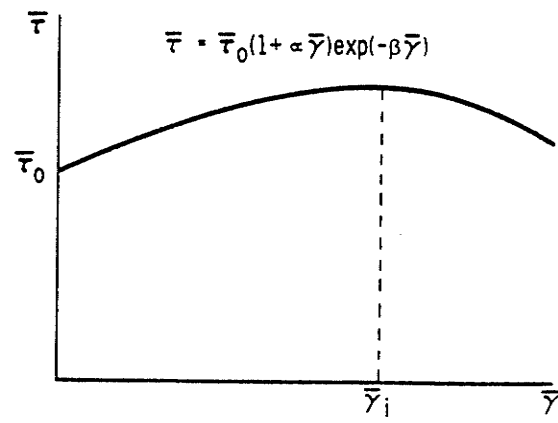


Figure 4: Illustration of equation 17 [9].

Both of the aforementioned models begin at the point of plastic deformation with work hardening, and neglect the elastic portion of deformation. The relations work relatively well and are reasonably reliable if all required materials constants are known, at least approximately.

1.4. MATERIAL BEHAVIOR AT HIGH STRAIN RATES

1.4.1. Introduction

It is possible to discuss the deformed shear band as a precursor to transformed shear banding, as has been done in some cases [10,22,23], this review will treat them as totally separate entities for the sake of simplicity.

1.4.2. Quasi-Static Versus Dynamic Deformation

In the classical quasi-static torsion model, plastic deformation is considered to be uniform throughout the cross-section, as shown in Figure 5. In high strain rate or dynamic torsional testing the classical quasi-static model applies for only a very brief period of time or for extremely low strain values. After this period the quasi-static regime ceases to be valid and adiabatic strain localization or shear banding begins. A frame by frame picture of a high speed torsion test taken by stop-motion photography is shown from start to finish in Figure 6. In Figure 6 the sample deforms according to elastic theory for a only a few frames, after which localization occurs as is shown by the nearly vertical deformation lines at the center of the specimen. It is important to note, however, that for very hard specimens brittle fracture begins to dominate over ASB formation and hence ASB theory is no longer applicable.

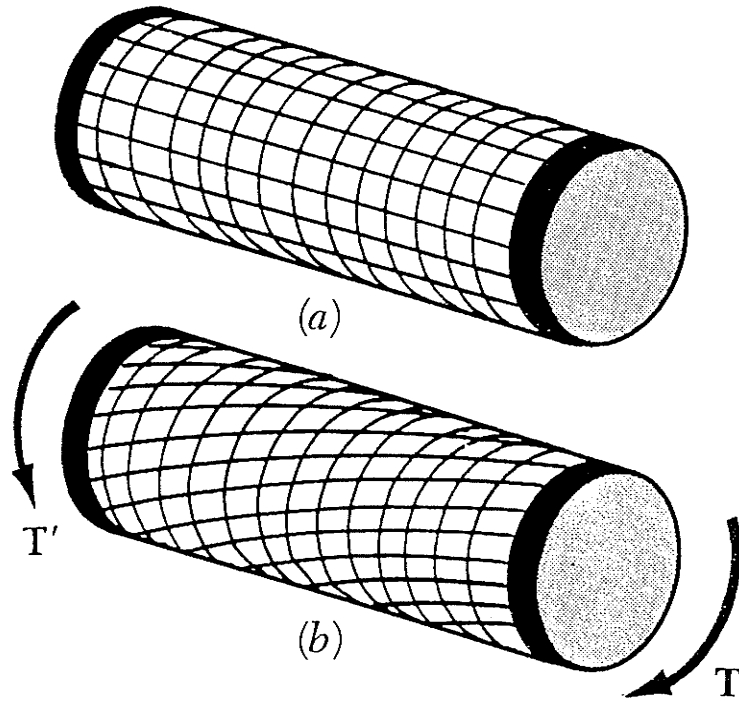


Figure 5: Uniform elastic-plastic deformation in torsion [82].

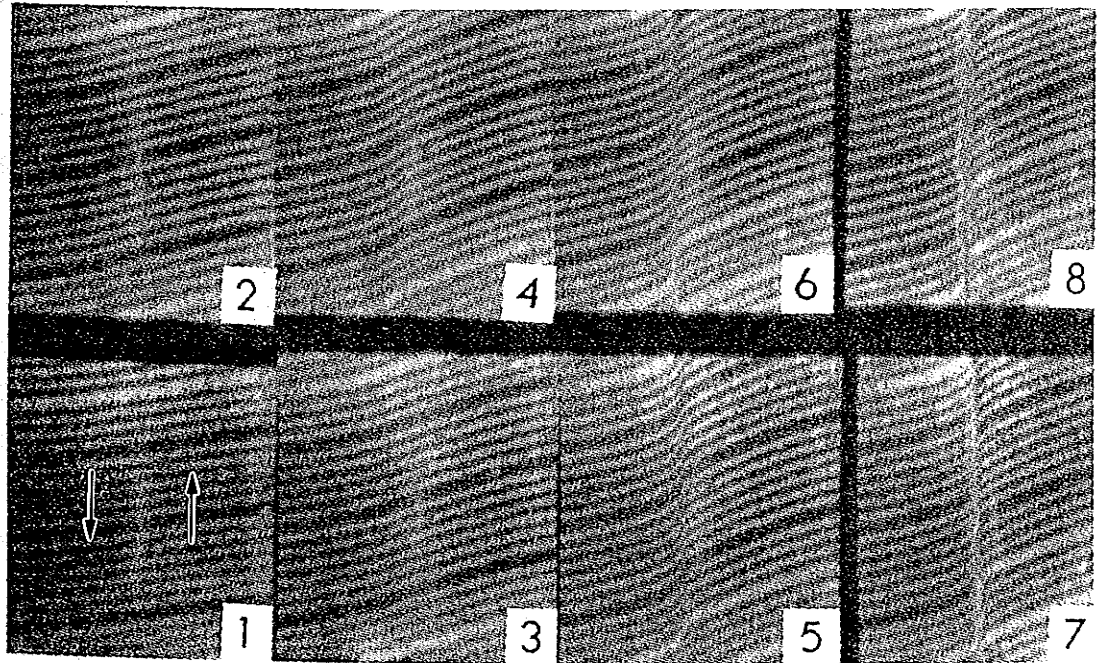


Figure 6: High-speed photograph of ASB formation [23].

1.4.3. The Deformed Shear Band

The deformed shear band can be described as a zone of intense shear deformation of the original microstructure across a very narrow band [24]. The reason for this occurrence is the presence of mechanical instability in the material at some point during the test. This instability functions as a nucleation point. The inhomogeneous shear zones undergo plastic work, which in turn heats the zone adiabatically and initiates thermal softening. This results in significantly reduced shear resistance in the shear banded region [25].

Typically, a single shear band will form due to the effect of a single nucleation point, though it is possible for multiple shear bands to form [7, 21] parallel to each other if two nucleation points of similar size and type are within close proximity of each other. Possible nucleation points include precipitates such as MnS [26], phase boundaries of two dissimilar phases such as pearlite and ferrite [23] or ferrite and martensite [27] and voids present within the material. More macroscopic points include; scratches, machine marks or thinner sections on the specimen. Each of the aforementioned flaws behaves as a stress concentration point and is subjected to more stress and deformation than the surrounding material. This results in more heat being generated in the region close to the flaw which in turn softens the material and creates an environment conducive to further deformation, strain localization and heat generation. It can be seen that upon the onset of adiabatic shear banding the process is self-regenerative until failure or subsequent removal of the dynamic load.

Shear strain within shear bands commonly ranges from 5 to 100 [3, 28-34], and in some cases as high as 570 [35]. The width of shear bands can range anywhere from 10

to 360 μm in width [3, 5, 23, 27, 36] depending on the material tested and the strain rate achieved

1.4.4. The Transformed Shear Band

The transformed shear band is initiated and forms through the same mechanisms as the deformed shear band. The only difference being that due to some specific material properties the specimen is capable of undergoing what is referred to as a phase transformation of a sort and experience a permanent change in microstructure [6, 10, 21, 25, 33-42], instead of remaining simply a deformed shear band. As mentioned before, the elevated temperature of the shear band has been inferred indirectly from metallurgical evidence [6, 10, 25-55] and directly from experimental observation [56, 57] to be much higher than in deformed bands, often up to several hundred degrees greater than the surrounding matrix. The shear band is then quickly cooled by the surrounding material upon completion of plastic deformation, implying that the material is quenched. Subsequent nital etching reveals the band to have a very high reflectivity and hence appear white in optical micrographs, Figure 7.

Cooling rates in the order of 10^7 K/s have been calculated [52]. If the temperature rise is great enough and the cooling rate fast enough, martensitic-type phase transformation is assumed to occur, resulting in a transformed shear band.

Identifying the shear band as definitely being martensite is a difficult task, considering the fact that there has not been any real unequivocal evidence proving that the phase is martensite [10, 21, 25, 58, 59] even from results published as recently as 1990.

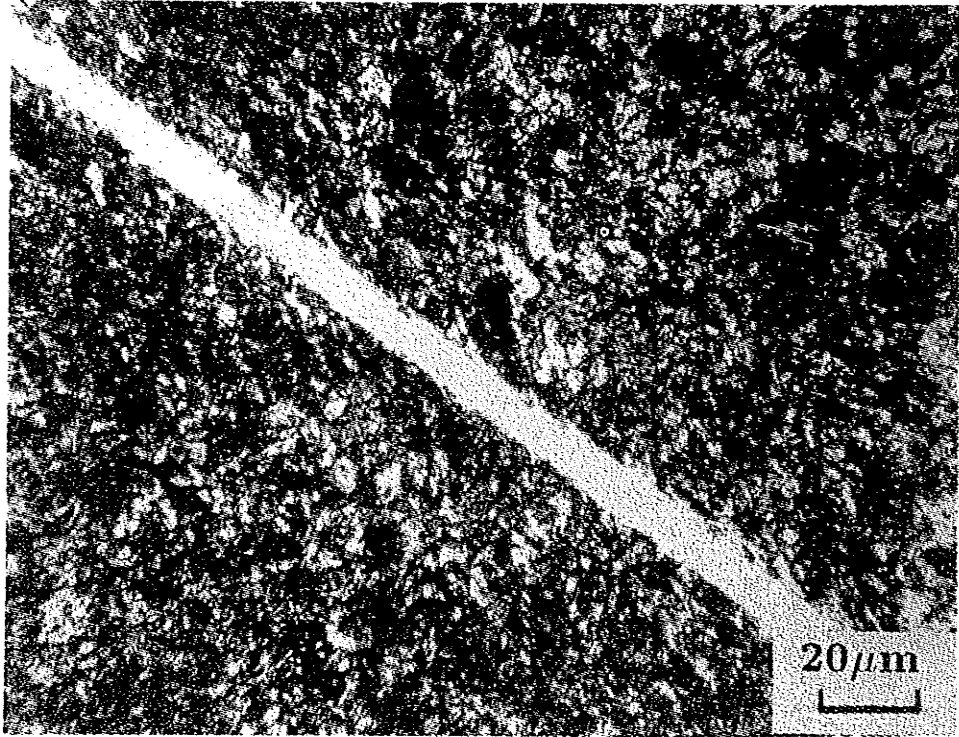


Figure 7: Example of a white etched ASB optical micrograph [23].

1.4.5. Formation of a Transformed Shear Band

The transformed shear band has generally been found to occur only in materials which display a phase transformation at elevated temperatures [21]. Typically, this also corresponds to materials with lower thermal diffusivities such as 4130 steels and 6Al-4V Ti alloys. Figure 8 shows the relation between thermal diffusivity and critical longitudinal strain for several materials tested. In the figure, fully blackened circles represent materials which form the transformed shear bands, half-filled circles represent deformed type shear bands and white circles indicate a material which does not usually undergo shear localization.

It is evident that as the thermal diffusivity increases so does the materials tendency to form shear bands of the transformed type, thus the most commonly affected materials are steels. [6, 10, 25, 34-40, 60-64] The strain rate sensitivity and strain-hardening rate are important related properties to the material resistance to adiabatic shear localization. A material with a high strain rate sensitivity and a low strain hardening rate will become unstable at high strain rates and ultimately fail through the formation of an adiabatic shear band.

The microstructure of a material also plays an important role in shear band formation, as mentioned by Backmann and Finnegan [6]. For a given strain rate, pearlitic/ferritic microstructures tend to favor deformed shear banding while tempered martensite has a tendency to form the transformed variety. Thus, most of the work reported on the TEM analysis of transformed shear bands is on materials that initially had a microstructure of tempered martensite [56, 65-68].

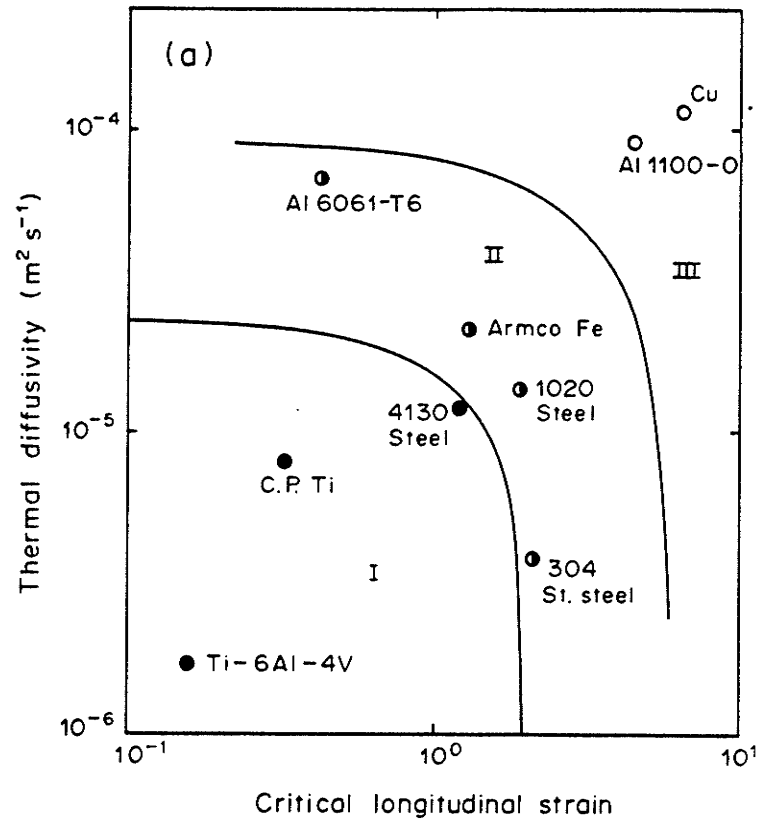


Figure 8: Thermal diffusivity vs. Critical longitudinal strain, showing material parameters influence on shear band type [21].

1.4.6. Temperature Requirements

Adiabatic heating plays a major role in the formation of the shear band, therefore temperature effects are rather critical, well pronounced and well documented. It has been determined, almost counter-intuitively, that lower test temperatures are more conducive to adiabatic shear band formation than elevated temperatures. This was first indirectly inferred in Zener and Holloman's landmark paper on shear banding in 1943 [28] and then reiterated and verified many times since [69, 70]. The reason for this effect is easier understood if analyzed from the actual case of the shear banding process instead of the shear band as an entirely separate and unrelated occurrence dependent only upon temperature. With increased test temperatures the plasticity of a sample increases along with the specific heat. These details, combined with the fact that less work is now required for deformation and all plastic deformation that can occur is less localized, results in a reduction of the temperature rise initiated by plastic flow. The absence of a significant temperature gradient between regions experiencing localized deformation and the bulk of the material hinders the mechanisms responsible for catastrophic flow, and ultimately leads to adiabatic shear band formation [67]. The end result is that at a given strain rate, a lower temperature test will be more likely to form a transformed shear band than a higher temperature test due to the steeper temperature gradient formed. Also, different degrees of strain localization and shear banding can be obtained by varying the test temperature for a given strain rate.

The question of whether or not there is in fact a temperature rise significant enough to induce a phase transformation posed a valid problem until Duffy and co-investigators were able to provide data which verified the presence of a very significant temperature rise across the shear band during shear localization [5]. Using an array of

infrared indium-antimony detectors with a spot size of 20 μm each, the surface temperature of the torsional samples could be measured over the area expected to undergo shear banding. The maximum recorded temperature was 455°C for a hot rolled steel specimen. Though this temperature may not seem to be large enough to cause a phase transformation, one must remember that the maximum temperature rise within a shear band will occur at the center of a 5 - 10 μm band, due to the high strain rate gradient present in the ASB. What this implies is that, even if the spot was centered exactly on the high temperature zone of the ASB, there would be a significant contribution to the temperature reading from the cooler surrounding material within the spot size. This could significantly reduce the maximum recorded temperature. If this was the case, it would be a strong argument in favor of the theory that a phase transformation does, in fact, occur. Conversely, it is very possible that 455°C is very near the maximum value and, though there is not a temperature rise great enough for phase transformation, it is high enough to allow deformation of a type that would give the appearance of a transformed region due to its drastically altered and deformed microstructure.

Whatever the temperature conditions may specifically be, it is well recognized that there is a temperature increase within the shear band and that it contributes significantly to the deformation mechanism and the resulting microstructure.

1.4.7. Microstructure and Morphology of the Transformed Shear Band

When accumulating research material regarding the structure of a transformed shear band it becomes obvious that there are many conflicting viewpoints and opinions all within a very small database from which to draw information. The existing

information is far from detailed and conclusive, but it does shed some light on the problem as well as giving an adequate starting point from which to conduct further research.

From research as early as 1944, shear bands which have appeared white when etched with Nital were assumed to be martensite [28] mainly due to their high reflectivity of light and high hardness. This belief was adopted by many researchers in the following years [7, 10, 22, 29, 36, 55, 71]. The white etch assumption might have stood up undisputed if it were not for further transmission electron microscopy (TEM) investigations of the so-called transformed shear bands and the interesting findings published by Turley in 1974 [31], where white etched shear bands were found to exist in specimens prepared through a process that would not be capable of providing the high temperatures required for phase transformation. Subsequent TEM analysis of the aforementioned rogue white etch bands revealed the structure to be BCC, definitely not of the transformed variety. The subgrain size was reported to be very small (0.05 - 0.1 μm) and there was also a reduction in visible carbides, both effects associated with transformed shear banding. This of course does not suggest that all white etch shear bands obtained through high strain rate testing in the past have been incorrectly classified as transformed shear bands. Just that it is conceivable now that the white etch may be an artifact of the etchant and extremely high localized deformation, not necessarily indicative of a phase transformation.

Supporting evidence of the above mentioned statement is provided by Manion and Stock [26] who showed that a sample containing a white etched shear band, assumed to be untempered martensite, could be subsequently tempered. If the aforementioned shear band was truly untempered martensite it should darken when

tempered and re-etched. The results were rather interesting, a first temper at 300°C for 30 minutes resulted in only one half of the shear band to darken whereas the other half remained white. An additional temper at 575°C for 30 minutes was required to darken the remaining half of the shear band. The markedly un-martensitic behavior of the second half of the shear band implies then that it perhaps was not typical martensite as is currently known to be, and that not all the white etch regions are untempered martensite.

With all the questions of whether or not the white etch shear bands are transformed or not, it was only a matter of time before analytical tools such as the TEM were used to study the bands in more detail. Considering the amount of uncertainty surrounding the topic of transformed adiabatic shear bands, there has been very little analytical work done on the topic. The limited research is due, in part, to the fact that specimen preparation is very difficult to carry out effectively. The white etch portion of the shear band resists the etchant more than the matrix and therefore yields a thicker specimen from which information is difficult to obtain.

One of the earliest attempts of shear band analysis used X-ray diffraction (XRD) to determine the lattice parameter for an ASB using $K\alpha$ and $K\beta$ radiation. The results seemed to show that the band was BCT martensite [56]. However this is by no means conclusive. The surrounding matrix was tempered martensite (carbides in a ferritic matrix) and could have easily contributed to the impression of a martensitic shear band. Also, there was no apparent presence of retained austenite within the shear band, another factor contributing doubts to the theory that a phase transformation had taken place. Finally, no concentration gradient was encountered when traversing the shear

band, implying the adiabatic heating was too brief in duration for any measurable amount of diffusion to occur.

TEM of the ASB seems to suggest a very fine grained, untempered martensite with no evidence of carbide precipitate particles or retained austenite, as mentioned earlier. The lack of austenite and the fine grains were attributed to the extremely rapid heating and quenching by the surrounding matrix. No additional proof of a martensitic transformation had been provided. Additional work from the same year provided evidence that the grains within the ASB were approximately $0.1 \mu\text{m}$ in diameter and possibly less [55]. Electron diffraction patterns indicated a BCC structure but it was still assumed to be martensite of some sort, in spite of the fact that for a 0.6% C steel the martensite is of BCT plate type [72]. It was concluded that there was insufficient time for recrystallization or grain growth in the austenite (which the authors show no there is no evidence of occurring) so the martensite just formed heavily deformed retained austenite. It is also difficult to accept this considering that austenite is FCC and none was mentioned to have been found.

A similarly timed publication by Wingrove [63] reconfirmed the presence of martensite in the shear banded region of the quenched and tempered steel through the analysis of TEM produced electron diffraction spots. TEM micrographs showed that the matrix was typical of a quenched and tempered high carbon steel with extensive carbide precipitation along micro twin boundaries. The white etch band, conversely, had a very high density of dislocations with some cell boundaries. Small precipitates could occasionally be imaged using dark-field techniques, but for the most part, they were very small and unidentifiable with any certainty. Tempering of the shear band did not cause the martensite to behave as would be expected, as it continued to etch white,

implying a lack of carbide precipitation which normally causes darkening, indicative of a tempered martensite. Nonetheless, the lattice spacings indicate it is in fact martensite, in spite of its unique morphology. The dislocation density could not be explained conclusively, but was thought to be generated during the deformation of austenite and inherited by the subsequently formed martensite. Another theory was that the dislocations were generated within the martensite during deformation, after the transformation process. The extreme plastic deformation during adiabatic shear banding can conceivably create a very high dislocation density in the austenite, but this assumes proof that some austenization takes place, which in this case did not and was never mentioned. The very small size of the precipitate particles was assumed to be due to the fact that they locked dislocations and thus survived the transformation to martensite. The shear bands resistance to tempering as normal martensite was attributed to either the carbides being so very small they were undetectable or that the carbon was trapped in solid solution - held by lattice defects such as vacancies and dislocations.

More contemporary work was far improved but still inconclusive. Dereps findings in 1987 [64] stated that as the ASB is approached there is a considerable decrease in the density of dislocations and that the martensitic lathes of the surrounding matrix seemed to becoming refined. Another interesting fact was that the mean diameter and density of the precipitates increased as the ASB was approached, going from a diameter 27 nm to 34 nm and a density of $6 \times 10^{10} \text{ mm}^{-3}$ to $2 \times 10^{11} \text{ mm}^{-3}$. Electron diffraction of all foils exhibited diffused rings that, when indexed, gave evidence of Fe_3C carbides in small proportion, austenite in very small quantities, ferrite and martensite sharing the same diffraction rings and iron oxide from the surface of the thin foils. Significant microstructural modifications occur near the ASB. In addition to the previously

mentioned details there is a precipitation of iron carbide particles. All of the changes that do occur are very similar to the modifications produced by heat treatment and are due to the temperature increase associated with some aspect of the strain localization. Areas close to the ASB have been subjected to temperature gradients which produce effects similar to annealing, including increased polygonization as the shear band is approached. The microstructure within the shear band was attributed to the fact that enough diffusion was allowed for carbides to be almost completely placed in solution. This would require a shear band temperature of at least 1000°C for 50 nm diameter precipitates to dissolve in 0.1 ms. The previously mentioned ferrite was thought to be delta ferrite, not alpha ferrite, which are impossible to distinguish in this instance due to the thermal contraction effects upon the shear band. This assumption would require that the shear band had become momentarily liquid, of course. Derop does not, in the end state that alpha transformation had indeed taken place, considering the large amount of seemingly contradictory evidence in regards to the occurrence of a phase transformation.

The most recent work in the field is also the most comprehensive and conclusive. Wittman, Meyers and Pak did a very extensive study of the shear band region in quenched and tempered 4340 steel with the TEM [62]. The findings were relatively close to what Wingrove had found, with a high dislocation density and some cell boundaries within the shear band. Also noticed, was the appearance of extra spots in the diffraction pattern upon tempering of the shear band, indicating a possibility of carbide precipitation in spite of the fact that the characteristic white etching band remained basically unchanged. The shear band itself did not possess a clear boundary between itself and the matrix, and the martensite structure was unlike common lath or plate-type martensite. The tip of the shear crack consisted of a highly deformed region,

narrower than the fully developed band. This was representative of all shear bands observed. In order to test the hypothesis of a phase transformation occurring the shear band was analyzed for the presence of austenite, but none was evident. As a verification of this the sample was immersed in liquid nitrogen for 1 hour such that any remaining austenite would be transformed into martensite, thereby increasing the hardness of the material. This process yielded no perceptible hardness variations.

Studying shear bands that were not yet fully developed showed a microstructure consisting of highly deformed martensite plates with alignment in the direction of the shear flow. The center of the shear band did not contain detectable grain boundaries and is attributed in part to the large foil thickness (approaching 5 grains thick, as shear band thinning is very difficult). Indexing electron diffraction patterns from this area indicated χ (Fe_3C_2) carbides in a martensite matrix. The carbides are commonly witnessed in the transition from epsilon to omega carbide during the onset of third stage tempering. What is noteworthy is that χ carbide usually requires a temperature between 200 and 400°C for 20 minutes before it becomes evident. Analysis of the internal twin boundaries revealed the presence of carbides common even without the influence of shear loading. The boundary between the matrix and the shear band revealed a presence of cementite carbides with diameters varying between 5 and 200 nm as shown through dark-field micrographs. An interesting aspect of the TEM micrographs was a tweed-like microstructure commonly associated with a significant amount of carbon in solution [73] usually found in heavily deformed martensite in which carbon is locked up at dislocations. This creates an image effect due to the interference of the electron beam and the carbon rich dislocations. The Hägg carbides (χ , Fe_3C_2) and cementite carbides have been attributed to one of many reasons. Firstly, the material was transformed to austenite and quenched rapidly to martensite with the remaining

adiabatic heat creating carbides. This was reported to be improbable due to the fact that there was absolutely no evidence of retained austenite in the shear band region, which is usually present even in materials splat quenched. The second possibility is that the Hägg carbides are the same as those that were initially in the matrix. The second theory is supported by the fact that a relatively large amount of heat is required to form the carbides mentioned in the first theory. Therefore, it is highly unlikely that a transformation could have taken place within the shear band followed by a quench to form martensite. This does not agree well with theoretical heat models and experiments that predict and show, based on the severe amount of shear, adequate temperature rise to induce austenitization. Though this is explained by assuming that heating was not of a significant enough duration to allow for the up-quench transformation to austenite to have occurred. The hardening was then proposed to be partly due to adiabatic heat induced carbon diffusion to dislocation sites within the shear band. Theoretical models seem to allow enough time for this to occur. A by-product of the above mentioned reaction would be a general reduction in carbide particle size, which would also explain the thermal softening observed by Rogers and Shastry [10] during microhardness traverses.

In summary of the paper by Wittman and co-investigators, the microstructure of the shear bands closely resembles the matrix with the stress having broken up the laths into very small pieces. It was concluded that the white etch is an artifact of etching and cannot provide enough information to allow the assumption of a phase transformation to be made. Instead, all that can be assumed is that carbides have been dissolved and are too small to cause localized pitting or that the microcrystalline structure within the band changes etching characteristics.

The assumption of a martensitic transformation seems to be the easiest explanation for the occurrence of a white etch. However, as mentioned earlier this requires a tremendous amount of heat in order to occur, though temperature rises have been recorded [11] and theoretically determined [64, 74]. It is believed that they are a result of the deformation process which encourages further localization of deformation by increasing the plasticity of the material in the shear band region. It is the highly localized deformation which causes the material to take on the characteristics it does, that is the very fine microcrystalline structure and increased dislocation density and subsequent hardness.

The shear band microstructure is best described by Whitman and co-investigators [65] as being the result of previously existing matrix carbides being broken up into much smaller, finely distributed particles throughout the band. The driving force for this process is the extremely high stress and the adiabatic heating inducing increased plasticity. Even though it seems that existing evidence rules out the possibility of a phase transformation having occurred, the above described shear band will still be referred to as being a "transformed" type for convenience sake throughout the rest of the document.

1.5. VARIOUS HIGH STRAIN RATE TECHNIQUES

There exist almost as many methods of obtaining high strain rate test conditions as there are research groups pursuing the topic. Selection of which method to utilize in the present study was based on cost effectiveness, practicality and the type of data and subsequent analysis desired. For the purpose of this study, a torsionally modified split-Hopkinson bar was deemed the most effective way of achieving high strain rate

experimental conditions and provide both data and adequate post-test specimens from which significant metallurgical information could be obtained. More detailed reasoning is supplied in Chapter 2. The remainder of this section will briefly touch upon the existing technology currently in use elsewhere.

1.5.1. Rod Impact

In 1947, Taylor and Whiffin [46 and 47 from (5)] accelerated cylindrical specimens into a rigid plate. The resulting plastic deformation shortened the rod. Through 1-D rigid plastic analysis the dynamic yield stress could be inferred. Subsequent studies determined the strain distribution in the test specimen. A variation of the rod impact is the symmetrical rod impact where two identical rods are collided. This modification helped alleviate problem related to the frictional effects inherent to the rod-plate collision, but introduced the problem of keeping the two rods perfectly aligned. Some drawbacks include a lack of a conventional stress-strain curve, a highly deformed sample which may not represent material behavior in the field and the lack of easily examined shear banded regions.

1.5.2. Expanding Ring

The expanding ring test is a very sophisticated and extremely effective means of subjecting samples to tensile loads with strain rates in excess of 10^4 1/s. In its most complex configuration it can provide the full high strain rate stress-strain relationship for the sample. Simpler configurations are limited to determining ultimate strain only. The test is based on the sudden detonation of an explosive charge at the center of the ring and for this reason only a few laboratories have the facilities, equipment and authorization to employ this technique.

1.5.3. Flyer Plate Impact

The flyer plate apparatus consists of a flat flyer plate slamming into a stationary target plate. Typical data produced during this test include high strain rate yield-stress, shock wave response, spall strength and equations of state information for materials undergoing uniaxial strain. Extreme care and precision must be exercised to ensure that there is no tilt between the target and impact plates. Typically, stress-strain curves and adiabatic shear banded regions are not generated.

1.5.4. Torsional Impact

This technique typically consists of a high speed lathe mounted device consisting of a rotating chuck and fixed chuck mounted components. Upon reaching the desired speed a spring loaded catch mechanism engages the two, previously unconnected, components. The ensuing impact is carried by the sample which acts as the weak link between the recently coupled device and is subsequently shorn. The test is susceptible to inaccuracies during data accumulation due to the impact of the catch mechanism and the sample is typically shorn right through, making subsequent shear band analysis very difficult.

CHAPTER 2

DESIGN AND IMPLEMENTATION OF A TORSIONAL SPLIT-HOPKINSON BAR

2.1. INTRODUCTION

This section covers all the design details involved with the torsionally modified split-Hopkinson bar. Included are its construction and the methodology involved with data acquisition, post-processing and interpretation. A description of the equipment used for signal measurement, data acquisition and amplification is provided. The operating procedure for varying temperature and strain tests are also given. Since the experimental specimens are equally important as the apparatus, specimen preparation, including all details of machining, specimen geometry, heat-treatment and final polishing are included.

2.2. HOPKINSON BAR THEORY

The split-Hopkinson bar is by far the most commonly utilized experimental configuration for high-strain rate material testing. Since its conception in 1948 by Kolsky [75], many arrangements of the bar have been used, including compression, shear and torsion, shown in figure 9.

The basic set-up is shown in Figure 10. As is often the case in high strain rate testing, it is not always possible to directly monitor the test specimen for data regarding to the stress and strain state the specimen is undergoing. For this reason, the sample must be monitored indirectly. In the case of Hopkinson bars the stress-strain

information from the sample is derived from the wave magnitude signals entering and leaving the specimen, the difference between total input and total output represents the amount of load signal required to deform the sample. For the torsional split-Hopkinson bar the load impulse is supplied by the sudden release of a stored torsional wave (which shall be discussed later). The input, or incident, wave and the transmitted and reflected waves are all recorded by strain gauges and captured by a computer. Subsequent analysis of the captured data, done as detailed later in this chapter, provides all pertinent stress-strain information.

The theory behind the bar involves obtaining data on the dynamic stresses, strains and displacements at the end of a bar based on information obtained at some location near the center of the bar. Provided that impact-load traveling through the bar remains elastic in nature, the disturbance at the end of the bar will remain essentially undistorted except in very high frequency components. The speed of the wave traveling through the bar follows the relation;

$$c = \sqrt{\left(\frac{E}{\rho}\right)}$$

Where E is the modulus of elasticity and ρ is the density. This equation is valid for axially applied pulses, either positive or negative in nature. For shear pulses the modulus of elasticity would be replaced by the modulus of rigidity, or shear modulus, G . Deformation of the sample occurs because its size, or more specifically, cross-section, is much smaller than the Hopkinson bar, resulting in the elastic wave traveling through the Hopkinson bar to plastically deform the sample.

For this thesis it was decided that a torsional version of the split-Hopkinson bar would be constructed due to the combined factors of the drawbacks associated with axial-type bars and the benefits inherent to torsional type bars. The shortcomings intrinsic to the axial-type compression type Hopkinson bars shall be discussed in order to establish further justification for the construction of a torsional bar.

Due to the Poisson's ratio effect, compressive loading is always accompanied by a radial expansion of the test specimen. With this radial expansion is the opposing force of radial inertia, which increases with shorter pulses and greater pulse amplitudes. This results in a radial stress component superposed on the axial component. Thus, in a test which is supposed to be uniaxial, the stress state is not fully uniaxial. To further compound the problem, elimination of the radial stress component is not a trivial calculation due to the fact that it relies on dynamic material parameters not yet determined.

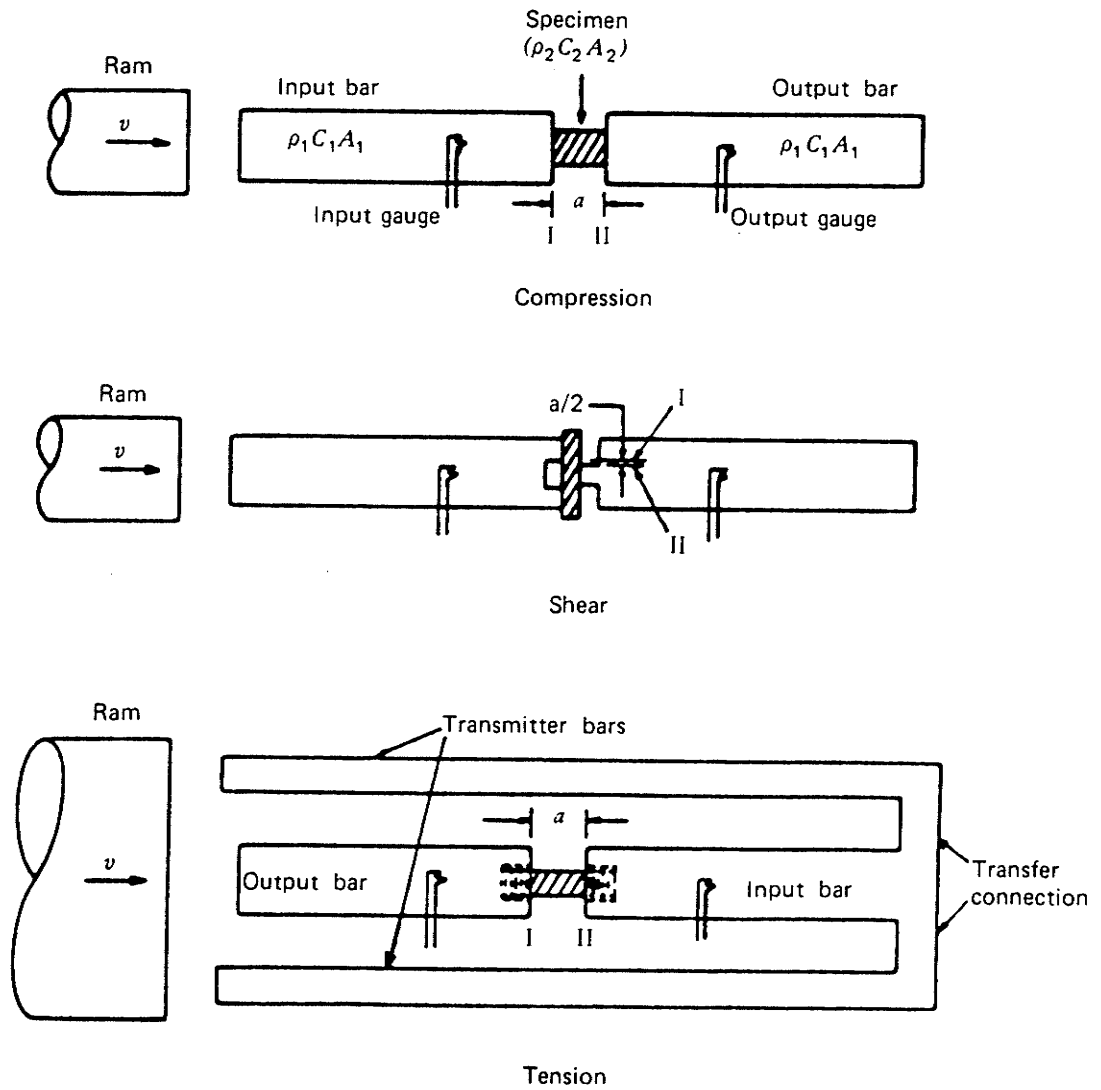


Figure 9: Various configurations of the Hopkinson bar [76].

DCDT: direct current differential transformer

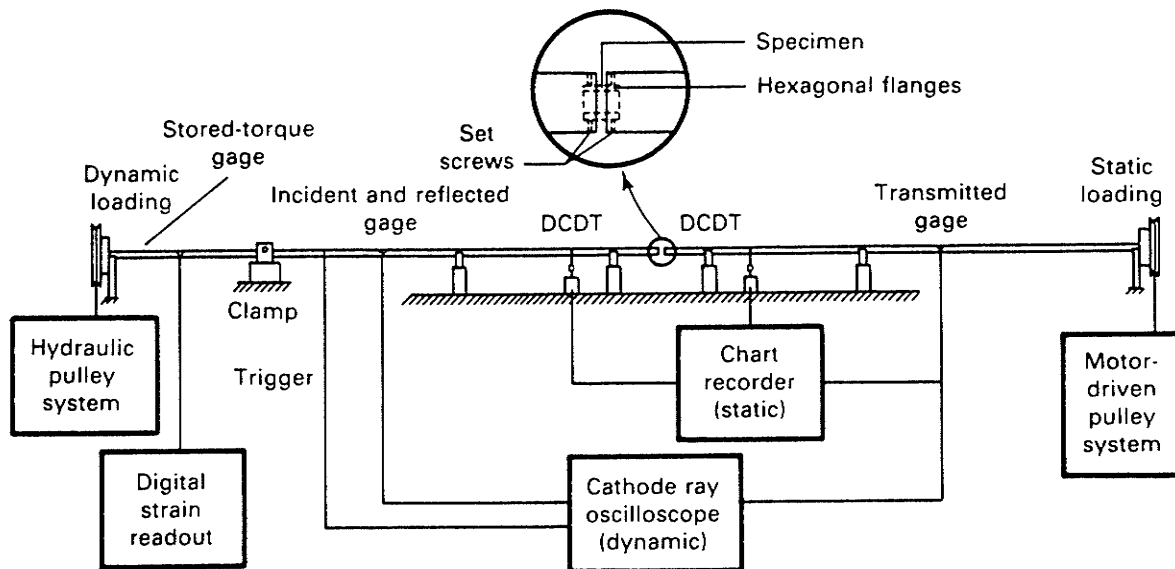


Figure 10: Typical set-up of a torsional Hopkinson bar [76].

Another problem associated with the radial expansion of the sample is the friction induced radial traction acting at the interfaces between the sample and the loading bars. Friction can be minimized through proper lubrication, but it can never be eliminated. All of these factors, plus the fact that the sample is severely deformed after testing contribute to the difficulties associated with compression testing, resulting in torsional impact being a very attractive alternative.

In torsion testing, due to a complete lack of Poisson's ratio effects, radial deformation of any significant variety does not occur. This implies that inertial and frictional effects prevalent in axial testing are non-existent in the torsional test. These factors were the driving force behind the development of the torsional Kolsky bar. A beneficial quality which was later determined is that strain rate sensitivity values obtained using the torsional bar compare well with axial tests.

Another important difference between the axial and torsional setup is the nature of the pulses traveling along the length of the cylindrical bar. An axial pulse will undergo geometric dispersion due to the fact that different frequency components of the pulse travel at different velocities [76]. This effect is especially pronounced in higher frequency components. Conversely, there is no geometric dispersion when a torsional pulse travels elastically down a bar. This implies that as the pulse is carried toward the specimen it will not change its shape.

A benefit of the no dispersion quality is that a pulse initiated with a very low rise time will sustain this sharp wave front without any alteration to the pulse due to various components of the wave moving ahead or falling behind the main body of the pulse, independent of the length of the Kolsky bar. This quality in torsional pulses lends itself well to pulse measurement. Contrary to axial/longitudinal pulses, the strain gages used

to measure the pulses can be placed as near, or far, from the specimen as is convenient and still accurately represent the magnitude and duration of the pulse, as it affects the specimen. In axial Kolsky bars, a gage placed too far from the specimen will provide irrepresentative signals due to excessive dispersion, while a gage too close to the specimen will be susceptible to three dimensional end effects.

A disadvantage to the non dispersive nature of the wave is that if the torsional pulse is noisy when initiated, implying it is superposed by some high-frequency distortion components, this quality will be maintained by the pulse for the duration of its existence. A direct effect of the noisy pulse would be an equally variable strain rate, the physics of which will be described later.

Torsional split-Hopkinson bars can also be modified for use as a quasi-static torsional apparatus [11], allowing quasi-static incremental strain rate and dynamic strain rate tests. This arrangement allows strain rate effect tests to be done without incurring the errors associated with using more than one test apparatus throughout the range of strain rates. The modification consists of fixing the free end of the transmitter bar to the base of the apparatus and applying the quasi-static load to the incident bar where the jack mechanism is currently attached. Load application is facilitated through the use of a powerful electric motor coupled to the bar with a speed reducer. This modification was not implemented in the present study due to time and cost constraints.

In his axial bar, Kolsky showed that in the measurement of the pulses on either end of the specimen, the portion of the incident loading wave that is transmitted through the specimen yields a measure of the axial stress, while the magnitude of the reflected wave is in proportion to its strain rate. With a torsional Kolsky bar the axial stress and strain values are replaced by shear stresses and angular displacements.

Combining output from the strain gages on opposite sides of the specimen and integrating the strain rate/time pulse to yield strain versus time, as will be shown later, provides a complete record of the stress-strain curve.

The actual stress wave in the torsional Hopkinson bar is produced by the sudden release of a stored torque. The loading pulse itself is produced by clamping the bar at some predetermined distance from its end equipped with some mechanized means of twisting the clamped length. Upon loading to the desired level of strain, the retentive force of the clamp must be suddenly released. An ideally functioning clamp will hold the bar with no slippage and release the torque expediently and cleanly enough to consistently provide a sharp fronted, flat stress pulse, as often as is required. Due to this necessity, the clamp is the most critical component of any successful torsional Hopkinson set-up. The design of which will be discussed subsequently.

Upon release of the clamp, the stored torque is released in the form of two torsional pulses equal and opposite in magnitude, exactly one half the value of the stored torque each. One of the pulses propagates from the clamp towards the specimen while the aforementioned equal and opposite unloading pulse propagates from the clamp towards the loading mechanism. The resulting phenomenon is commonly overlooked in related literature in spite of the already contained evidence. The length of the stress pulse is, if one disregards rise time and clamp release noise, exactly double the length of the loaded portion of the Hopkinson bar. The reasoning behind this is illustrated in Figure 11.

If at the point of clamp release the solid and dotted square waves represent the loading and unloading pulse respectively, the loading pulse moves to the left while the equal and opposite unloading pulse moves to the right. Upon moving to the right, the

unloading pulse will immediately ricochet off of the loading end, invert to be the same sign as the loading pulse and instantly, and seamlessly, attach itself to the loading pulse, effectively doubling the length of the loading pulse and the ensuing torsional pulse. Evidence of this phenomenon is provided in the following section.

2.3. DESIGN OF A SPLIT-HOPKINSON BAR

In 1992 a preliminary design of a split-Hopkinson bar at the University of Manitoba had been developed based on the schematic shown in Figure 10. No actual bar was available. The major focus of the current study involved design and implementation of the apparatus covered in this section.

2.3.1. The Loading System

The method of loading is facilitated through the rather simple yet highly effective hydraulic jacking mechanism shown in Figure 12.

Upon adequately securing the bar to prevent slip (the clamping mechanism, Figure 18, will be discussed later), torque application to the load section is done by cranking the jack, Figure 12. Between the loading arm and the point of contact with the jack is a load cell calibrated to provide the applied load in kilograms. Next, the applied torque is calculated by taking into consideration the acceleration of gravity and the length of the torque arm.

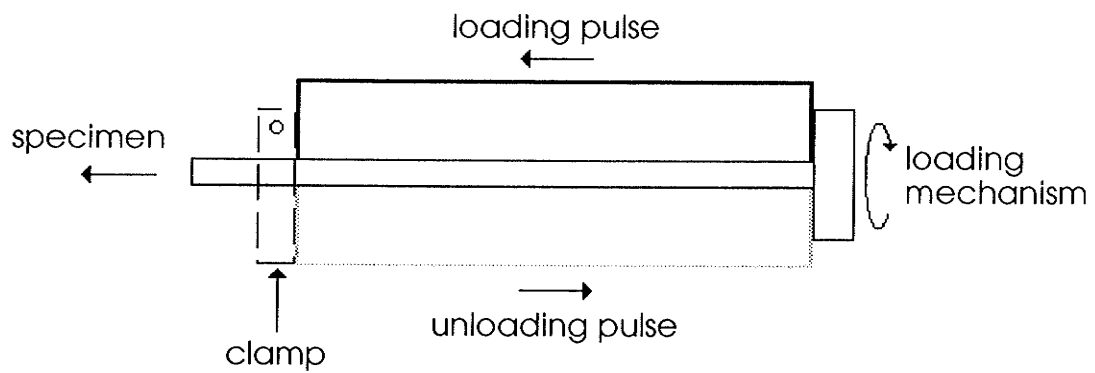


Figure 11: Behavior of the loading and unloading pulses upon clamp release.

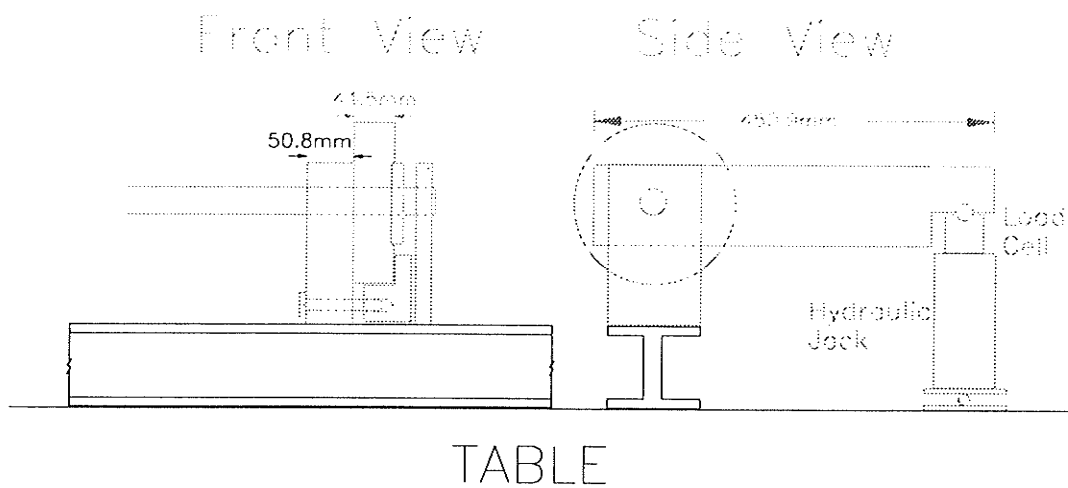


Figure 12: The jacking mechanism.

To eliminate errors, there are two other redundant systems which are used to obtain the actual applied load. To counter the detrimental effects of jack pressure decrease, the loading wheel can be locked in place with a caliper clamp. However, for the most part, this is not necessary as the jack decrease is slow enough to allow for fracture of the load release pin with no more than a few percent loss in stored torque. The jack itself is a simple 3 ton hydraulic jack fixed to a swivel base to compensate for motion of the lever arm when twisting the bar.

2.3.2. Specimen Mount

Another extremely important aspect of the entire experimental setup is the way in which the specimen is held between the two ends of the Hopkinson bar. The literature shows that for materials of relatively low flow stress the specimen flanges can be fastened with epoxy to the ends of the bars. This method is not effective for stronger materials such as the SPS-Plus steel used in these experiments.

It was decided that machined hexagonal sockets and hexagonal flanged specimens, 15.88 mm across and 6.35 mm deep would be used for the specimen gripping set-up, as shown in Figures 13 and 14. Unlike some cases in the literature [5], no set screws or rigidity increasing compounds like glycol phthalate were used. This does not preclude the possibility of set screws being retrofitted to the existing apparatus for future experimental runs though.

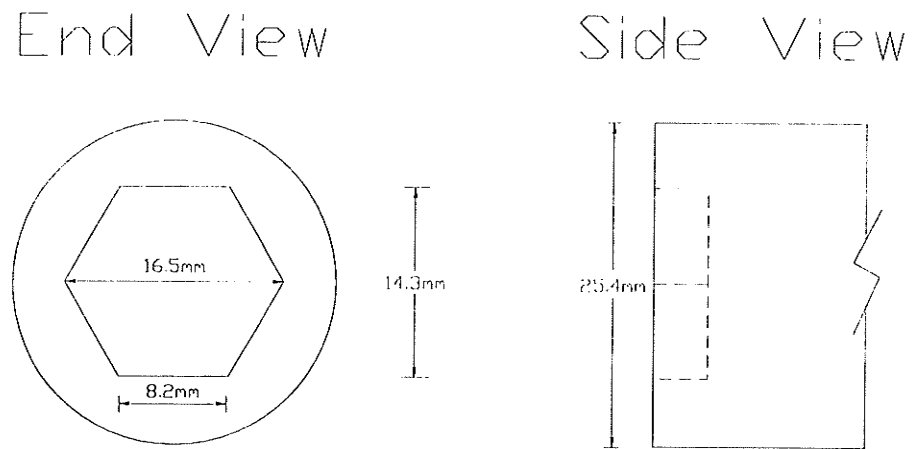


Figure 13: Specimen slot at end of the bars.

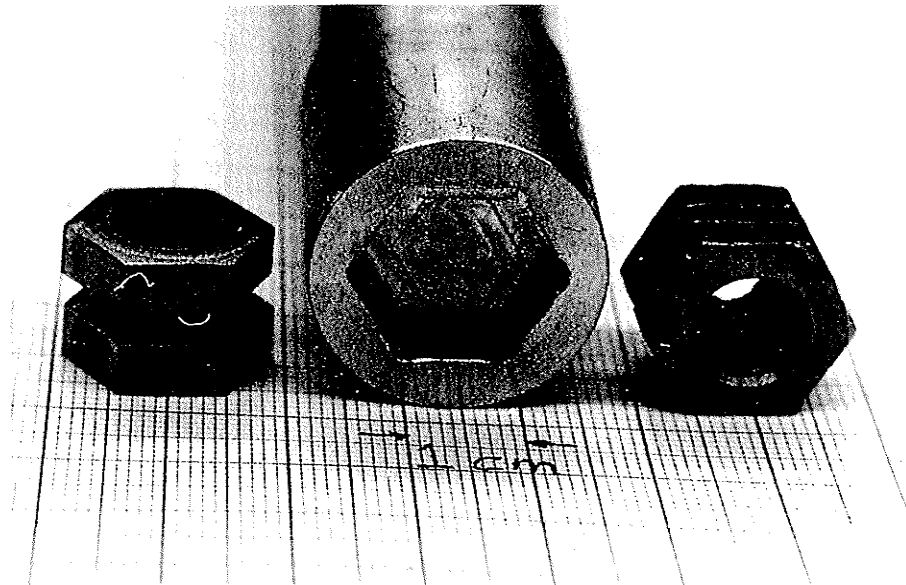


Figure 14: Photo of specimen and specimen slot.

2.3.3. Strain Gage Placement

Due to the complex nature and interactions present within the Hopkinson bar, more specifically the incident bar, careful attention must be paid to the placement of the strain gages. As touched upon earlier, the necessary data for processing the stress-strain history of the sample are obtained through the combined analysis of the incident, transmitted and reflected waves. Placement of a gage too close to the specimen will result in the leading edge of the reflected wave interfering with the trailing edge of the transmitted wave, thereby ruining the data over the interval of overlap. Conversely, using an arbitrary distance away from the sample is also not feasible either because there are physical restraints imposed by the length of the bar and the space constraints available for this rather long set-up. Optimally, there are two things that should be considered in order to ensure proper bar design. First is the length of the section to be twisted which acts as the source of the load impulse. Second, is the actual wave characteristic diagram that functions to give the time displacement record for all three of the required waves for the duration of the test.

2.3.3.1. Wave Characteristic Diagram

An example of a wave characteristic or Lagrangian diagram is given in Figure 10. Interpretation of the wave characteristic diagram is not nearly as difficult as it seems. The starting point of the wave is directly under the clamp gage section at time equal to 0 μ s. Based on the velocity of the wave, given above to be approximately 3100 m/s, and the dimensions of the bar (i.e. the length) one can derive the time displacement history for every wave and its accompanying reflection.

In the case of the Hopkinson bar used in the present experiments, since the clamped section is 49 cm long the load impulse will therefore be 98 cm long or 316 μs in duration. In order to avoid overlap of the incident and reflected waves, the incident strain gage must be at the very least 49 cm from the end of the bar. This location coincides with the intersection of two lines at approximately the 570 μs line, in Figure 15, more specifically immediately to the left of it. This location should be theoretically clear of any overlapping zones, but due to real effects such as rise time, decay and clamp release noise it is necessary to move a few centimeters further away from the specimen. A complete drawing of the final working design is provided in Figure 25.

The second important gage to be placed is on the transmitter bar. Since both bars are of equal length, the transmitter bar is relatively immune to reflective overlapping effects, due to the fact that they occur so late in the test. So late, in fact, that all the necessary data has been captured and the test completed before the transmitted wave could reach the end of the bar and return to overlap with itself. Gage placement, in this case, is simply the same distance from the sample as in the transmitter bar.

A beneficial side effect of placing the gage the same distance from the sample on both ends is that, when captured at the same time, it facilitates easier data reduction and increases accuracy [77]. Placed in this manner, one does not have to be concerned with the timing of the signal capturing devices, as they can be triggered simultaneously. Slight discrepancies between the placement of the two gages can be overlooked, as an error of 1 mm in alignment corresponds to an error of only a fifth of a microsecond [73].

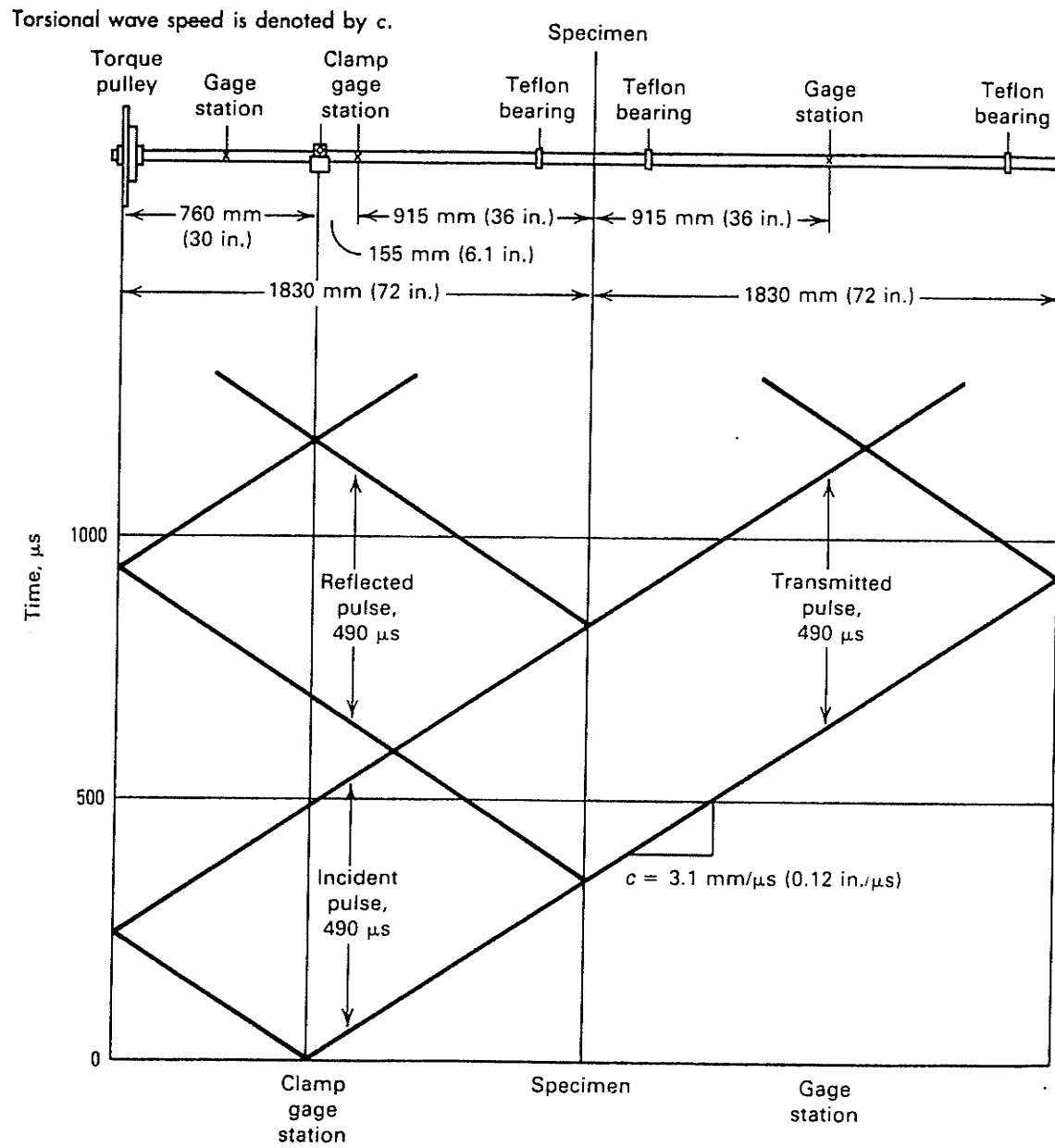


Figure 15: Langrangian or time-displacement diagram superposed on a typical split-Hopkinson set-up [73].

The third strain gage placed on the Hopkinson bar is probably the least significant. It provides the magnitude of the stored torque in the bar before unloading and can be located anywhere within the clamped section, but preferably near the center to avoid inhomogeneous end-effects. This gage also functions as a means to measure the load in the bar and aid in calibrating the instrumentation.

2.3.4. Criteria For the Design of the Load Length

2.3.4.1. Velocity of the Impulse

In order to be able to make accurate calculations as to the location of the wave at a given time, it is necessary to first know, at least approximately, the velocity of a shear wave through an aluminum bar.

In the Handbook of Chemistry and Physics [78], the velocity of a plane transverse (shear) wave in rolled aluminum was given to be 3040 m/s. As will be shown later, the use of this approximation proved to be very accurate, as was verified upon completion and testing of the split-Hopkinson bar.

For the sake of accuracy in later calculations, and to show the techniques used to determine it, the true value for the shear velocity is calculated through data obtained during regular testing of the Hopkinson bar.

To measure transverse wave velocity, the bar is set up to record data as in normal testing. All the required information is provided by the transmitted wave record. Attention must be paid to the configuration of the recorder such that capture duration is set long enough to have record of the waves first pass under the strain gage as well as

the leading edge of the same wave inverted after striking the end of the transmitted bar. The inversion effect is illustrated in Figure 16.

The circled sections of the wave represent the matching arbitrary points on the wave from which all calculations are based. Figure 17 shows the actual record used for this calculation.

The time between the two reference points represents the time required for the wave to travel 99 cm, reflect off the end of the bar and travel back along the same 99 cm. Since the time between the two points is 631.08 μs , the speed of the wave in the bar is;

$$\frac{2 \times 99[\text{cm}]}{631.08[\mu\text{s}]} = 3139 \left[\frac{\text{m}}{\text{s}} \right].$$

As can be seen, this is a very close to the published value of 3040 m/s. In fact, only off by $\approx 3\%$. Since the factors of safety are far larger than this, it can be concluded that having worked with the value of 3040 m/s was adequate.

Having obtained an exact value of the velocity for future reference, the next step is to determine the absolute minimum length of the wave that would still cause a fracture in the specimen.

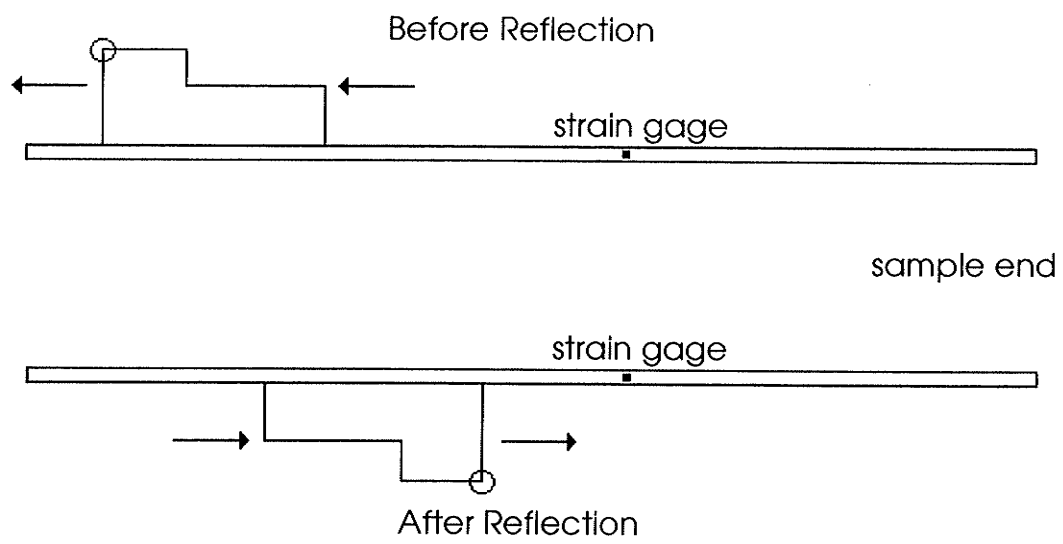


Figure 16: Tracking the wave inversion effect in order to calculate shear wave velocity.

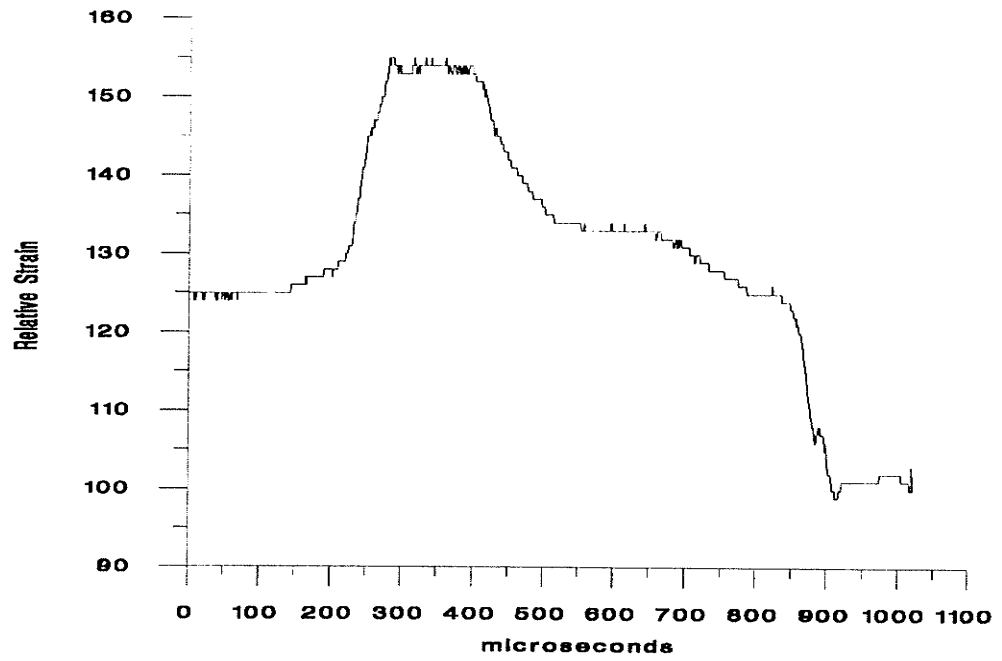


Figure 17: Transmitted pulse trace.

2.3.4.2. Specimen Fracture Criteria

Throughout the calculations presented in this section a number of assumptions have been made for the sake of simplicity. In turn, factors of safety have been introduced to counter the possibly detrimental aspects of the assumptions.

The standard sample size of a 12.7 mm internal diameter and a 13.39 mm outer diameter with a resulting wall thickness of 0.34 mm is used in the following calculation. The amount of energy required to illicit the onset of yielding in a quasi-static test can be calculated as follows.

The torque T_y at the onset of yielding is given by:

$$T_y = \frac{\tau_y J}{c_2} \quad (19)$$

where τ_y is the shear stress required for yielding, J is the polar moment of inertia and c_2 is the outer radius. In the case of a hollow cylinder, J would be;

$$J = \frac{\pi}{2} (c_c^4 - c_1^4) \quad (20)$$

In the case of the average specimen in the present study,

$$\begin{aligned} J &= \frac{\pi}{2} \left[\left(\frac{13.39}{2} \right)^4 - \left(\frac{12.7}{2} \right)^4 \right] \\ &= 602 [mm^4]. \end{aligned}$$

Based on the fact that the steel used is a medium carbon type similar to 4340 and previous data, the maximum yield strength that can be obtained through heat treatment can be taken to be $\tau_y = 1000$ MPa. Following equation (19), this would result in a torque at yielding of,

$$\begin{aligned} T_y &= \frac{1000 \times 601.93}{13.39/2} \left[\frac{Nmm^4}{mm^3} \right] \\ &= 89907 [Nmm]. \end{aligned}$$

The angle of twist at this same point would be,

$$\phi_y = \frac{\tau_y L}{c_2 G}, \quad (21)$$

where L is the gage length and G is the modulus of rigidity or shear modulus. The resulting twist is thus,

$$\begin{aligned} \phi_y &= \frac{1000 \times 4.953}{13.39/2 \times 79000} \left[\frac{Nmm^3}{Nmm^3} \right] \\ &= 9.36 \times 10^{-3} [radians] \\ &= 0.536^\circ. \end{aligned}$$

The approximate limiting value, under quasi-static test conditions, for plastic deformation would be as follows,

$$\begin{aligned}
 T_p &= \frac{4}{3} T_y \\
 &= \frac{4}{3} (89907.16) [Nmm] \\
 &= 119900 [Nmm].
 \end{aligned} \tag{22}$$

The next part of the calculation lays out the limitations of the Hopkinson bar based upon the material and geometry of the twisted length.

The absolute maximum strain, γ_{\max} , that could be carried by the bar is as follows;

$$\begin{aligned}
 \text{since } \tau &= G\gamma \\
 \gamma_{\max} &= \frac{\tau_y}{G} = \frac{140}{26} \left[\frac{MPa}{GPa} \right] \\
 &= 5.38 \times 10^{-3}.
 \end{aligned} \tag{23}$$

This maximum strain would correspond to some degree of twist or torque within the bar, depending upon its length L .

$$\phi_{\max} = \gamma_{\max} \frac{L}{c}, \tag{24}$$

where c is the radius of the bar. This results in a twist of,

$$\begin{aligned}
 \phi_{\max} &= 5.38 \times 10^{-3} \frac{469.9}{12.7} \left[\frac{mm}{mm} \right] \\
 &= 0.199 [radians] \\
 &= 11.42^\circ.
 \end{aligned}$$

These numbers are based on the current length of the clamped section, L . Recalling the approximate value of torque required to generate fracture to be 120,000 Nmm from equation (22), the maximum torque produced in the loaded section can be determined and then compared to the specimen value to see if at least that amount of torque can be produced.

The equation used to calculate the torque in a bar of given length is as follows;

$$T_{\max} = \frac{\phi_{\max} JG}{L}. \quad (25)$$

Substituting values in for the above equation yields,

$$\begin{aligned} T_{\max} &= \frac{0.199 \times \frac{\pi}{2} 12.7^4 \times 26}{469.9} \left[\frac{\text{mm}^4 \text{GPa}}{\text{mm}} \right] \\ &= 450,500 [\text{Nmm}]. \end{aligned}$$

Based on the above calculated value, the current design of the bar should be capable of effectively breaking materials having up to three or four times the strength for which it was designed. This factor of safety is large enough to accommodate any increases in material strength introduced due to dynamic loading.

2.3.5. The Clamp/Release Mechanism

The clamping mechanism is shown in Figures 18 and 19. The clamp itself is utilized by loosening the loading bolt and then fully tightening the load release pin as much as possible by hand. At this point the loading bolt is tightened enough to remove

any slack in its motion plus another quarter of a turn. The desired load can now be applied with minimal slip of the bar, after which the loading bolt is tightened until fracture of the load release pin. In order to verify the validity of the clamps effectiveness, a few calculations are made to illustrate the effectiveness of the design.

Assuming that the bar will be loaded to its maximum load resulting from a twist angle of 12° or 0.209 radians, the accompanying torque in the bar would then be,

$$T = \frac{0.209 \times \frac{\pi}{2} 12.7^4 \times 26}{469.9} \left[\frac{\text{mm}^4 \text{GPa}}{\text{mm}} \right]$$

$$= 472500 [\text{Nmm}].$$

This torque can be expressed as a force acting on the surface of the 12.7 mm radius bar.

$$F_{bar} = \frac{472551.29}{12.7} \left[\frac{\text{Nmm}}{\text{mm}} \right]$$

$$= 37200 [\text{N}].$$

In order for the bar not to slip, there must be at least that much braking force from the clamp, after slip losses. The coefficient of static friction between mild steel and aluminum is $\mu = 0.61$ [79]

$$F_{brake} = \frac{F_{bar}}{\mu} = \frac{37208.76}{0.61} [\text{N}]$$

$$= 61000 [\text{N}]. \quad (26)$$

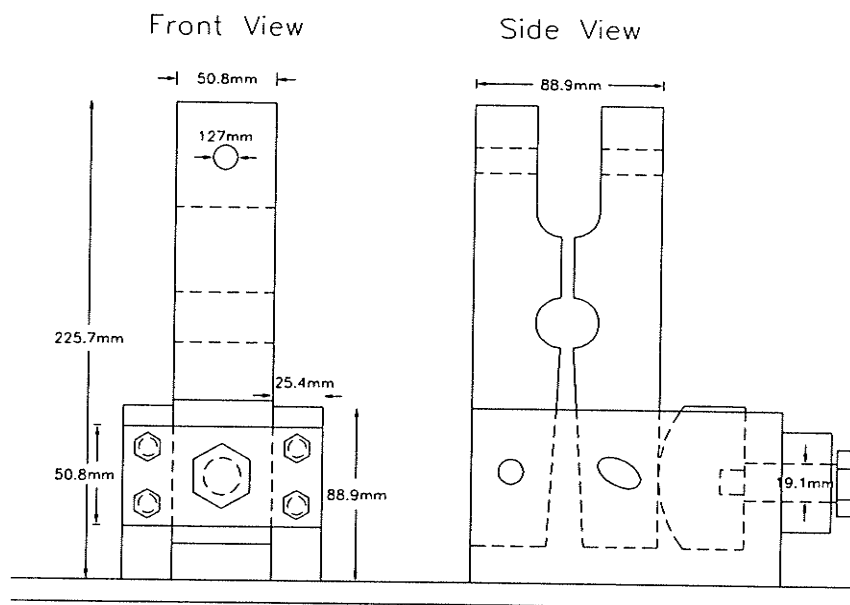


Figure 18: Sketch of the clamping mechanism.

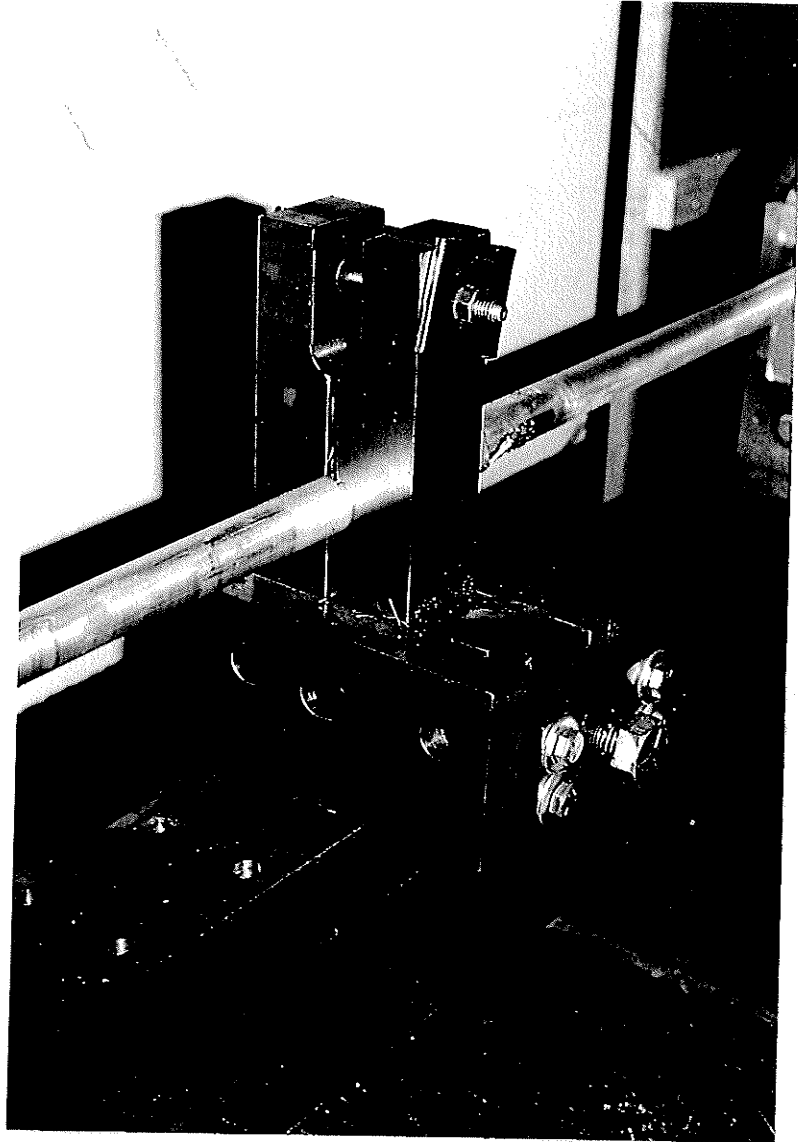


Figure 19: Photograph of the clamping system.

As illustrated in Figure 20, the load on the pin will be F_1 , where,

$$\begin{aligned} F_1 &= \frac{3.55}{7} 60997.97 [N] \\ &= 30900 [N]. \end{aligned} \quad (27)$$

In order for the mechanism to perform as described above, this load must be sustained by the fracture pin without premature failure. The load carried by the pin, σ_{pin} , will be,

$$\begin{aligned} \sigma_{pin} &= \frac{F_1}{A_{pin}} \\ &= \frac{30934.69 \left[\frac{N}{mm^2} \right]}{\pi 4.763^2} \\ &= 434 [MPa]. \end{aligned} \quad (28)$$

Since the pin is made of high strength steel, it can easily accommodate the aforementioned load without premature failure, even with a stress concentration notch machined through its midsection to ensure fast, brittle fracture. Further tightening of the clamp, as prescribed earlier in the section, will cause fracture and ultimate release of the stored torque to occur.

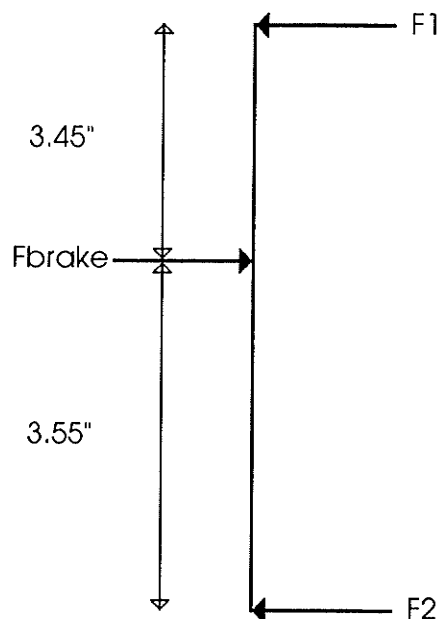


Figure 20: Force diagram of the clamping mechanism.

2.3.6. Final Mechanical Design

The bar is constructed of two 1.829 m lengths of 25.4 mm diameter 6061-T6 aluminum. The bars are suspended on a series of Teflon bushing lined mounts which are, in turn, attached to a 4 m long I-beam which functions as the base of the whole apparatus.

With every fundamental component of the test apparatus having been covered in detail, the Hopkinson bar can now be shown as the sum of its components. Figure 25 shows a schematic of the torsional split-Hopkinson bar, and Figure 22 is an enlarged view of the loading side of the Hopkinson set-up. The electronic componentry and schematics are described in the following section of the text.

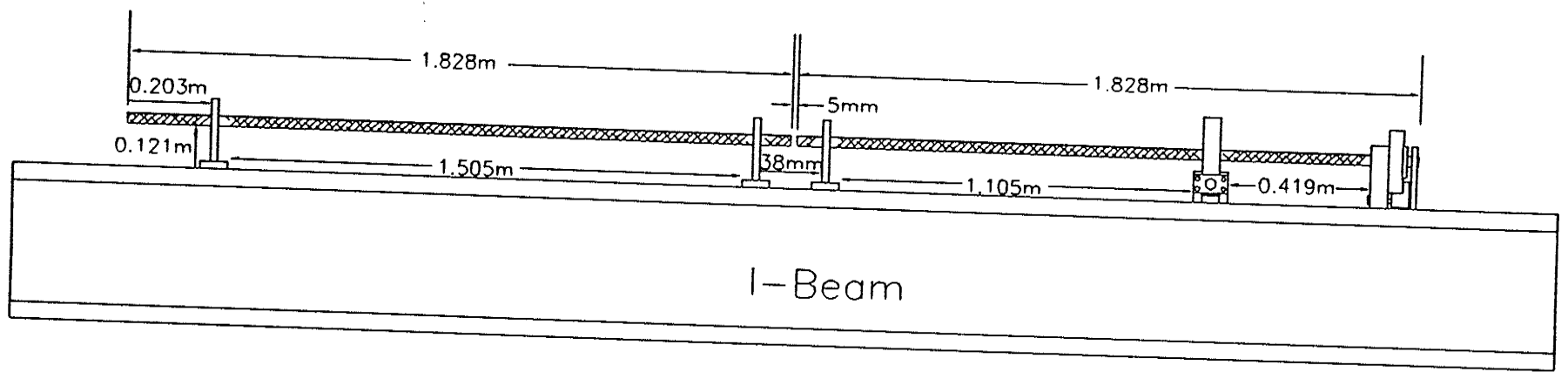


Figure 21: Sketch of the Hopkinson bar set-up.

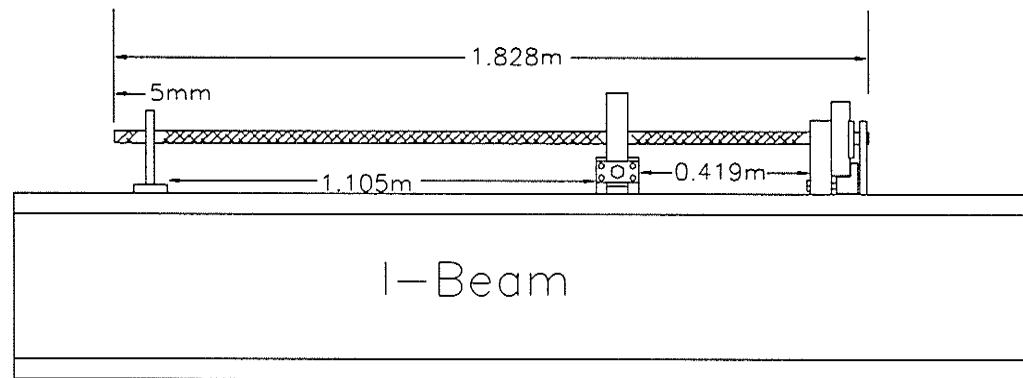


Figure 22: Enlarged view of the Hopkinson bar - loading side.

2.4. ELECTRONIC INSTRUMENTATION / DATA ACQUISITION

The electronic instrumentation of the system is based on three transient wave form recorders which capture the incident, transmitted and reflected waves. The system is completed with the addition of 3 amplifiers, 3 strain gages, 3 non-storage oscilloscopes, 1 digital storage oscilloscope, a personal computer and a signal switching box. The set-up will be described as an integral unit rather than by individual component.

All data acquisition starts with the strain gages on the surface of the bar. Typical 90° offset tension gages, and the problems associated with using them in torsion, have been by-passed in favor of torsional type strain gages designed specifically for this manner of application. The strain gages were supplied by Measurements Group, Inc., type CEA-06-250US-350. The apparatus was fitted with 3 separate strain gages. Two on the incident bar and one on the transmitted bar. Each strain gage signal is amplified by one of the three amplifiers which increase the signal to a full scale output of 10 volts. The incident bar strain gage uses a Honeywell Accudata 118 amplifier while the transmitter bar gage is coupled to an Accudata 218 amplifier. Only the two gages placed equidistant from the specimen shall be examined closely, as they are the only gauges responsible for the test data acquisition. From the amplifiers, the signal is then ready to be captured by the Biomations 805 transient wave form recorder. The amplifier for the incident signal also provides the reflected signal, and thus must have a signal splitter at its output to accommodate each of the two connected Biomations. The typical set-up consists of two digital storage oscilloscopes working in parallel. The first captures the incident and reflected waves and the second captures the transmitted wave. The drawback of this set-up is the fact that the scales of both the scopes are set

such that two waves could fit in the memory at once. This results reducing the possible resolution to one half of the maximum. With three independent capturing devices maximum resolution can be utilized.

The transient recorders used have the ability to be internally or externally triggered, with the trigger delay time adjustable to precisely the duration required. In addition, the length of the stored signal can also be easily set based on the pulse duration. With the principle of operation established, it was decided to have the first unit, the incident wave recorder, be the master recorder to which the reflected and transmitted recorders would be linked. That is, the incident recorder triggering the storage of the reflected and transmitted waves.

The order of events in signal capture are as follows. The incident pulse travels over the first strain gage, the incident recorder would detect this initial signal and commit its entire duration to memory. At this point the incident recorder would send a trigger pulse to the remaining two recorders. Since both remaining signals have an equidistant path from the specimen to their respective gage, the delay after incident trigger is set to the same value for both of them. The delay and duration on the reflected and transmitted recorders have been adjusted such that the signals stored on them start at approximately the same point in memory as in the incident recorder. With all three signals captured, the data is ready for the next step in processing / storage.

To check the status of the stored signal, each of the recorders is coupled to a BK Precision 2120 non-storage oscilloscope. In order to transfer the data to DOS format disk, the use of a Gould 4035 digital storage oscilloscope was required. The Gould scope has the ability to download stored traces from each of the transient recorders and upload them, individually, to the personal computer through an IEEE interface card.

Selection of which signal to transfer is facilitated by a 3-channel switching box located underneath the electronics rack.

The Gould is computer controlled by a program which was modified for this operation. The program stores the signals as three individual ASCII files, which can then be manipulated by either an automated stress-strain / strain rate history generating program, written specifically for this task, or manually manipulated in a spreadsheet program, to the same basic result.

2.4.1. Equipment Calibration

The calibration presented in this section does not apply to the individual components of the system, piece by piece, such as various amplifiers or wave form recorders. It is assumed that everything has been previously calibrated to roughly the same gain and full scale output, as per their respective manuals. This section is provided to explain how the entire collective system was calibrated and each of the components adjusted to perform on par with the others, and ensure that each device used to provide the data is on scale with each back-up system.

Since amplifier performance may change slightly if moved to another strain gage, the amp were calibrated with the strain gage they would be coupled to during the experiments. To calibrate the load cell with the strain gage on the loaded section of the bar and the accompanying twist indicator, the following operation was performed. The clamp was tightened and the bar loaded in small increments up until maximum safe load was achieved. At each increment the load displayed on the strain gage, the load cell and the twist gage were recorded and then converted to torque by whatever mathematical manipulation was required. The relationship between the three techniques

was linear and directly proportional, indicating that the load cell and twist gage were accurate systems of redundancy to the strain gage. Calibration curves of the aforementioned operation is provided in Figure 23.

To ensure that all the signals produced would react identically to a given input, the transmitter and incident bar were connected via a solid core sample that would undergo minimal deformation regardless of the applied load. With the clamp loosened and the loading arm in the rest position, another loading arm was attached to the end of the transmitter bar. From this temporarily affixed torque arm, calibration weights were hung and the deflection of the incident/reflected and transmitted signals measured. The respective amplifiers were then fine tuned until their signals, reactions and deflection matched exactly the strain gage output from the loaded section of the incident bar and the equivalent torque inferred from the load cell. Upon completion of this technique the signal detection and amplification is perfectly calibrated and ready for testing.

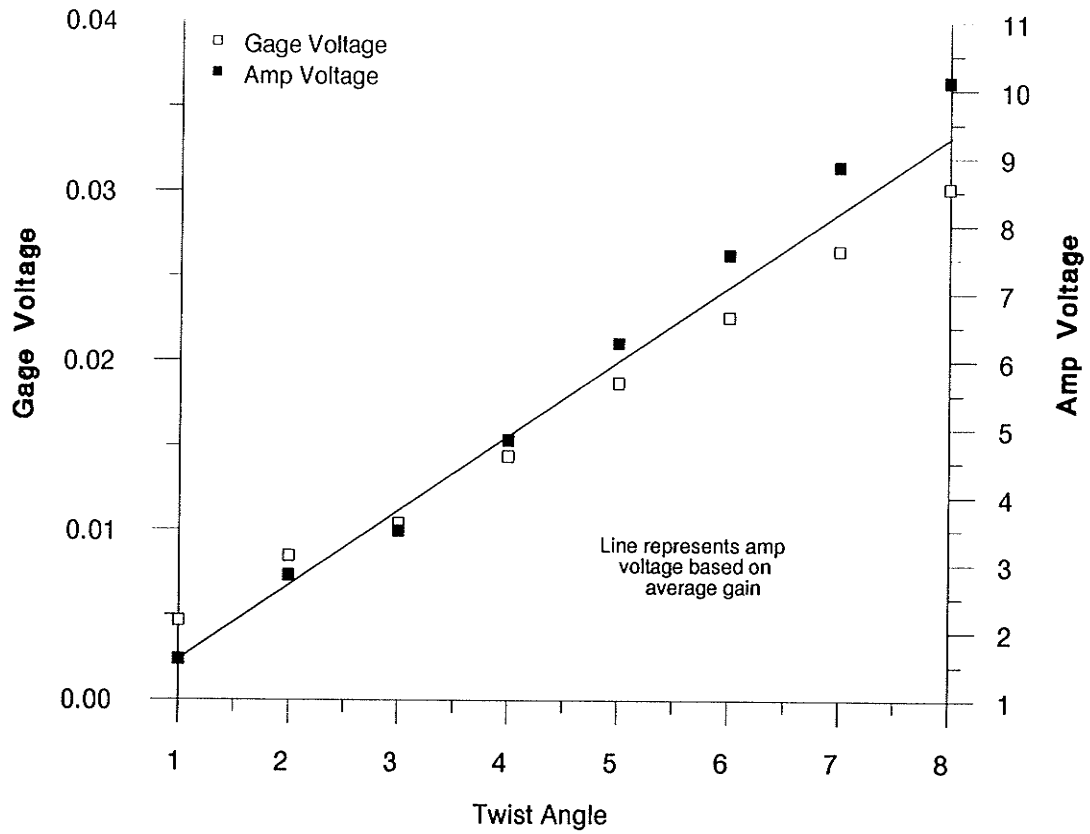


Figure 23: Calibration Curves for the Hopkinson bar.

2.5. CALCULATING STRESS, STRAIN AND STRAIN RATE

With a working split-Hopkinson apparatus and data acquisition system in place, all that remains to be done is the necessary post-processing and data manipulation to provide the stress, strain and strain rates for each test. Originally the analysis was developed by Kolsky for tension, but appears in this section transposed to shear [73]. The building blocks for these calculations are in the incident, transmitted and reflected pulses, shown in Figure 25. It is the use of these building blocks which will now be discussed in detail.

One fact that must be kept in mind when analyzing stress-strain data from the Hopkinson bar is that the inherent limitations of the design preclude its effectiveness for determining material behavior in the elastic region due to stress-wave reflection, nonuniformity of stress and large strain-rate variations during the initial portions of the test [85]. The nonuniformity is well illustrated in the strain rate vs. time graph in Figure 25.

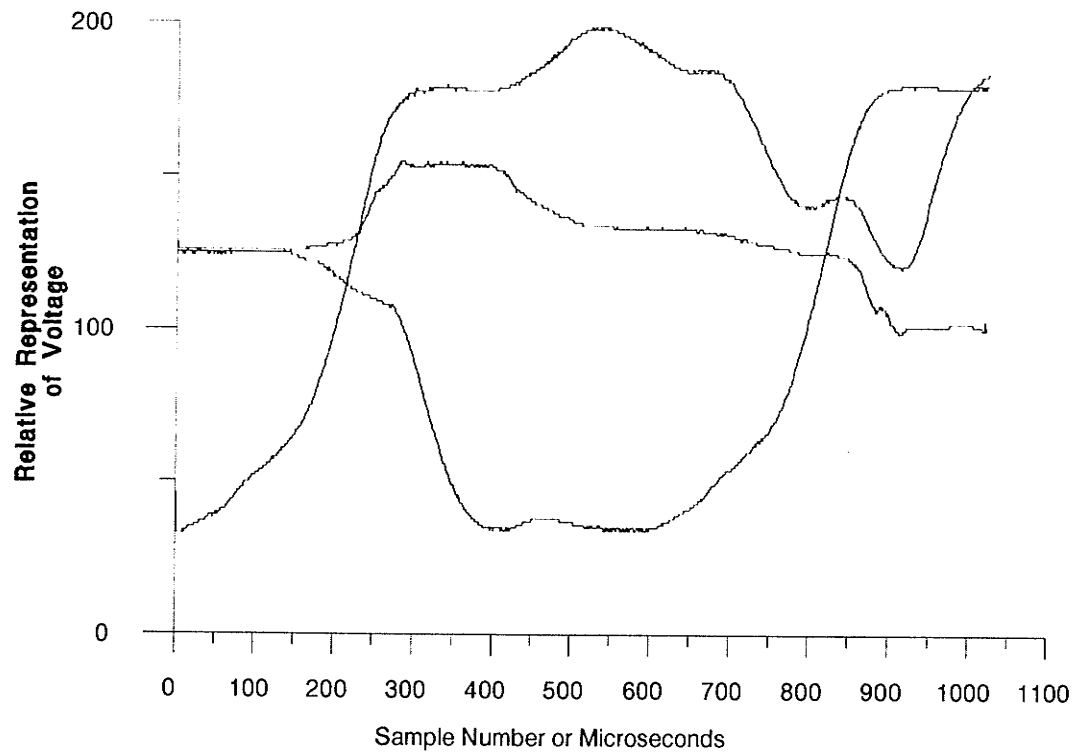


Figure 24: The Incident, Reflected and Transmitted Pulses.

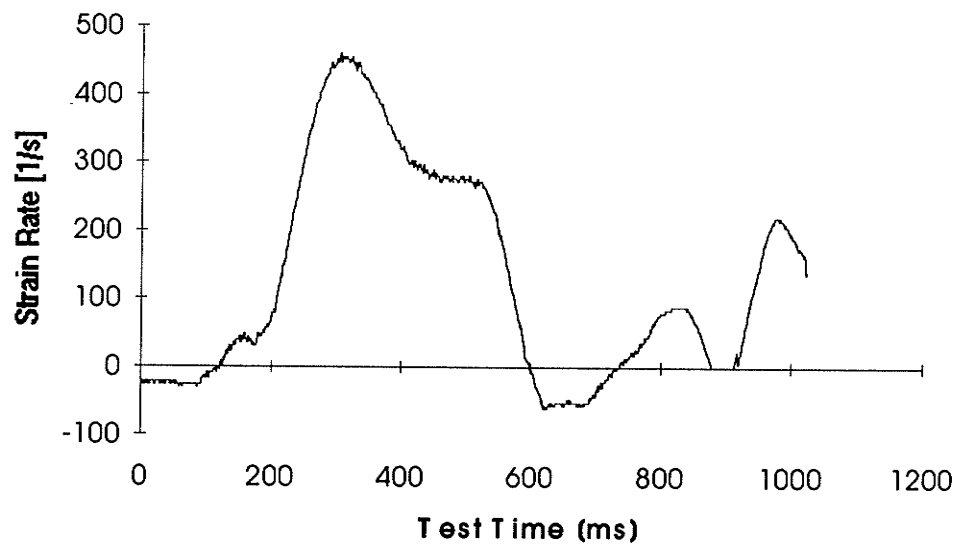


Figure 25: Strain Rate vs. Test Time.

Keeping with Kolsky's analysis, the reflected torsional pulse provides a measure of the shear strain rate through the specimen, $\dot{\gamma}_s(t)$. Single integration of this quantity yields the shear strain in the specimen, $\gamma_s(t)$. The shear strain in the specimen can be expressed as the difference in rotation of the two ends, divided by its length,

$$\gamma_s = \frac{D_s \phi_1 - D_s \phi_2}{2L_s}. \quad (29)$$

ϕ_1 and ϕ_2 are the twist angles of the incident and transmitted bars, respectively. D_s is the mean diameter of the thin walled specimen and L_s is the gage length. The value of ϕ_2 can be obtained from the surface shear strain of the transmitter bar by:

$$\gamma_T = \frac{D}{2} \frac{\partial \phi_2}{\partial x} = \frac{D}{2c} \frac{\partial \phi_2}{\partial t} \quad (30)$$

in which D is the diameter of the Kolsky bar and

$$c = \sqrt{G/\rho},$$

the torsional velocity in the Kolsky bar. From this relation ϕ_2 can be expressed as,

$$\phi_2 = \frac{2c}{D} \int_0^t \gamma_T(t) dt, \quad (31)$$

and similarly, ϕ_1 can be expressed as the difference in strains due to the incident and reflected pulses:

$$\phi_1 = \frac{2c}{D} \int_0^t [\gamma_I(t) - \gamma_R(t)] dt. \quad (32)$$

The negative sign is required due to the fact that the reflected pulse travels in the -x direction. Differentiating equation (29) and substituting in (31) and (32) for ϕ_1 and ϕ_2 , respectively, will yield:

$$\dot{\gamma}_s(t) = \frac{c}{L_s} \frac{D_s}{D} [\gamma_T(t) - \{\gamma_I(t) - \gamma_R(t)\}], \quad (33)$$

with all the strains being a function of time. In the case of a homogeneous state of strain in the specimen, the transmitted pulse can be expressed as the difference between the incident and reflected pulses, that is,

$$\gamma_T \approx \gamma_I - (-\gamma_R).$$

This assumption would cause equation (33) to be simplified to the form

$$\dot{\gamma}_s(t) = \frac{2cD}{L_s D} \gamma_R(t). \quad (34)$$

The assumption posed to derive equation (34) from (33) relies heavily on the occurrence of a very uniform strain-rate. Analysis of the curves has shown this to be incorrect. Though the strain rate is generally constant, there are aspects of change within the test that cannot be overlooked and should thus be taken into consideration when calculating all aspects of the experimental results. All quantities in equation 33 are known and constant except for the magnitude of the strain values γ_I , γ_R and γ_T which are provided by the digital acquisition equipment.

Integration of equation (33) yields the value of strain, $\gamma_s(t)$, in the sample. For example:

$$\gamma_s(t) = \int_0^T \frac{2cD_s}{L_s D} [\gamma_T(t) - \gamma_I(t) + \gamma_R(t)] dt, \quad (35)$$

where T is the duration over which the required strain value is to be obtained. As mentioned previously, full time for data acquisition would be 1024 μ s with each interval, Δt , being 1 μ s in duration. Simplifying equation (35) to a more workable form yields,

$$\gamma_s(t) = \frac{2cD_s}{LD} \sum_{i=0}^{1024} [\gamma_T(t) - \gamma_I(t) + \gamma_R(t)] \Delta t, \quad (36)$$

which is the total strain acting on the specimen.

For the specimen shear stress, Kolsky has shown that the transmitted pulse, $\gamma_T(t)$, provides a direct measure of the average shear stress in the specimen. In a thin-walled tube loaded in tension, the stress is expressed by:

$$\tau_s = \frac{2T_s}{(\pi D_s^2) t_s}, \quad (37)$$

where t_s is the wall thickness and T_s is the average torque. The specimen average torque is expressed in terms of the average torque at each of its ends.

$$T_s = \frac{1}{2}(T_1 + T_2), \quad (38)$$

in which T_1 is the torque at the specimen - incident bar interface and T_2 the torque at the specimen - transmitter bar interface. T_1 is given in terms of the strain at the surface of the bar, that is, the incident and reflected pulses:

$$T_1 = \frac{G(\gamma_I + \gamma_R)\pi D^3}{16}. \quad (39)$$

In a homogeneous state of strain in which $\gamma_I + \gamma_R \approx \gamma_T$;

$$\tau_s(t) = \frac{GD^3}{8} \frac{\gamma_T(t)}{D_s^2 t_s}, \quad (40)$$

but as mentioned earlier, the state of strain is seldom uniform enough to assume it as such, and thus equation (40) is modified instead to be;

$$\tau_s(t) = \frac{GD^3}{8D_s^2 t_s} [\gamma_T(t) - \gamma_I(t) + \gamma_R(t)]. \quad (41)$$

Thus, strain rate has been calculated and by eliminating time in the stress and strain equations, stress-strain curves can be obtained as well.

2.5.1. Theoretical Limits on Strain Rate

Many design considerations can be taken into account to maximize the strain rate of the Hopkinson bar. However, there are practical and theoretical limits on the uppermost attainable strain rates. The generally accepted theoretical upper limit for a

Kolsky bar is about 10^4 s^{-1} , though actual limits are far less. This can be inferred from the relation provided by Hartley et al in [76] as follows;

$$\dot{\gamma}_s = \frac{1}{\rho c L_s} \left[2\tau_i \left(\frac{D_s}{D} \right) - 8 \left(\frac{D_s}{D} \right)^3 \left(\frac{2t_s}{D} \right) \tau_s \right]. \quad (42)$$

From the above relationship it is evident that the most significant influencing quantity comes from the right side of the equation within the square brackets - the specimen gage length. By shortening the gage length one will maximize this quantity.

Earlier it was mentioned that a few of the assumptions made by Hartley *et al* for simplicity were not followed to facilitate a higher degree of accuracy. An important addendum to the aforementioned decision is that a further means of decreasing inhomogeneity during the test is to increase the gage length. Though this does decrease the strain rate, it ensures an increased stability with the test conditions, specifically the strain rate. The reasoning behind this is that as the gage length is shortened, the strain rate will increase noticeably. At the same time, end effects become far more significant and the strain rate increasingly less uniform, resulting in erratic results and material behavior, as well as tested samples unsuitable for metallographic analysis.

The second term that can be modified to maximize strain rate is the diameter of the test specimen. Due to physical limitations imposed by the specimen holder, D_s/D , or the specimen diameter over the bar diameter has a limiting ratio of unity.

A high yield stress bar material will also increase the strain rate, but introduces many significant logistical difficulties. The beneficial aspects come from the fact that

the amount of stored torque can be significantly increased by using an alloy steel bar. However, two detrimental factors come into play when contemplating using a steel bar. Firstly, the mass density, ρ , in steel is approximately three times that of aluminum. Therefore in order to be able to realize any of the advantages associated with using a steel bar, its yield strength must also be triple that of aluminum. Otherwise there will be no increase in the strain rate. Secondly, the same problem posed when attempting to clamp and restrain an aluminum bar are present when clamping a steel bar. The critical difference being that if using a steel bar, the torque would be three times greater than in aluminum, requiring three times the clamp pressure. This, extremely intensified, radial pressure on the bar may lead to the introduction of radial and axial pulse components due to the sudden deletion of Poisson's effect upon release of the clamp.

Increasing the radius of the bar is a relatively insignificant modification, as can be inferred from equation (42), and not worth the additional effort when considering the return on investment. To effectively acquire upper limit strain rates above 10^4 1/s, and still have reliable data, an alternate testing system such as double shear, punching or plate impact must be utilized.

Lower limits from the strain rate are in the vicinity of 10^2 1/s. This is because a lower strain rate could not be held constant through the entire test. In order to approach a constant value of strain, the reflected pulse is required to remain constant. This condition, in turn, requires that the incident pulse be significantly larger than the transmitted pulse. Though the effect varies depending on the work hardening rate of the material, the end result is a lower limit of strain rate imposed upon the Kolsky bar.

2.5.2. Practical Limits on Strain Rate

Having seen the theoretical limits of the split-Hopkinson bar, it is important to understand why the practical limits of the strain rates reported within this thesis are less than 1000 1/s.

The first step is to start with the equation which governs what the maximum strain rate will be based on bar input capacity static analysis;

$$\dot{\gamma}_{\max} = \frac{2cD_s}{L_s D} \gamma_{\max} \gamma_{\text{unload}} \gamma_{\text{transmitted}}$$

As shown, the equation represents the maximum strain rate for the current configurations set-up. As is shown, the strain energy of γ_{\max} is not completely transferred to the specimen, as was assumed in the theoretical analysis. Exactly 1/2 of the energy is lost to the unloading pulse detailed in Chapter 2. In addition, depending on the hardness of the sample, approximately 1/2 of the remaining load pulse energy is passed right through the sample to the transmitter bar. This results in approximately 25% of the maximum strain energy being absorbed by the sample for deformation. Finally it is not recommended to operate the bar at the maximum load value due to the poor fatigue resistance of aluminum, if prolonged bar life and accuracy are desired. For this reason the input load was restricted to 60% of maximum capacity.

The resulting equation is;

$$\dot{\gamma}_{\max} = \frac{2cD_s}{L_s D} \gamma_{\max} \cdot \frac{1}{2} \cdot \frac{1}{2} \cdot 0.6 \quad (43)$$

based on the current set-up;

$$\dot{\gamma}_{\max} = \frac{2 \cdot 3139 \frac{m}{s} \cdot 13mm}{4.953mm \cdot 25.4mm} \cdot 5380\mu\gamma \cdot \frac{1}{2} \cdot \frac{1}{2} \cdot 0.6 \quad (44)$$

$$= 533 \frac{1}{s}$$

This number compares well with the recorded strain rate values of approximately 400 - 500 1/s.

The easiest way to increase strain rate without major geometric changes to the existing sample or apparatus would be to replace the current 6061-T6 aluminum bar with a 7075-T6 bar. 7075-T6 has a yield strength over twice that of 6061-T6 and would therefore result in an increase of $\dot{\gamma}_{\max}$ by more than twice of what is currently realized. Adjustment of sample geometry would provide a further increase in the strain rate to a combined total of about 2000 - 3000 1/s. However, as mentioned previously, this would preclude the possibility of extensive metallurgical analysis due to the extremely small gauge section that would have to be utilized.

CHAPTER 3

PROCEDURE FOR EVALUATION

3.1. EXPERIMENTAL PROCEDURE

The material in this investigation is SPS-Plus, supplied by Atlas Alloys. The composition is similar to 4340. The composition of SPS-Plus is given in Table 2. Included for the sake of comparison is the composition of 4340 steel, as well.

The steel was ordered in 15.88 mm hexagonal bar stock, hereafter referred to as hex-bar, such that it would fit into the specimen insert with no significant amount of machining required.

The final dimensions of the specimen are as per the values given in Figure 26. The machining process consisted of first cutting a 17 cm length of the bar stock and drilling a 12.7 mm diameter hole through the center of it using a lathe. To ensure true centering of the hole, a centering drill was used to start the hole followed by a guide hole of approximately 7 mm in diameter, with the guide hole functioning to keep the roughing bit straight. The rough bit used was 12.30 mm in diameter and was bored all the way through the material. Final tolerance was then achieved by carefully utilizing a 12.7 mm reamer.

Material	C	Mn	Si	Ni	Cr	Mo
SPS -Plus	0.42	1.18	0.29	0.41	0.95	0.06
4340	0.40	0.85	0.20	1.80	0.75	0.25

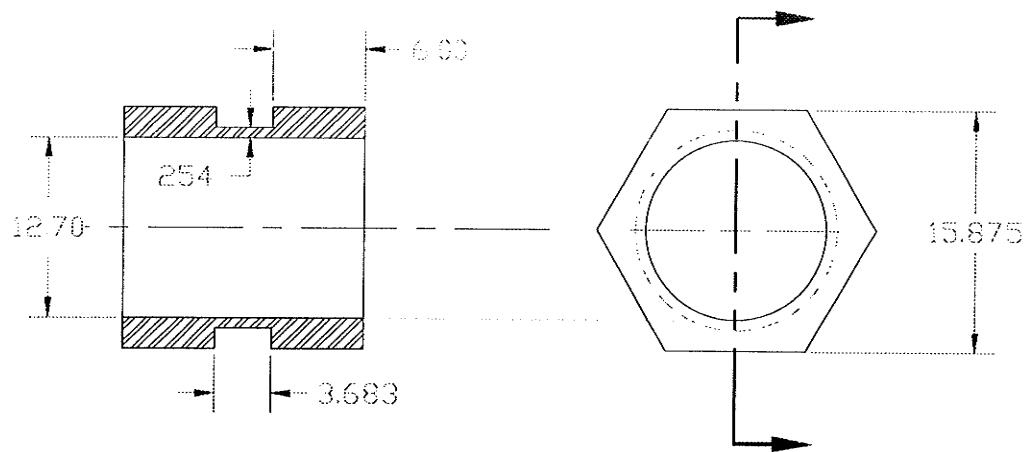


Figure 26: Specimen diagram. Dimensions in mm.

Upon completion of the hole being drilled, the specimens were notched with a custom designed notching tool that consistently cut 4.953 mm notches. Periodic checks of the outer diameter, while machining the notch, were made to guarantee a wall thickness of approximately 0.381 mm before final polishing.

All the critical polishing was done with the sample attached to the bulk of the material and still in the lathe. The turning speed was set to 1800 RPM and abrasive cloths and diamond paste were used in the same progression as in normal polishing to a surface roughness of approximately 8 μm . After polishing, the samples were ultrasonically cleaned, degreased and stored in a vacuum sealed desiccator until heat treatment.

3.1.1. Specimen Heat Treatment

For all the specimens that required heat treatment, a partially inclined 61 cm Marshal tube-type furnace was employed. The heat treatments used were as follows:

- Austenized at 850°C for 1 hour, air cooled.
- Austenitized at 850°C for 1 hour, oil quenched. Tempered at 315°C for 1 hour, air cooled.
- Austenitized at 850°C for 1 hour, oil quenched. Tempered at 480°C for 1 hour, air cooled.
- Austenitized at 850°C for 1 hour, oil quenched. Tempered at 650°C for 1 hour, air cooled.

Table 3: Pre-Test Statistical Data on Test Samples

Test Temperature	Sample	# of Samples	Mean Outer Dia. mm	Standard Deviation	Mean Wall Thickness mm	Standard Deviation
Room	A	3	13.37	0.04	0.34	0.02
	B	3	13.45	0.13	0.37	0.06
	C	3	13.47	0.08	0.39	0.04
	D	3	13.34	0.05	0.32	0.03
	E	3	13.31	0.18	0.30	0.09
-30°C	A	3	13.39	0.02	0.35	0.001
	B	3	13.48	0.14	0.39	0.07
	C	3	13.42	0.09	0.36	0.05
	D	3	13.43	0.13	0.36	0.07
	E	3	13.40	0.04	0.35	0.02
Overall Statistics =		30	13.41	0.09	0.35	0.04

Gage length for all samples = 4.95 mm

The aforementioned heat treatments, in addition to the as received condition, make up the full range of material conditions tested. Prior to heat treatment, the inclined furnace was flooded with argon for 20 minutes in an attempt to reduce the oxidizing atmosphere within as much as possible. In addition, the bottom of the tube was filled with titanium shavings to further reduce the harmful effects of oxidation.

Following cooling to room temperature, either by air cooling or the oil quench, the samples were again ultrasonically cleaned and degreased. In spite of all the precautions, there was always some oxidation or staining of the samples due to the high temperature oil quench. Thus some final touch-up polishing was always required. Final stage polishing was done by mounting samples on a 12.7 mm diameter shaft with a means of tightening the samples together, and then inserting the whole assembly into a lathe and repeat the last few grades of polishing cloth and diamond paste to reacquire the same finish achieved earlier.

Machining work was done before heat treatment such that any residual stresses due to the machining process would be removed. In addition, to ensure that the material failed within the gage length instead of along the corners, the notching tool automatically put a small radius along the edge of the gage section. Though extremely fragile and often difficult to obtain perfect samples from, the thinner gage section assured that there would be no variations in the heat treatment through the sample volume due to deep hardening limitations or variations.

3.1.2. Experimental Apparatus Instructions

When conducting the experiment, the most convenient method of describing the sequence of events is with an itemized list.

- Ensure the Jacking mechanism is at its lowest possible position and the release valve closed.
- The clamp load applicator is fully loosened and a notched load release pin inserted through the clamp and wrench tighten as much as possible.
- Tighten the load-applicator with the large wrench accompanying the split-Hopkinson apparatus $3/4$ of a turn.
- Zero all electronic equipment indicating the load within the stored torque region of the bar. This includes the readouts for the crank arm load cell and the strain gage at the mid-point of the length to be twisted.
- Load the jacking mechanism until the desired angle of twist is shown at the end of the bar, or the predetermined load is displayed on either the load cell or strain gage displays.
- Insert the sample between the incident and transmitter bars. Shave all burrs off the sample to ensure an unforced fit. Push the transmitter bar towards the sample and twist it clockwise (looking down the bar towards the clamp) to remove any slack that might exist at the interfaces between the specimen and either bar.
- Double check that all the Biomations wave form recorders are turned on, properly set and triggered for capturing data.

- Further tighten the load applicator until fracture of the load release pin occurs, thereby releasing the stored torque and inciting the test.
- Upon completion of the test, download each of the wave signals to the digital storage oscilloscope, which will in turn upload the file to the personal computer for final capture.
- Final manipulation is carried out automatically by an automatic pulse manipulating program.

3.1.3. Low Temperature Testing Procedure

To conduct low temperature tests the test sequence is essentially the same, with a few obvious additions. All the samples must have thermocouples spot welded to the inside edge of the hexagonal lug, as close as possible to the gage section as possible without actually contacting the surface. It is an acceptable placement for the thermocouple, as all the samples will be treated in the same way, keeping the level of consistency high.

The cooling source is a slightly pressurized dewar of liquid nitrogen. Cooling is obtained by aiming the nozzle of the pressure head attachment towards the sample and allowing a steady, controlled stream of N₂ gas to wash over the sample. By monitoring the temperature of the sample it is possible to adjust the N₂ flow to have a nearly constant temperature reading in the vicinity of -30 °C. Upon realizing the desired temperature, the test commences exactly as with the room temperature samples.

3.1.4. Varying Experiment Strain Rates

The most effective means of modifying the strain rate is to change the gage length of the test specimen. Equation 29 illustrates the theory behind this technique. L_g is the gage length term and is inversely proportional to the strain rate. It is important to realize, however, that by increasing the strain rate the surface of the specimen becomes increasingly small and difficult to salvage after the test for post mortem specimen analysis. The strain rate achieved was 439 1/s with a standard deviation of 102 1/s.

3.1.5. Post-Test Specimen Analysis Preparation

In order to conduct optical or electron microscopy of the gage section it is necessary to first remove the hexagonal lugs on either side of the test section. A slow speed diamond saw was used for this operation. Upon removal of the lugs, burrs left from the cut were ground off and the specimens cleaned in warm soapy water followed by an ultrasonic alcohol bath.

An unfortunate aspect of the lug removal process is the fact that in some instances the shear band and / or crack formation occurred quite far off center and close to the end - if not on the fillet itself. In these cases, care was taken to cut as close to the lug as possible, without damaging the deformed region. In spite of the care taken, however, some samples were left unusable after the procedure.

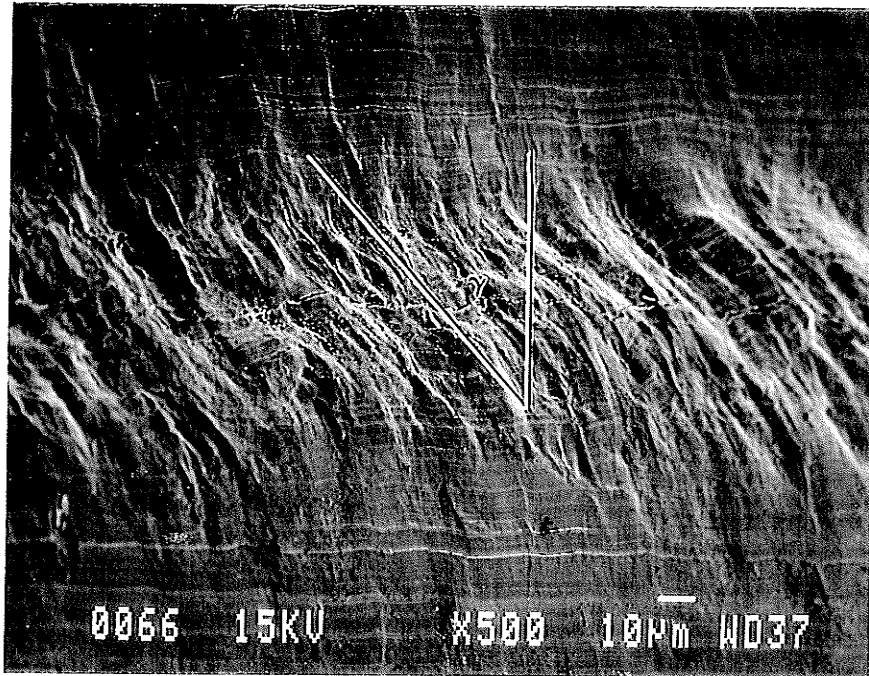


Figure 27: Illustration of the γ angle on a post-test specimen.

Upon completion of the gage length extraction and cleaning, the specimens were then observed under the Nikon Epiphot binocular optical microscope and the JEOL JXA - 840 scanning electron microscope. Once all the desired observations have been made with each system mentioned, the samples were subjected to a light 2% Nital etch. The examination process was then, once again, followed to obtain similar micrographs in the etched condition.

Determination of the local strain (strain within the shear band) was performed by taking the tangent of the angle γ as shown in Figure 27. ASB width was taken directly from micrographs. In totally sheared samples fracture was assumed to have taken place through the center of the band, allowing the measurement on one side to be doubled and represent the whole ASB. This was verified by analyzing both sides of a shorn ASB.

CHAPTER 4

VALIDATION AND EXPERIMENTAL RESULTS

4.1. EQUIPMENT FUNCTIONALITY

As required, the apparatus functions according to design. High strain rate tests can be obtained easily and consistently. The data are very clear and require very little post-processing to yield pertinent data. A wide range of material strength levels have been employed, each with reasonable results.

4.2. PRE-TEST SPECIMEN MICROSTRUCTURE

The five microstructures obtained for the various heat treatments were revealed using a 2% Nital etch. The various microstructures as observed in the scanning electron microscope (SEM) are documented in this thesis. The SEM micrographs are shown in Figures 28, 29, 30, 31 and 32. This redundancy is used such that drawbacks of one micrograph type could be compensated for by the other, and vice versa. In this section, the samples or micrographs may be referred to as A through E, inclusively, for the sake of brevity. Also, it should be noted that the five test conditions and corresponding Vickers hardness numbers (VHN) were as follows;

- A As received. VHN = 185.7
- B Annealed @ 850°C for 1 hour, air cooled. VHN = 209.2
- C Austenitized @ 850°C for 1 hour, oil quench. Tempered @
315°C for 1 hour, air cooled. VHN = 330.0

- D Austenitized @ 850°C for 1 hour, oil quench. Tempered @ 480°C for 1 hour, air cooled. VHN = 323.3
- E Austenitized @ 850°C for 1 hour, oil quench. Tempered @ 650°C for 1 hour, air cooled. VHN = 214.7

Figure 28 shows a typical coarse pearlitic structure with some ferrite outlining the prior austenitic grain boundaries. The lighter, almost featureless, smooth regions are ferrite. From examination of this morphology it can be inferred that the bar was hot rolled and slowly cooled, giving ample time for the formation of the lamellar pearlite shown. This, indeed, was the case for the as received bar stock - the first sample type tested.

Indicative of a higher cooling rate than what was used in the as received stock, Figure 28 shows the pearlite to be unresolved and of a very fine lamellar structure. The ferrite has formed at the prior austenite grain boundaries, just as in their specimens corresponding to Figure 28. In fact, closer examination of the micrographs in the aforementioned figures reveals that the ferrite structures are very similar in appearance. As initially mentioned, the increased cooling rate resulting from air cooling did not allow for the formation of a very coarse lamellar pearlite. Instead, the lamellae are very fine, and in some cases indistinguishable. Further justification for the aforementioned statements is derived from the fact that the "cell-like" pearlitic structures show resistance to the etchant while the surrounding ferrite is etched preferentially, as is expected [80].

Figure 29 shows a microstructure consisting of very fine and uniform lath type martensite with a few second phase particles interspersed within the matrix. Though

the precipitates were not examined in this sample, the presumably same, but larger, precipitates in Figure 31 were analyzed using EDS and were found to be high in magnesium, aluminum and oxygen. This microstructure is very similar to untempered martensite. By appearance alone the two would probably not be distinguishable.

It is believed that the early visible stages of tempering of the martensite is shown in Figure 31. Ferrite regions are being formed throughout the martensitic matrix, and are much more visible in Figure 31. The micrographs exhibit a visibly coarser microstructure than the one shown in Figure 30, and the precipitates have significantly increased in size and number. In addition, the martensitic cells appear to be increasingly segregated from each other with what is assumed to be ferrite [81].

The microstructure of the last specimen tested, shown in Figure 32, is just an extension of the changes noticed in Figures 30 to 31. The martensite has become very coarse and the grain boundaries compose a much larger fraction of the total area than is seen in 31. In fact, the ferrite is now much more uniformly distributed throughout the matrix. As a result of prolonged tempering the precipitates have probably become very large and fallen out of the sample during preparation.

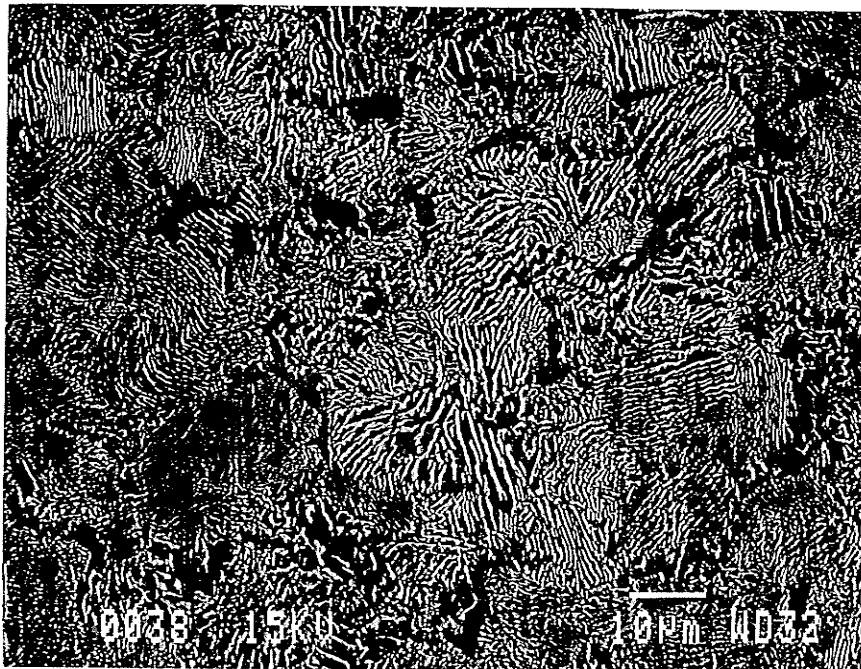


Figure 28: SEM Micrograph of Specimen A.

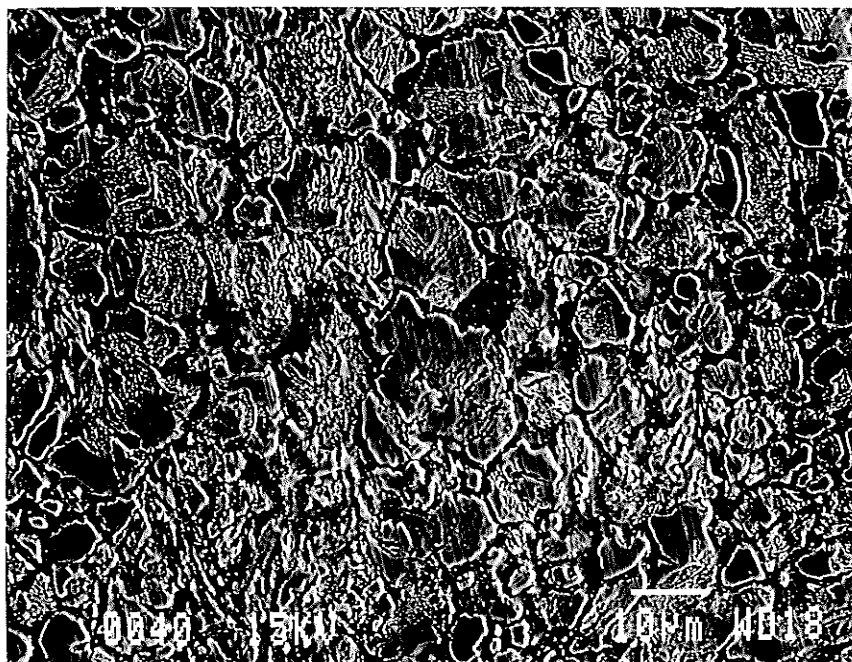


Figure 29: SEM Micrograph of Specimen B.

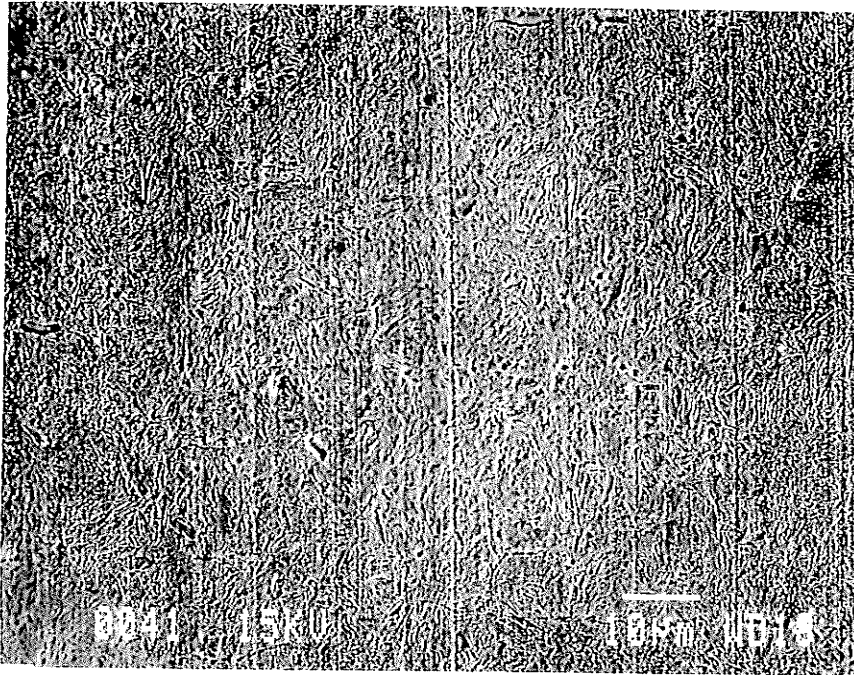


Figure 30: SEM Micrograph of Specimen C.

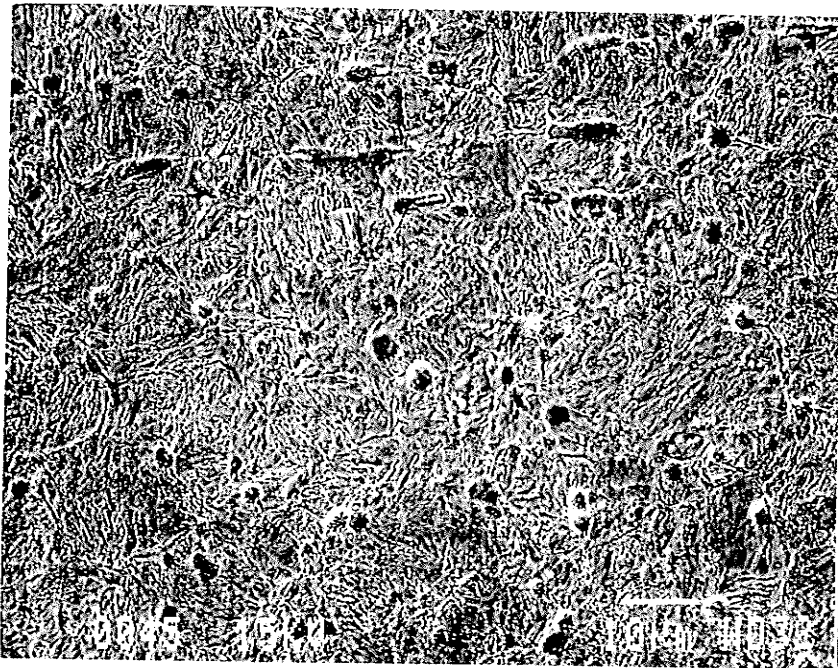


Figure 31: SEM Micrograph of Specimen D.

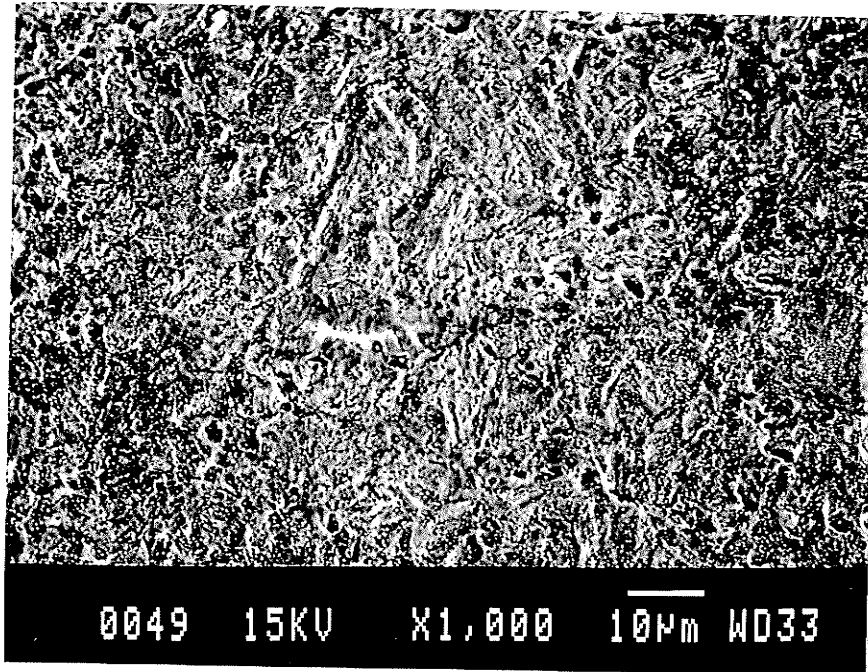


Figure 32: SEM Micrograph of Specimen E.

4.3. STRESS - STRAIN BEHAVIOR

The generally accepted form, with some variation, of a typical stress-strain curve is shown in Figure 33.

This figure is shown in order to validate the appearance of the curves to follow. In spite of the fact that the experiments were conducted at strain rates in the neighborhood of 500 1/s, the general appearance of high strain rate curves will still follow the classical elastic-plastic behavior of ductile to semi-ductile metals. Discernible yielding, upper shear and fracture points are all present in each of the curves presented in this thesis.

Details pertaining to the methodology of processing the raw data into stress - strain curves are provided in Chapter 2. Once all the samples had been post processed and their corresponding curves generated, one curve most indicative from each of the five sample types tested was selected. These five curves will be discussed for each, the room temperature and low temperature tests.

4.4. ROOM TEMPERATURE DYNAMIC TORSION TESTS

4.4.1. Stress Strain Curves

The first curve shown, Figure 34, corresponds to the as received, hot rolled, condition of the material. The curve shows a slight yield drop near the yield point, but is otherwise typical in its appearance. The ductility and strength values obtained from this curve are both average within the group, as demonstrated in Table 4.

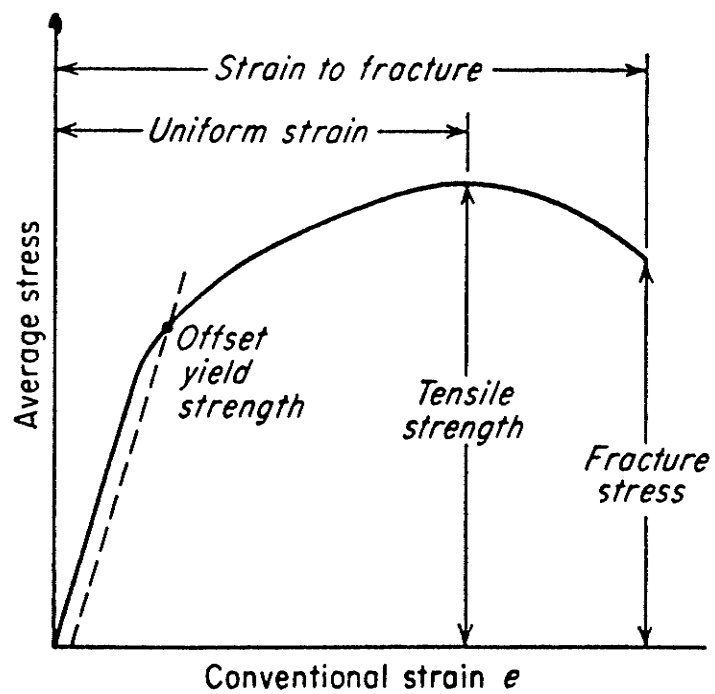


Figure 33: Typical Shape for a Stress Strain Curve [82].

The annealed material curve, Figure 35, is similar to the one corresponding to the as received condition. The ductility is slightly lower with approximately the same strength, as compared to the strength of the as received condition samples.

The stress-strain curve shown in Figure 36 takes a radical departure from the previously discussed two curves, but is still of an acceptable shape. The austenitized, oil quenched and tempered at 315°C specimen is typical of a very strong but brittle steel. There is limited plasticity following yielding, and the material possesses nearly double the shear strength of the first two sample types discussed above.

The steel which was austenitized, oil quenched and tempered at 480°C for 1 hour exhibited the stress-strain curve in Figure 37. As seen in this figure, this treatment resulted in improved strength and ductility compared to treatments A, B and C discussed earlier. This indicates that an intermediate tempering temperature is beneficial for this steel. The only drawback of this treatment would be the close proximity of the ultimate and yield strength.

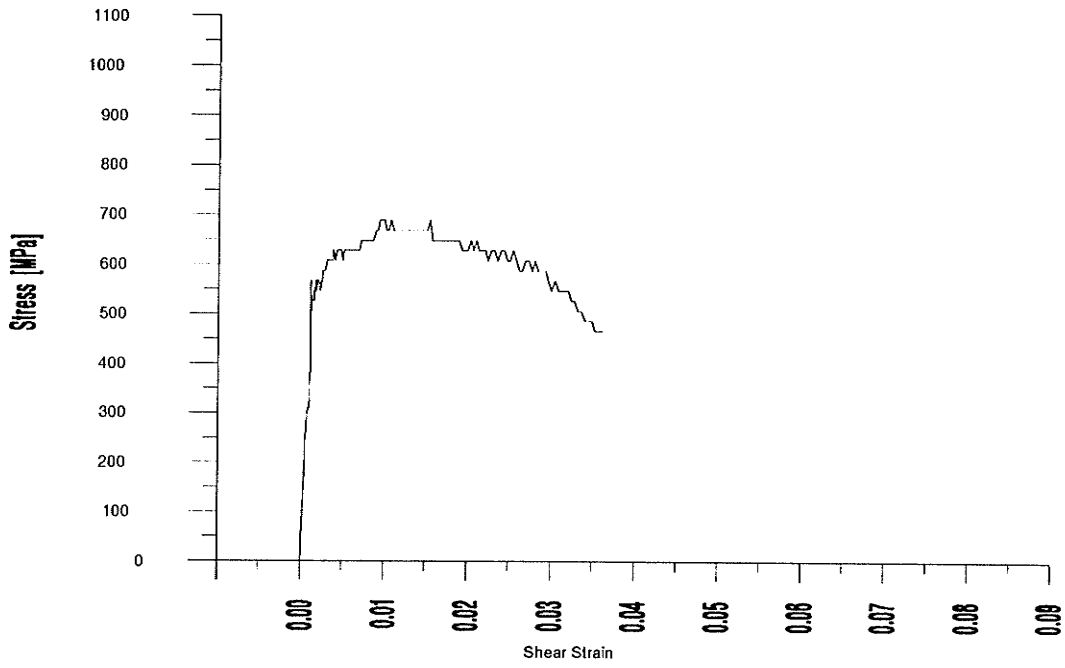


Figure 34: Stress - Strain Curve for A.

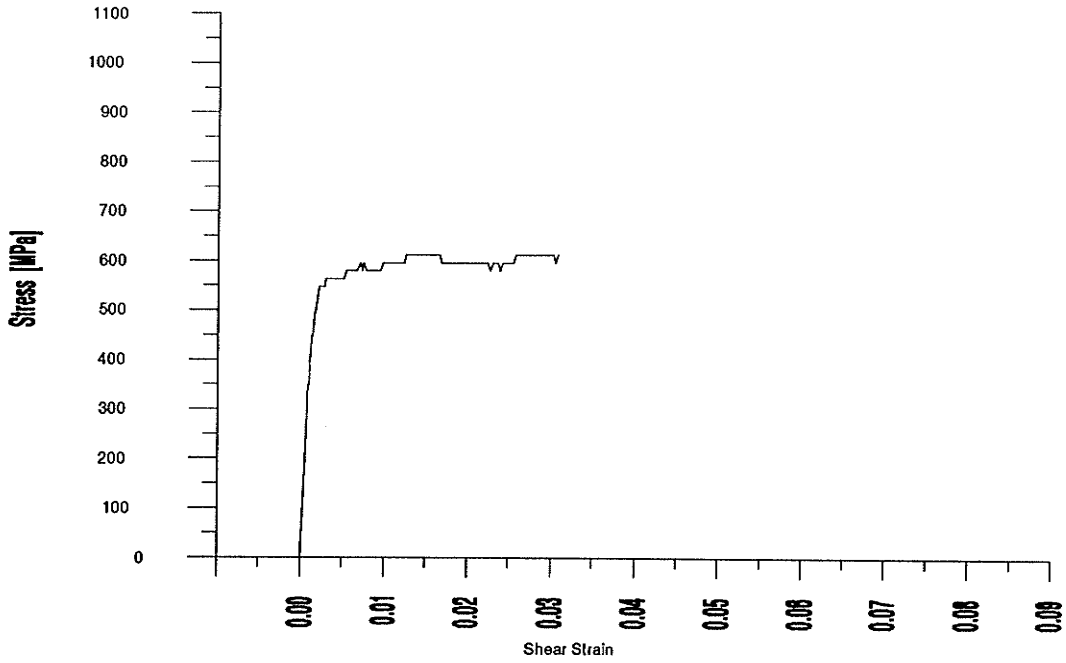


Figure 35: Stress - Strain Curve for B.

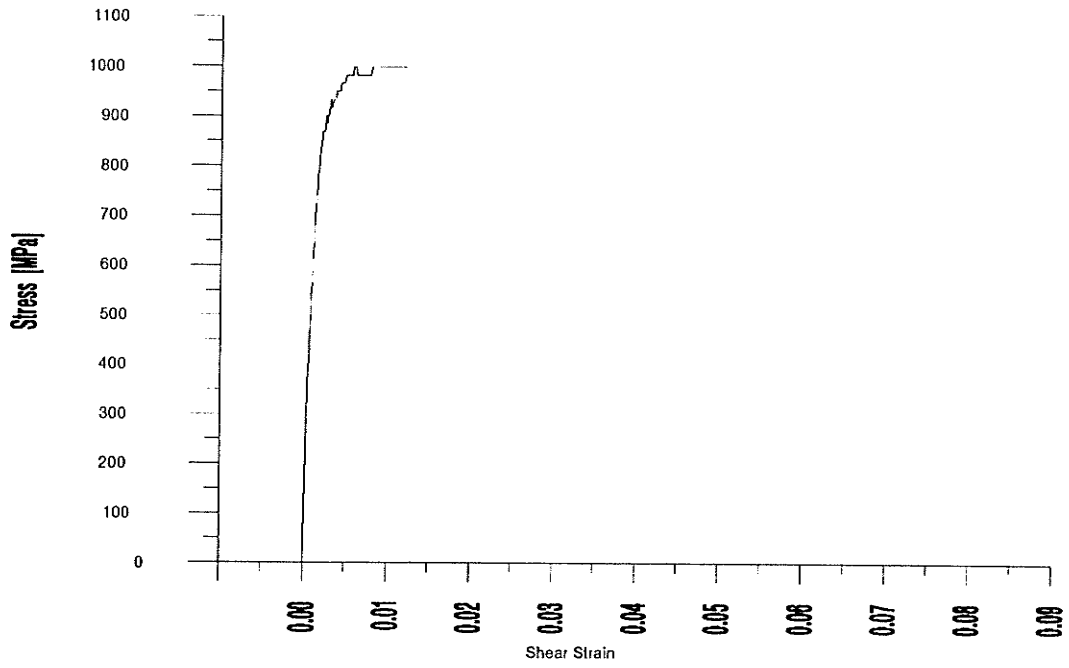


Figure 36: Stress - Strain Curve for C.

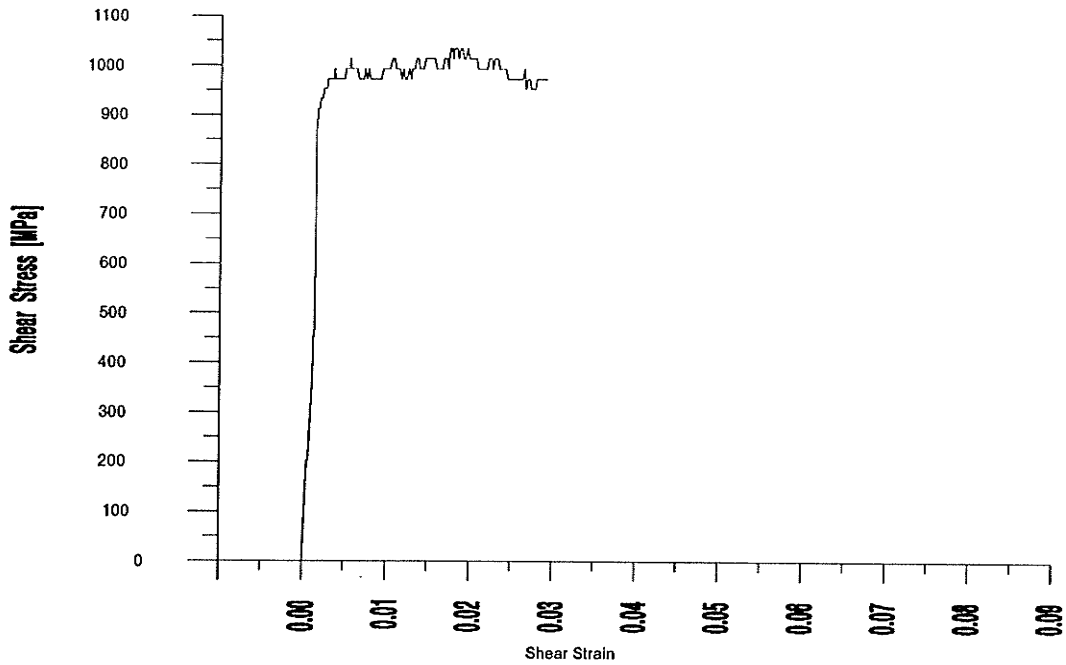


Figure 37: Stress - Strain Curve for D.

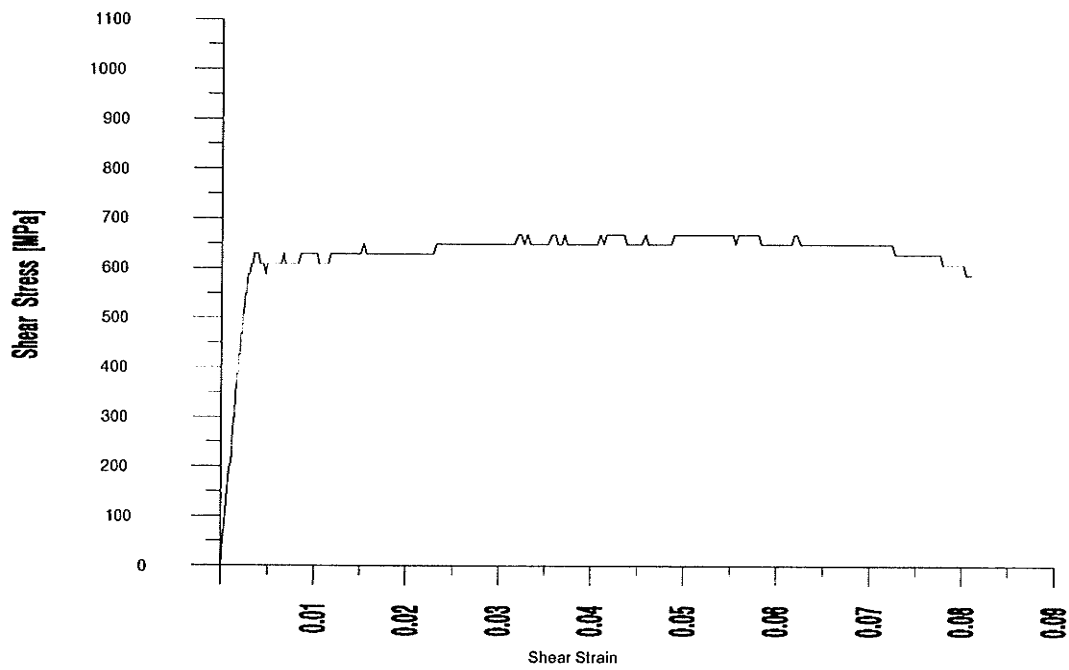


Figure 38: Stress - Strain Curve for E.

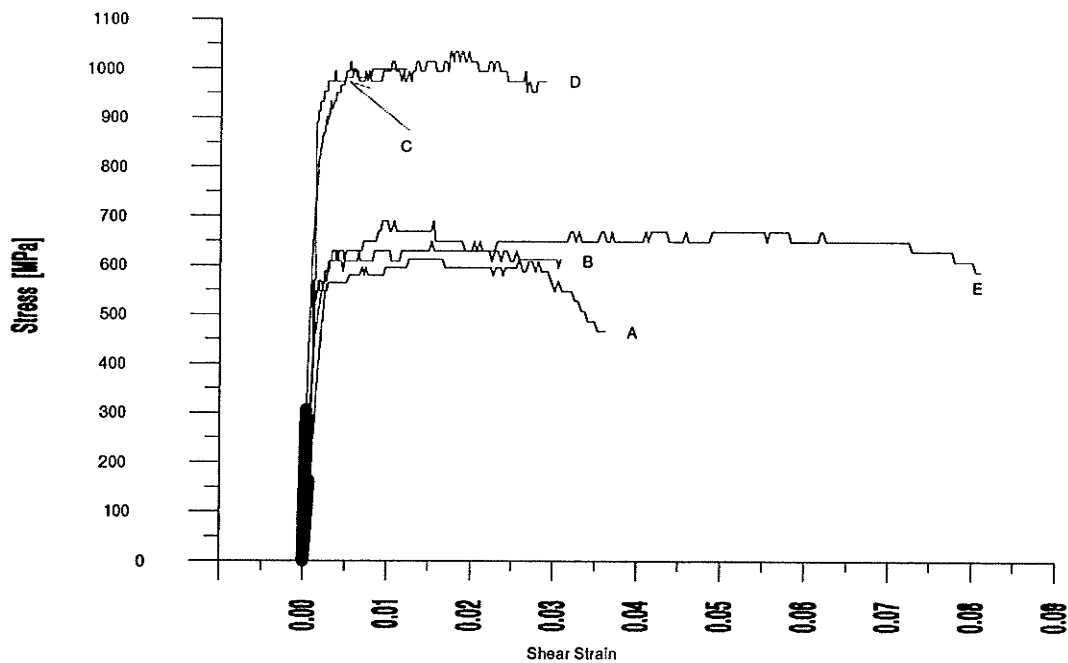


Figure 39: Stress - Strain Curve for all 5 Room Temperature Curves.

Figure 38 corresponds to the steel tempered at 650 °C following oil quenching from the austenitized temperature. In this material a drop in strength to the levels of samples A and B was observed, in exchange for considerable increased ductility - unique to all samples.

In order to be able to visualize more readily the relative performance of each of the sample types on the same scale, a composite figure consisting of all five samples is provided in Figure 39.

4.4.2. Mechanical Properties

The high strain rate data provided by the experiments are shown in Table 4. The effect of specimen hardness on the failure strain is shown in Figure 40. As shown, there is a gradual trend towards a decreased average specimen strain with an increase in material hardness, data presented includes both the room temperature and -30°C tests.

Table 4: A complete summary of the room temperature data accumulated

Condition	τ_{yield} MPa	τ_{ult} MPa	γ_{failure} %	γ_{local} %	ASB width μm	Vickers Hardness
A	535	565	5.0	274	60	185.7
B	613	840	3.9	97	50	209.2
C	675	930	3.4	274	10	330.0
D	640	758	5.5	188	15	323.3
E	520	580	9.7	248	63	214.7

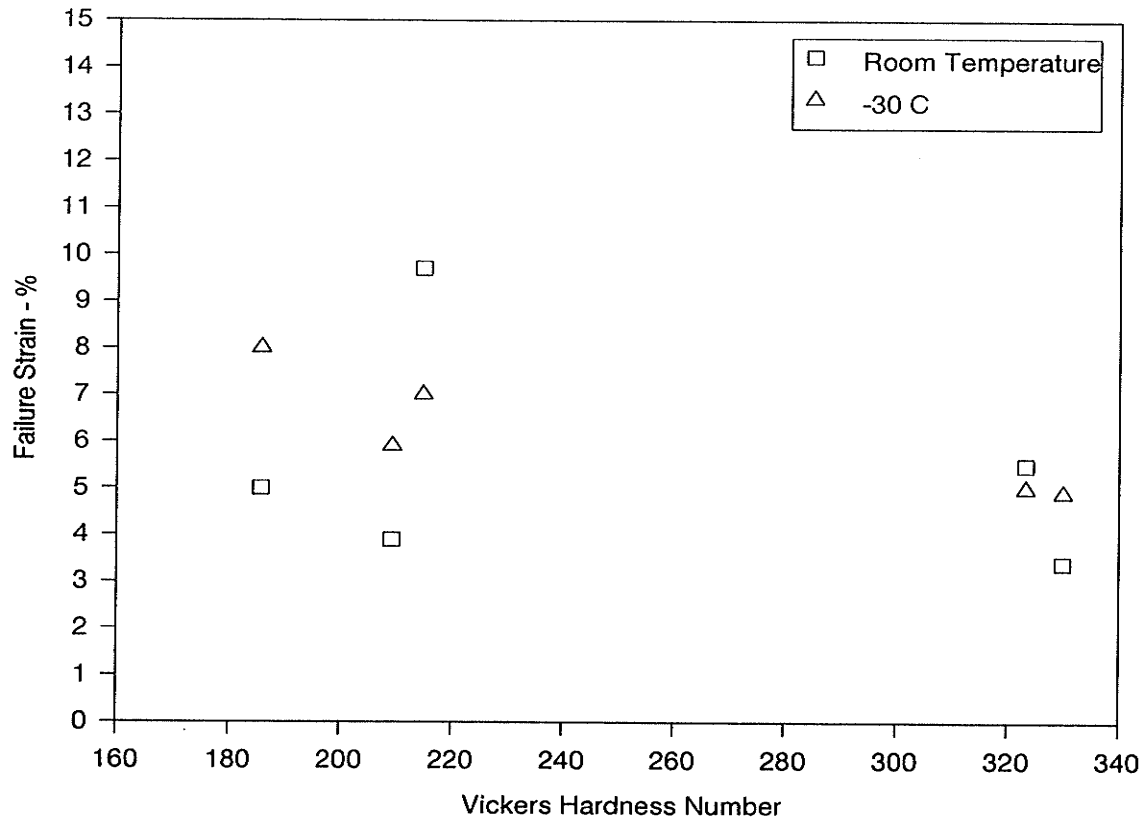


Figure 40: The effect of Specimen hardness on Failure Strain

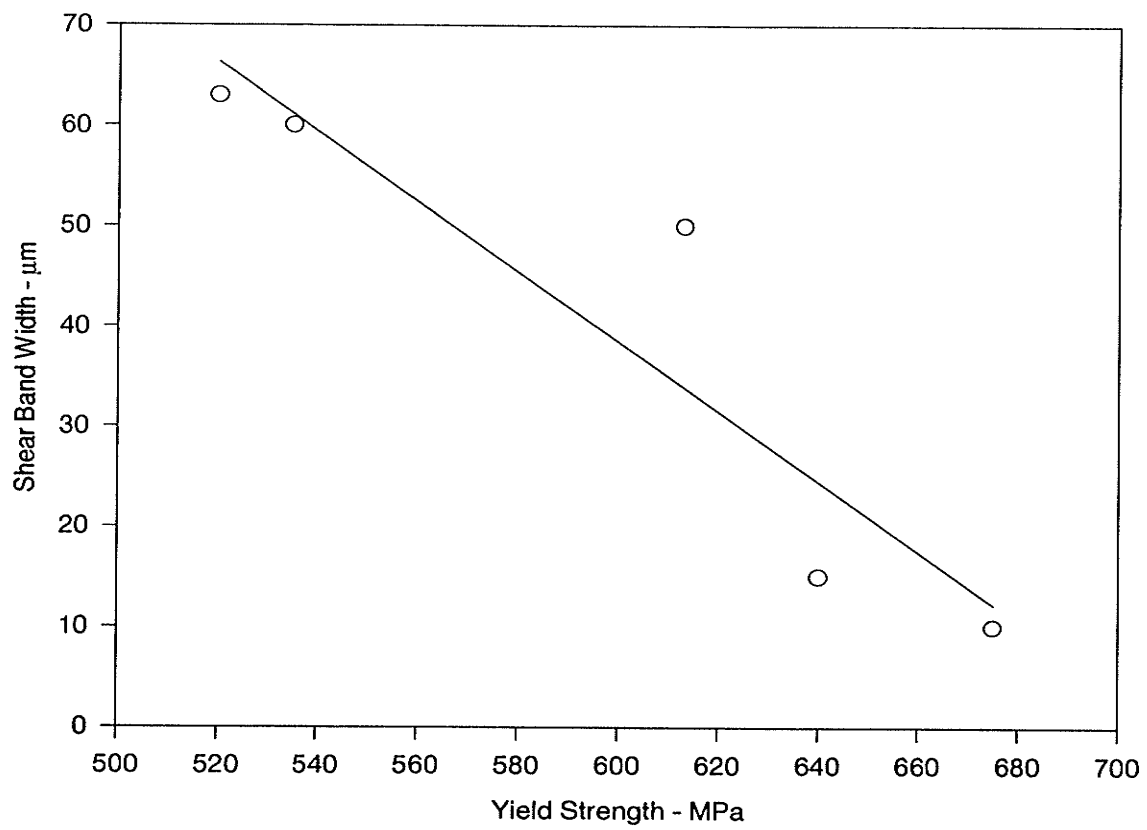


Figure 41: The effect of yield strength on the shear band width, at room temperature.

Another effect well illustrated graphically is the relationship between the yield strength of a material at room temperature and the adiabatic shear band width, at high strain rates, shown in Figure 41. Clearly, a higher yield strength results in a narrower shear band.

4.4.3. Morphology of the ASB Region

4.4.3.1. Unetched Specimens

In this section the shear banded regions are revealed more closely. One can see from Figure 42 that the shear banding was a gradual and spread out process. There seems to have been good flow and ductility, even within the shear band. Figure 42 displays shear bands reaching the maximum thickness found within the group under the circumstances of the applicable test conditions.

The annealed sample, Figure 43, does not seem to possess the uniformity of deformation found in sample A, Figure 42. The ASB seems to be cellular in its make-up and has deformed in such a way as to separate the cells from each other. The shear banded region is 50 μm , nearly as wide as was found in sample A, 60 μm .

Sample C, Figure 44, the quenched and 315 °C tempered steel, shows the narrowest ASB of the lot. The deformation was very localized and ultimately very brittle. The shear band itself, however, was uniform in topographical appearance.

Figure 45 displays how the segregation between cell-like divisions within the steel due to the onset of recrystallization and recovery are pronounced by the extensive deformation that takes place in these boundaries. The majority of the material deformation within the shear band is done along these cracks.

The shear band itself is very narrow, similar to that observed in C, with the material itself being very brittle. In the final sample (Figure 46) the shear band once again displays signs of a very ductile material and homogeneous deformation within the shear band. Generally, it is very similar to the ASB shown for sample A.

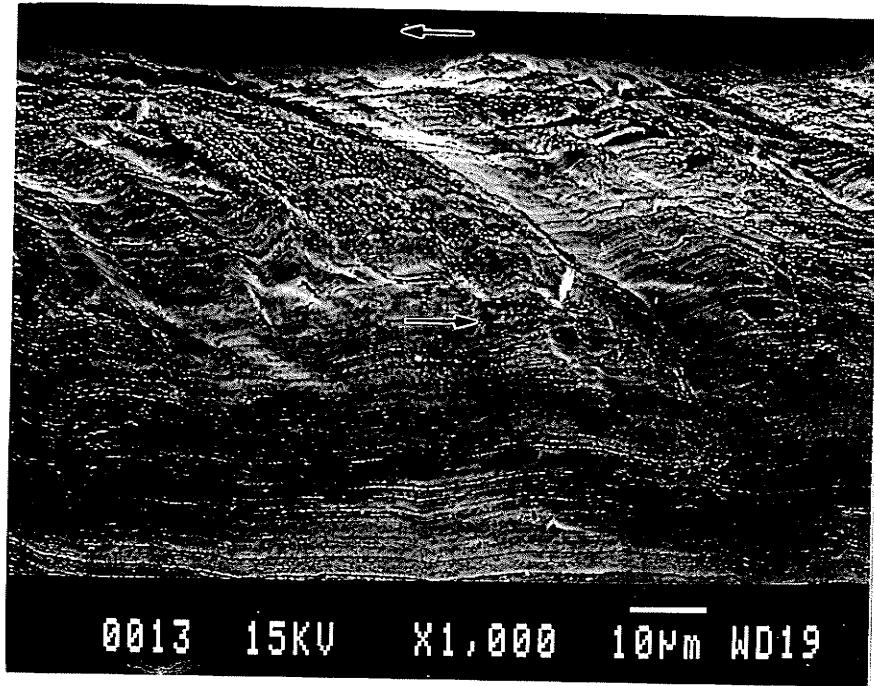


Figure 42: The unetched ASB for A.

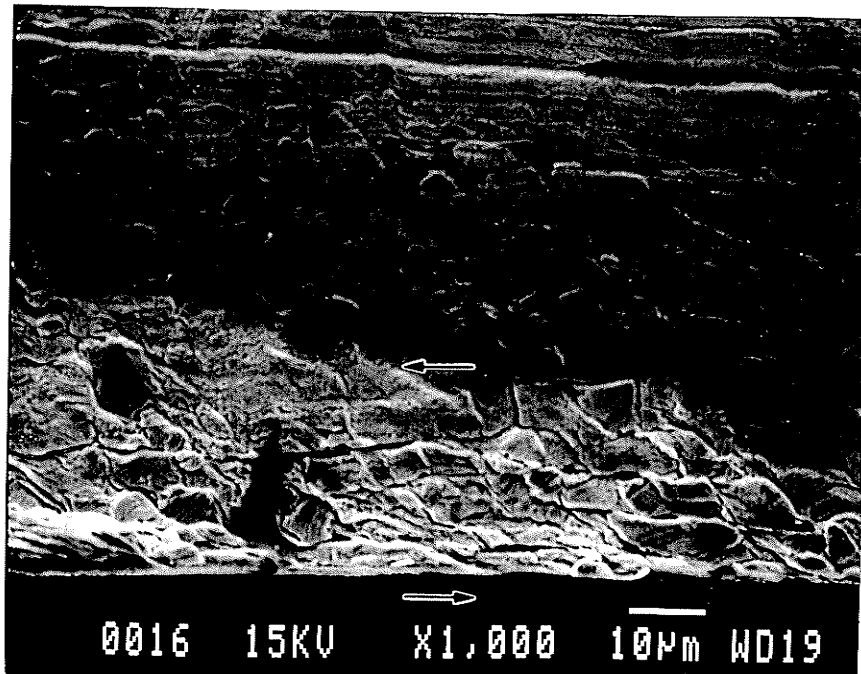


Figure 43: The unetched ASB for B.

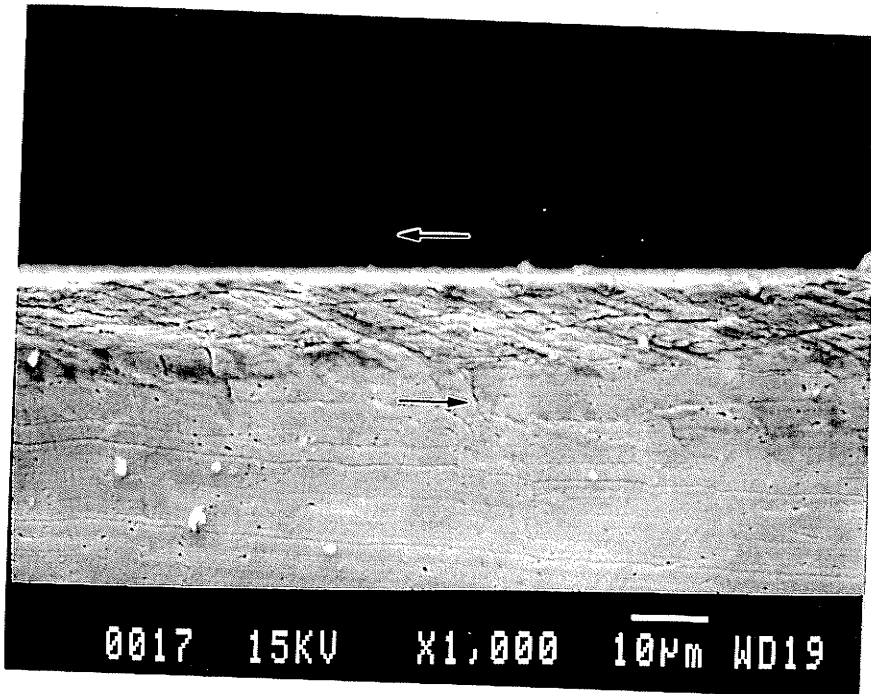


Figure 44: The unetched ASB for C.

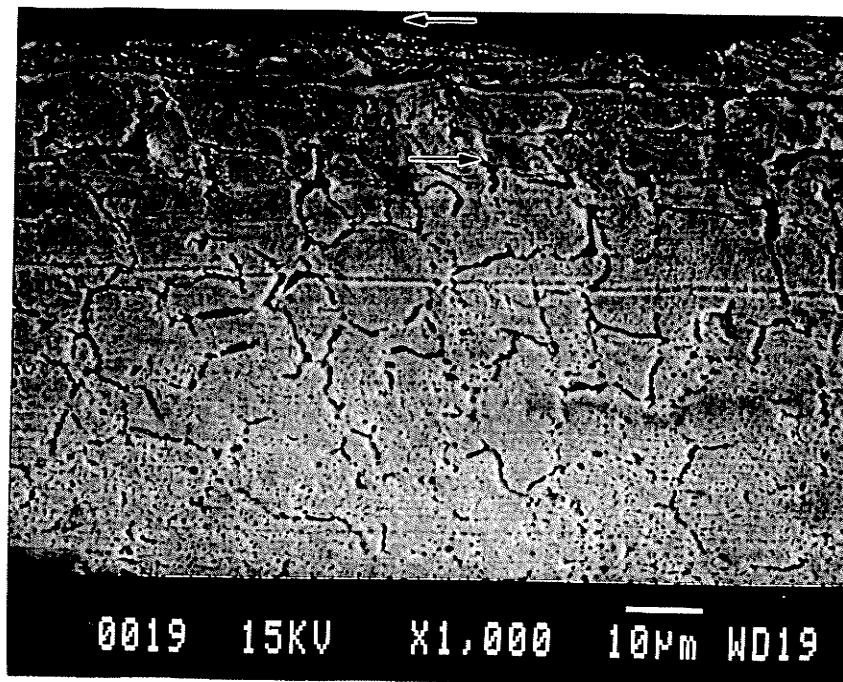


Figure 45: The unetched ASB for D.

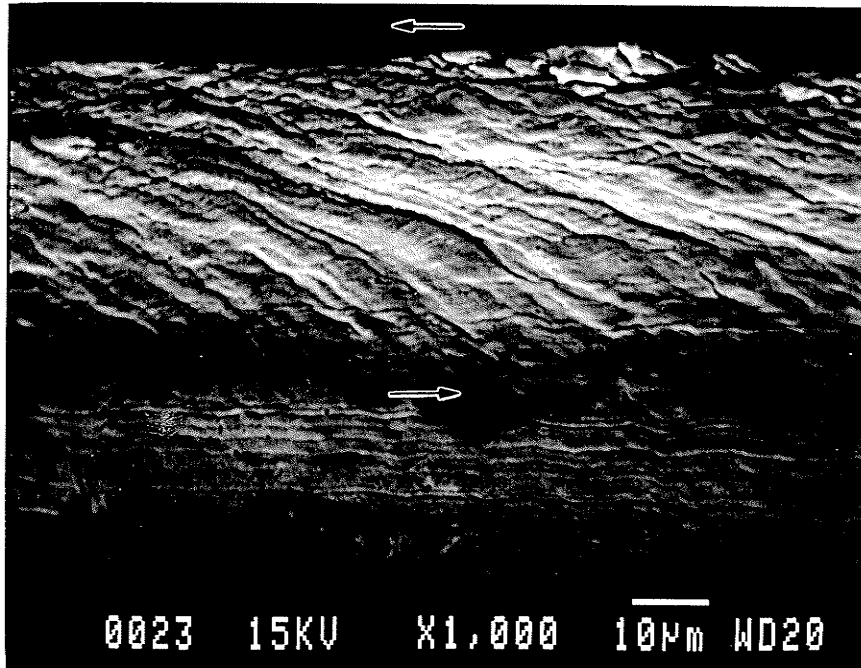


Figure 46: The unetched ASB for E.

4.4.3.2. Etched Specimens

Whereas the preceding section simply illustrated the macroscopic appearance of the adiabatic shear banded zones, this section will bring to the forefront *how* each of the shear bands is formed by revealing their etched microstructure. This enables one to see which components of the microstructure are more ductile than others, and how they interact with each other when severely deformed.

The widths of their shear bands have already been referred to and therefore they will not be discussed again here, since the etching process only affected the microstructures observed.. Except, perhaps, that the microstructures are generally pearlitic in nature for sample A and B, and martensitic in nature for C, D and E. These are shown in Figure 47 through 51.

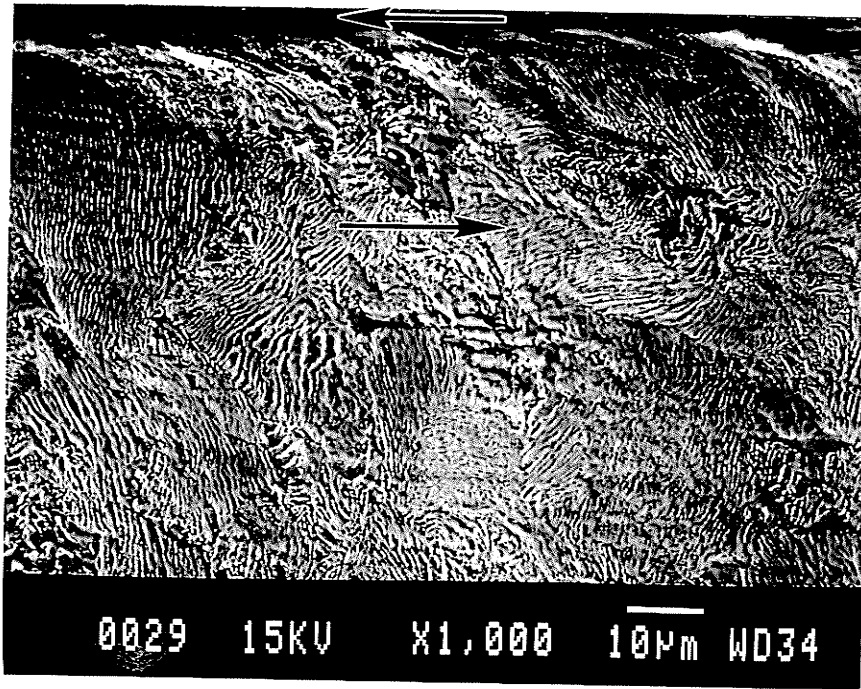


Figure 47: The etched ASB for A.

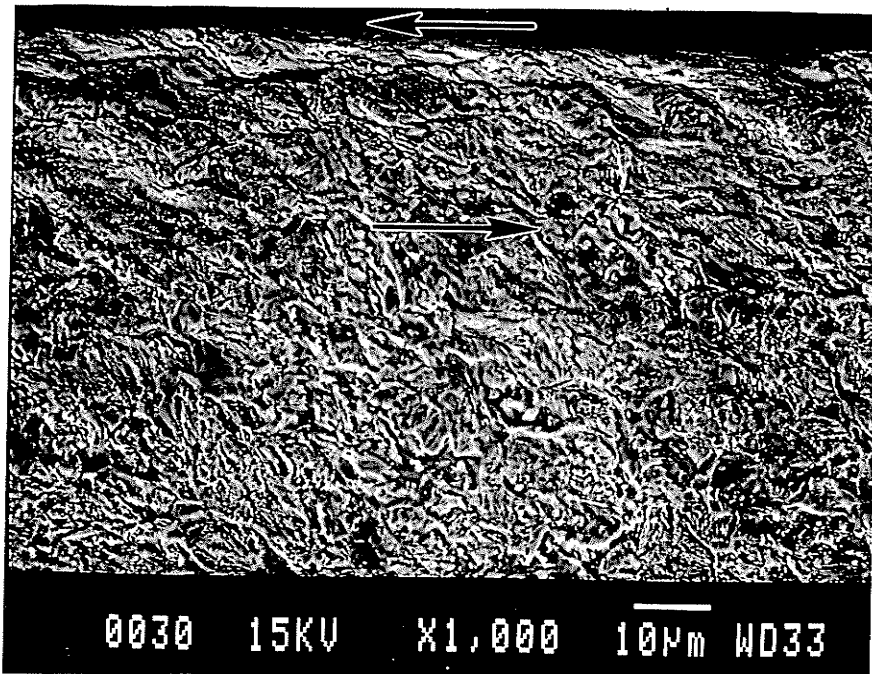


Figure 48: The etched ASB for B.

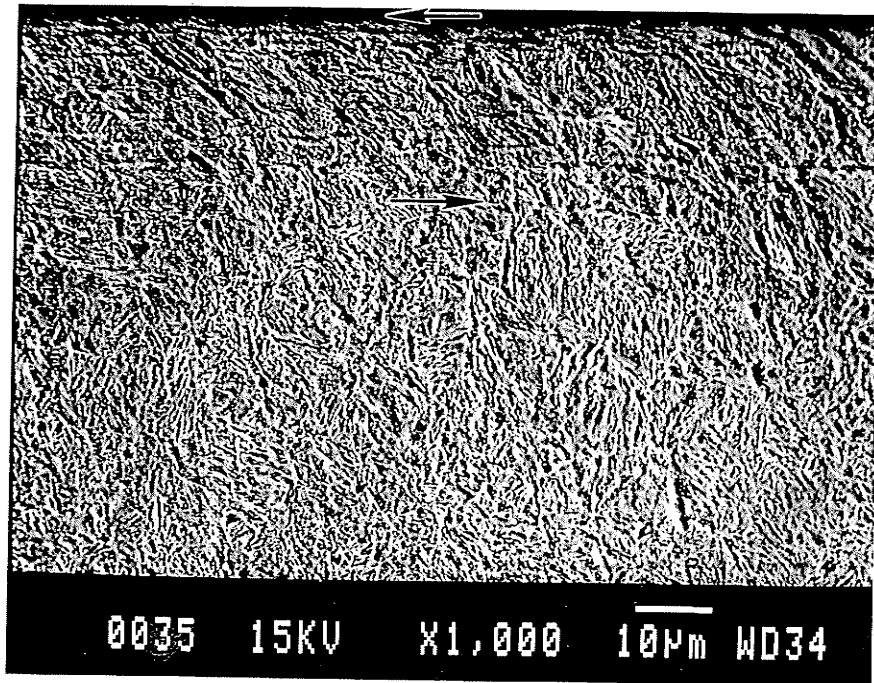


Figure 49: The etched ASB for C.

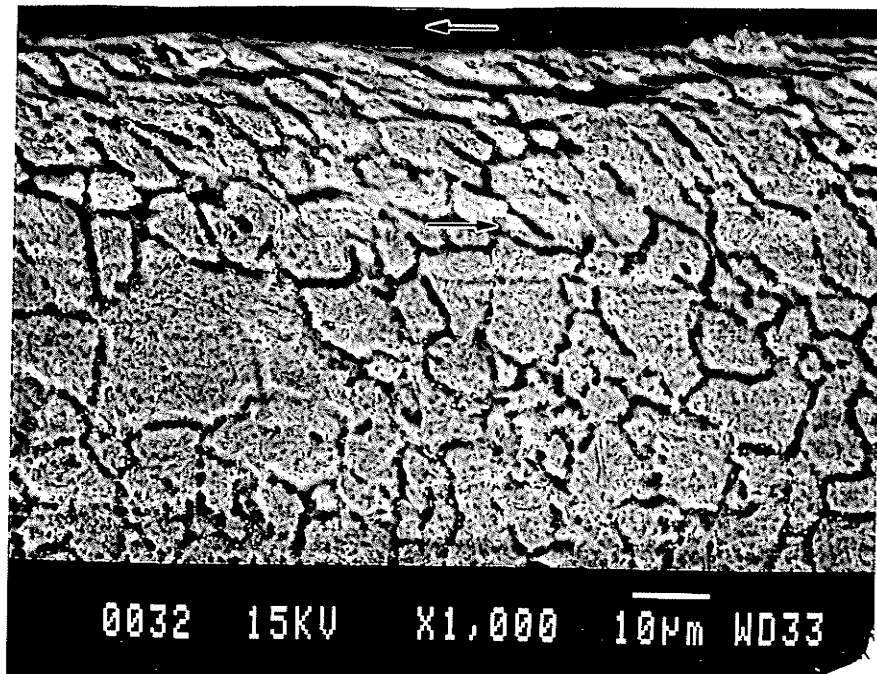


Figure 50: The etched ASB for D.

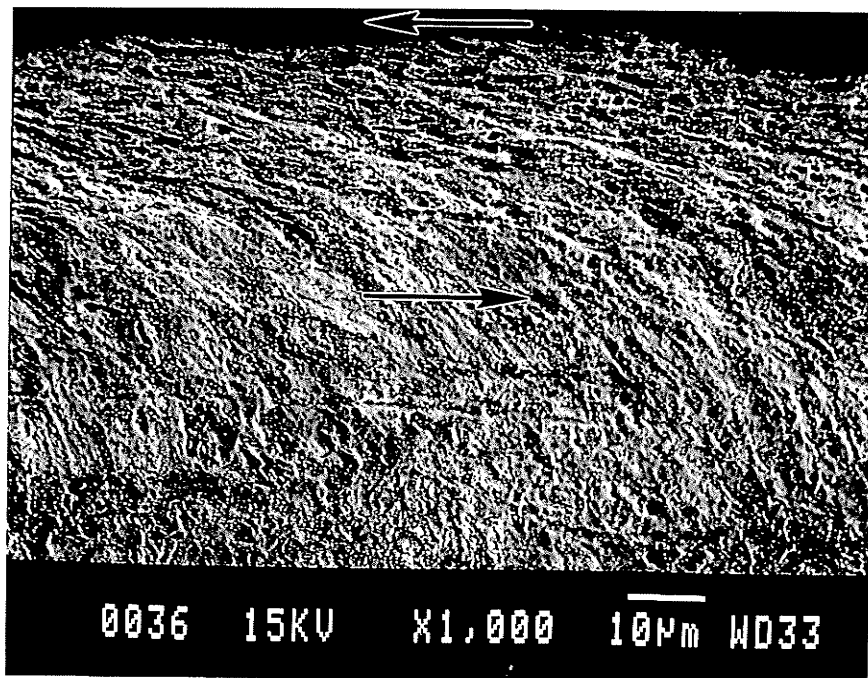


Figure 51: The etched ASB for E.

4.5. LOW TEMPERATURE DYNAMIC TORSION TESTS

4.5.1. Stress Strain Curves

In relation to the room temperature tests, the low temperature stress-strain curves are very similar in behavior and appearance. An interesting difference between the low and room temperature tests is that the scatter in experimental data between samples is somewhat decreased.

4.5.2. Mechanical Properties

Table 5 briefly summarizes the mechanical properties of the samples tested at -30°C. As mentioned previously, the results are basically congruent with the room temperature data, except the failure strain, which is somewhat larger.

Table 5: A complete summary of the -30°C data accumulated

Condition	τ_{yield} MPa	τ_{ult} MPa	γ_{failure} %	γ_{local} %	ASB width μm	Vickers Hardness
A	575	725	8.0	308	60	185.7
B	598	795	5.9	100	45	209.2
C	490	785	4.9	308	13	330.0
D	530	875	5.0	210	19	323.3
E	640	720	7.0	*	58	214.7

* No γ_{local} for sample E due to transformed nature of the ASB

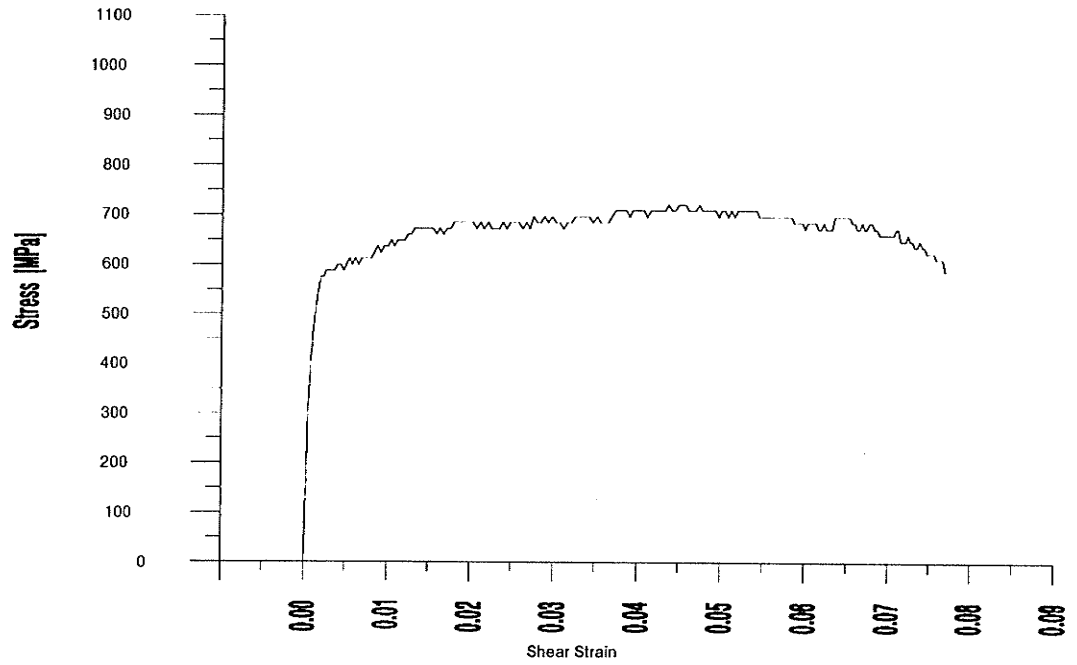


Figure 52: Stress - Strain Curve for A, -30°C.

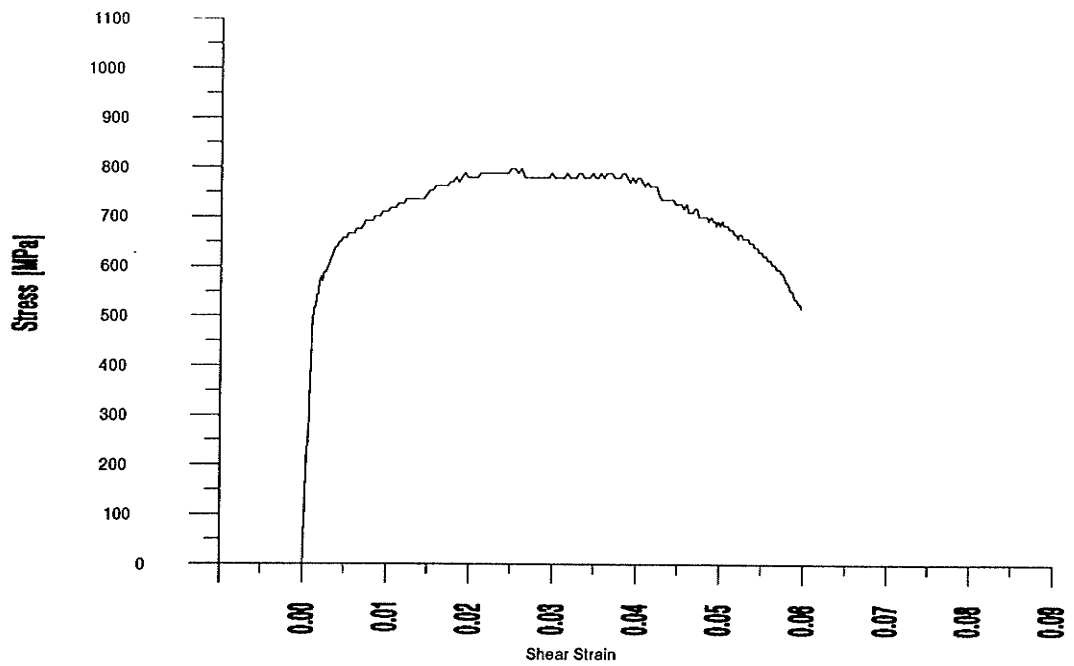


Figure 53: Stress - Strain Curve for B, -30°C

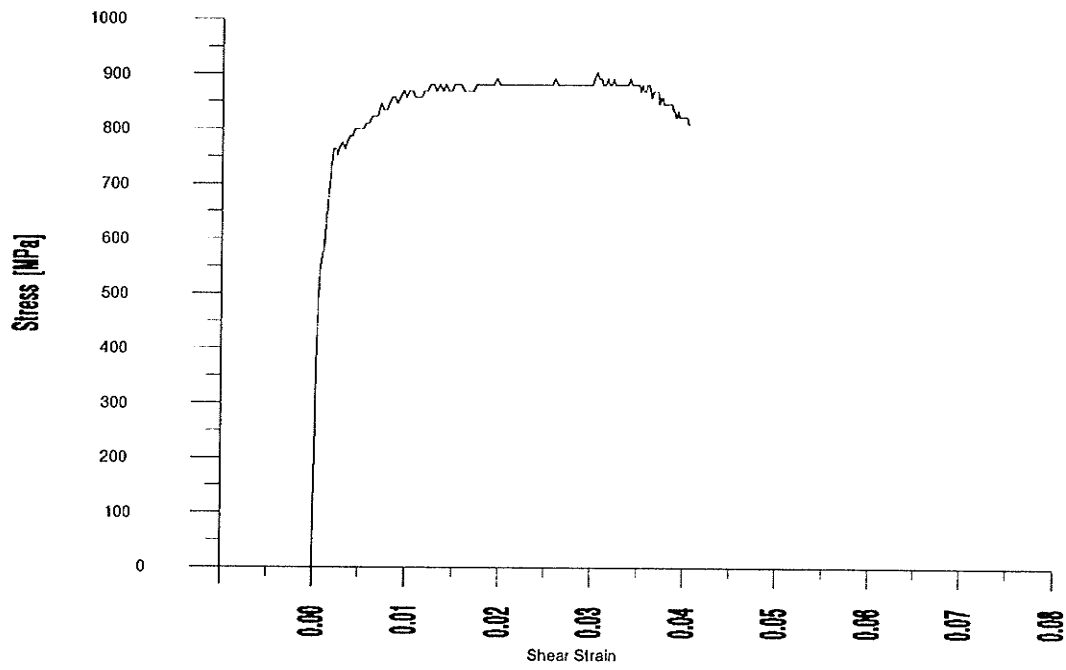


Figure 54: Stress - Strain Curve for C, -30°C

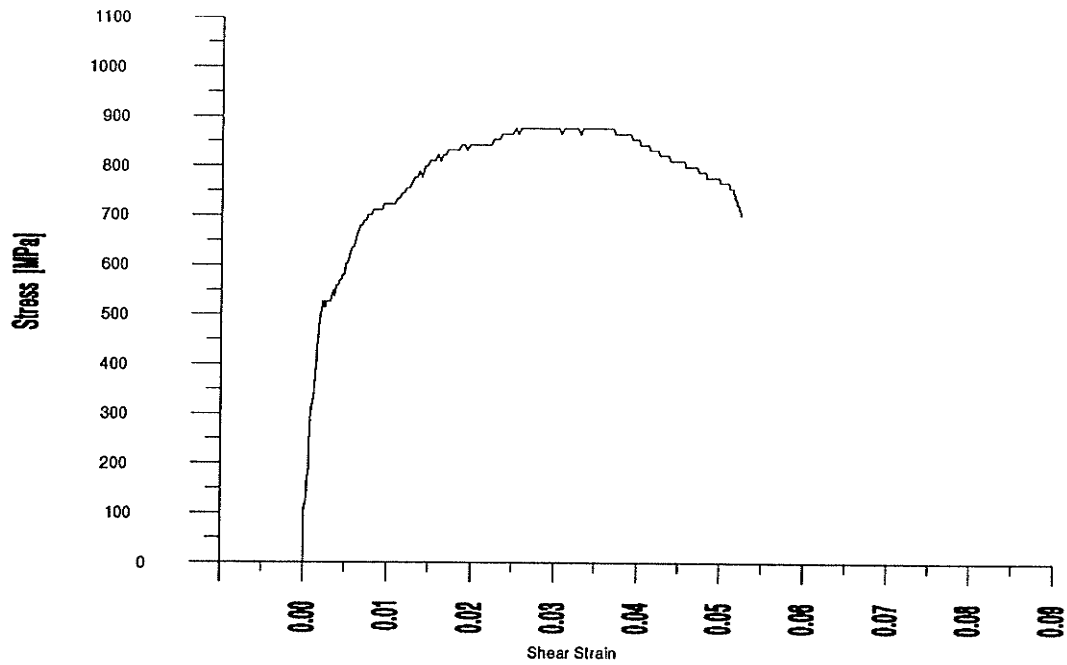


Figure 55: Stress - Strain Curve for D, -30°C

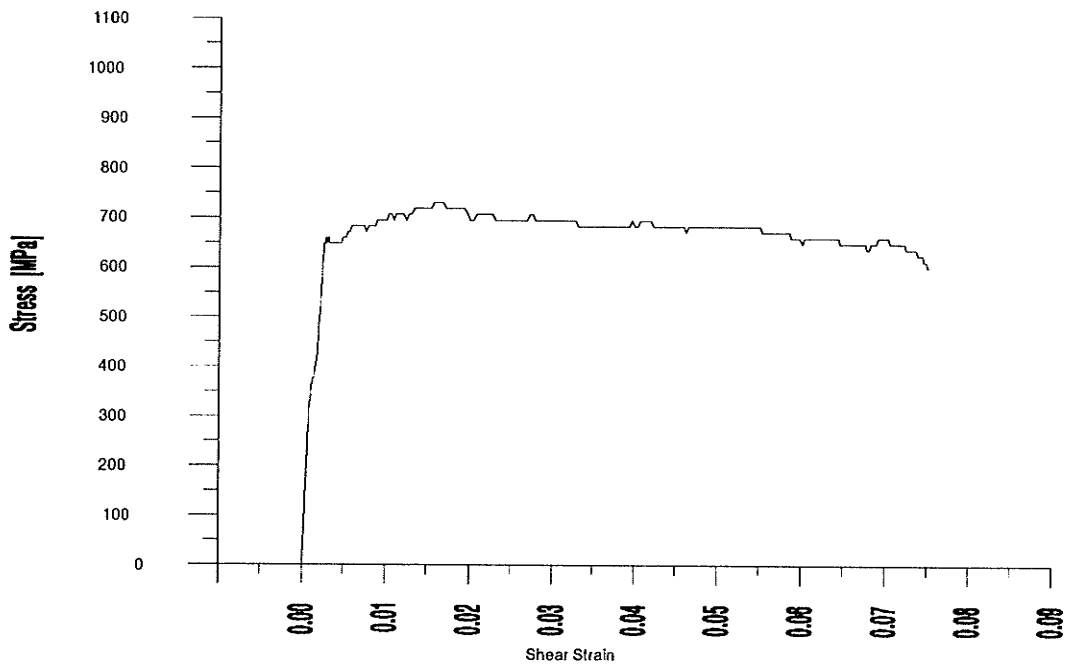


Figure 56: Stress - Strain Curve for E, -30°C

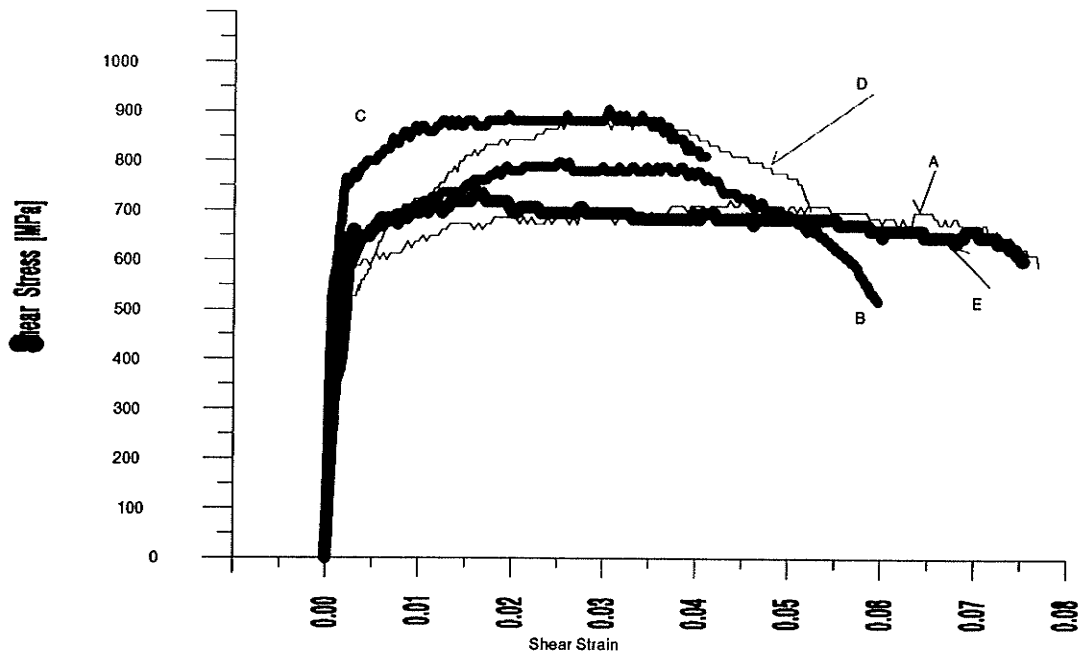


Figure 57: Stress - Strain Curves for all 5 samples, -30°C

4.5.3. Morphology of the ASB Region

4.5.3.1. Unetched Specimens

As was done for the room temperature tested sample, this section provides micrographs of the low temperature tested samples. The shear bands had roughly the same appearance as they did during the room temperature tests and need not be described again. There are only two significant differences between the room and low temperature test samples. The first being that the last sample, Figures 62 and 67, portrays shear band characteristics unlike and other sample tested, showing no visible signs of deformation within the ASB itself, and possessing a discrete boundary between the shear band and the surrounding matrix. The second difference is that the samples were less inclined to break during the test, and thus provided better samples to study the shear bands. In fact, the mean of the average or failure strains from all the room temperature tests was 5.5% with a standard deviation of 2.5. Conversely, the low temperature tested samples yielded a mean average strain of 6.2% with a 1.3 standard deviation. This represents a 12% increase in the mean average strain. Analysis of the mean local strains for both the room temperature and low temperature tests yields similar results, with an increase in values from room to low temperature tests being 11%. Interestingly, the shear band widths were within 1.5% of each other going from the room temperature to the low temperature. The trends are best presented in tabular format, Table 6.

4.5.3.2. Etched Specimens

In this section the etched version of the previously shown micrographs are examined. The shear bands are similar to the room temperature tests and are basically unchanged except for the aspects mentioned in preceding section.

Table 6: Mean and standard deviation values for room temperature and -30°C data

	τ_{yield} , MPa		τ_{ult} , MPa		γ_{failure} , %		γ_{local} , %		ASB width, μm	
	RT	-30°C	RT	-30°C	RT	-30°C	RT	-30°C	RT	-30°C
Mean	596.6	566.6	734.6	757.3	5.5	6.16	208.25	231.5	39.6	39.0
σ	67.01	58.42	160.01	117.7	2.49	1.33	84.52	99.09	25.26	21.87

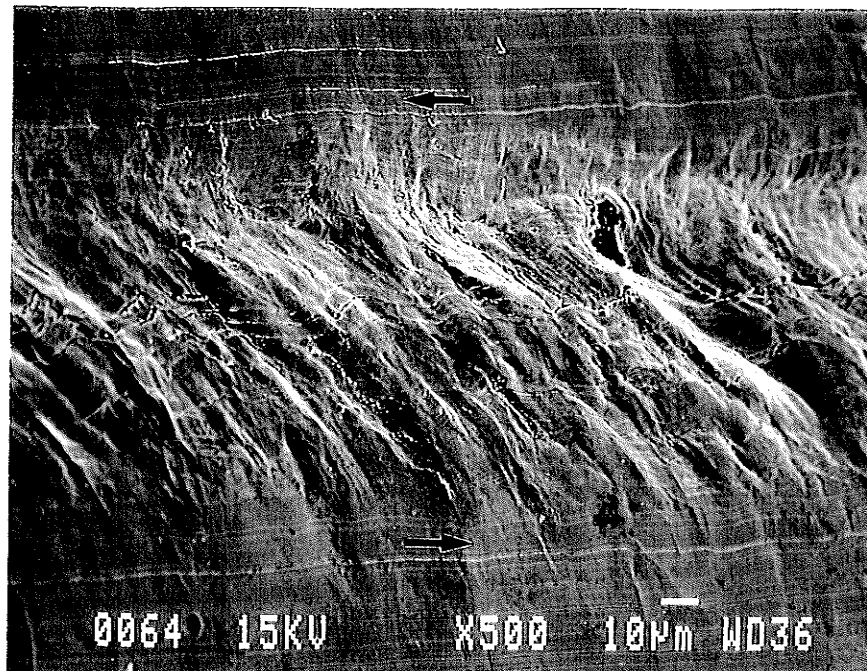


Figure 58: The unetched ASB for A, -30°C.

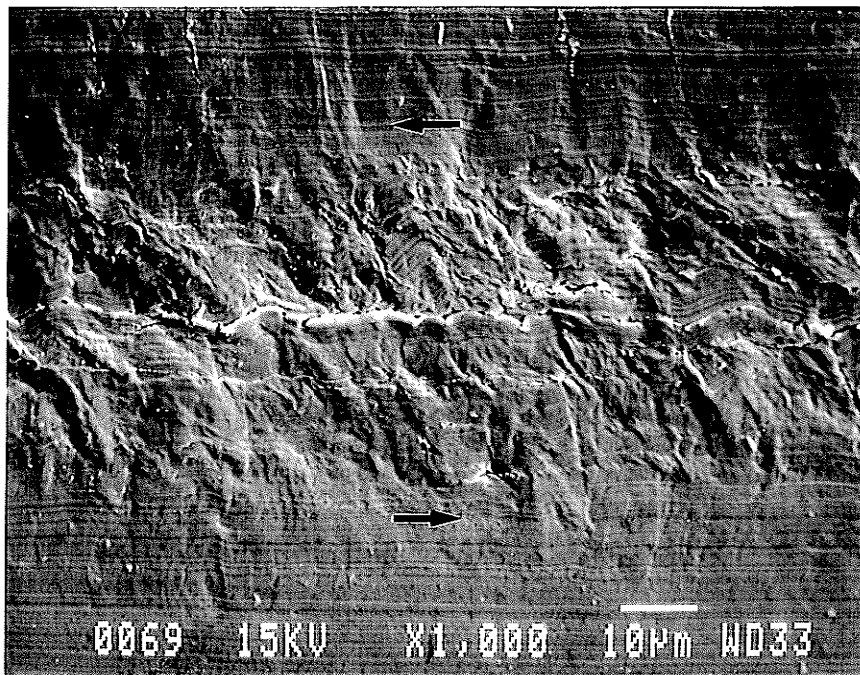


Figure 59: The unetched ASB for B, -30°C.

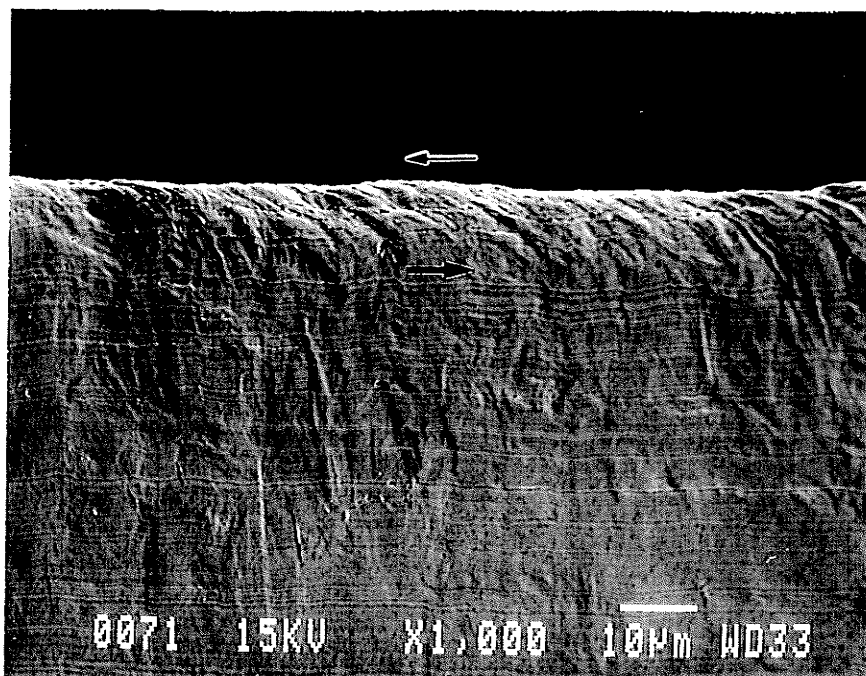


Figure 60: The unetched ASB for C, -30°C.

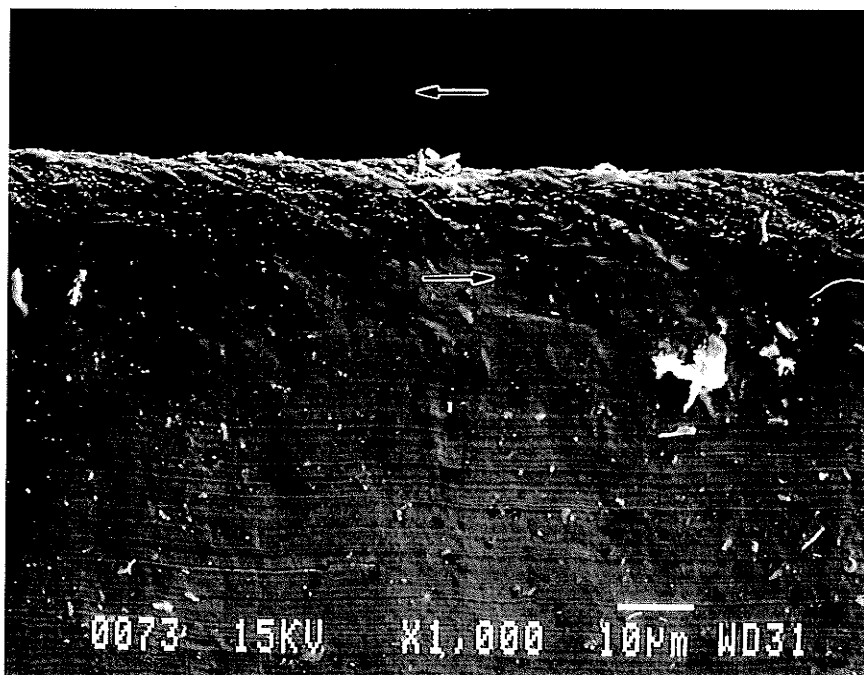


Figure 61: The unetched ASB for D, -30°C.

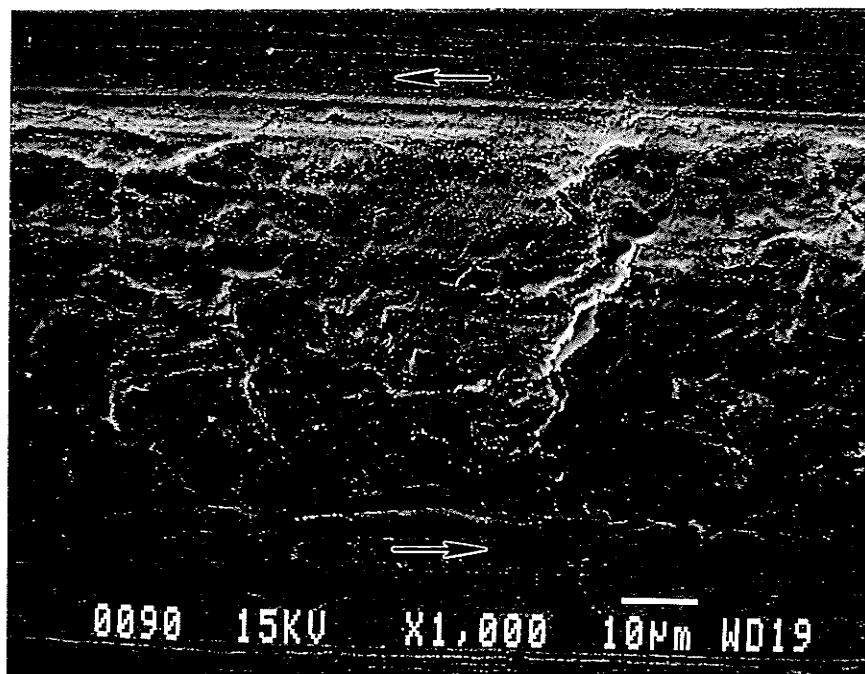


Figure 62: The unetched ASB for E, -30°C.

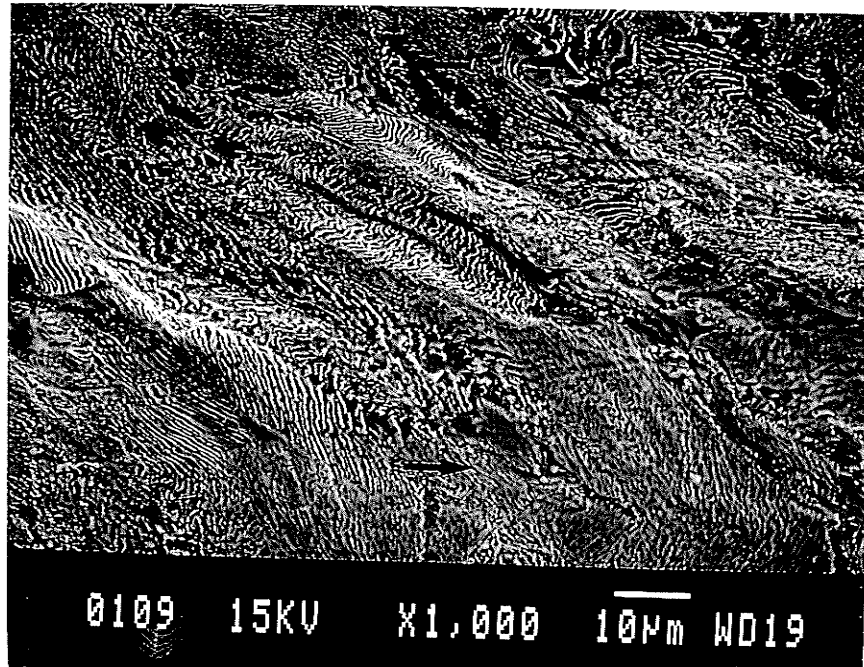


Figure 63: The etched ASB for A, -30°C.

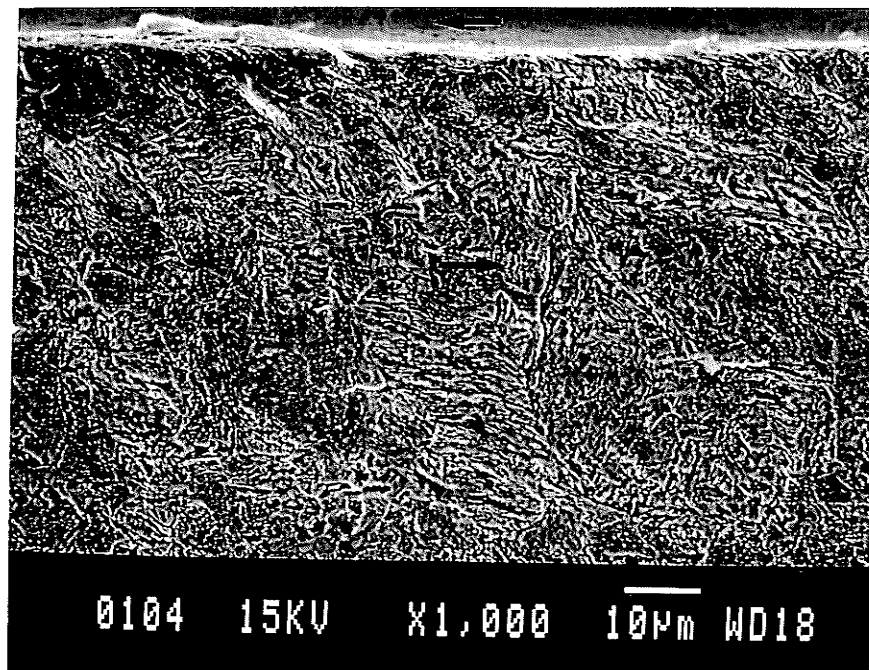


Figure 64: The etched ASB for B, -30°C.

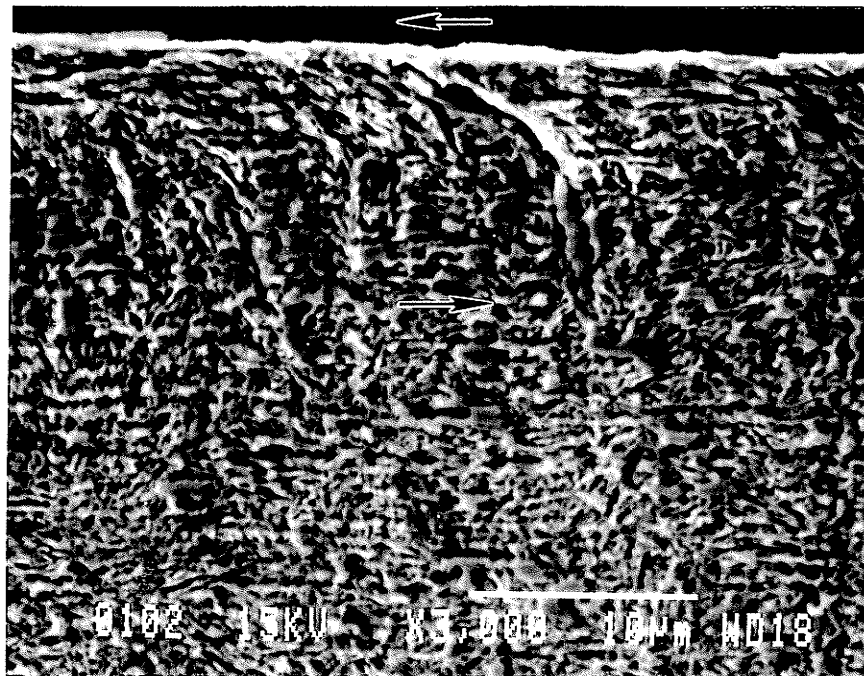


Figure 65: The etched ASB for C, -30°C.

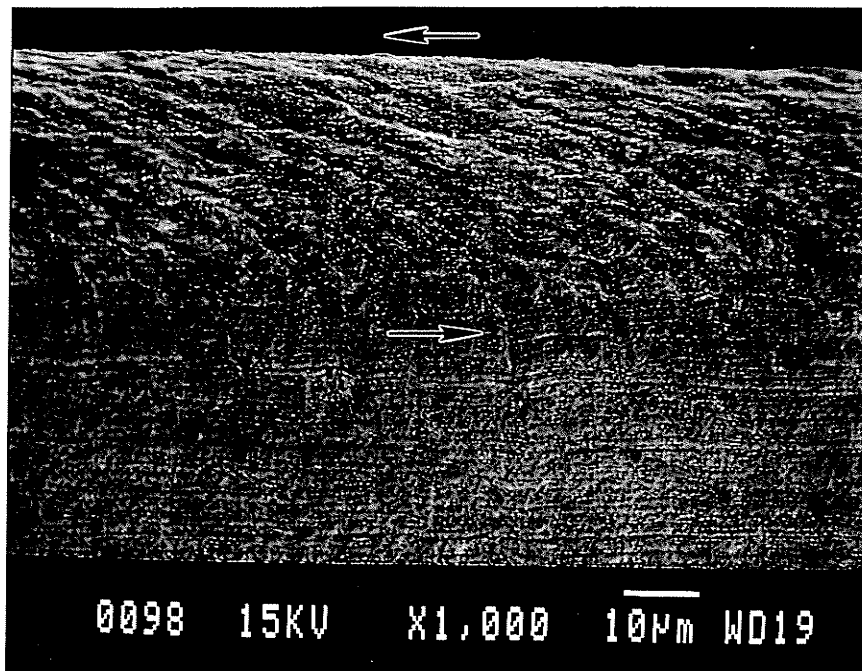


Figure 66: The etched ASB for D, -30°C.

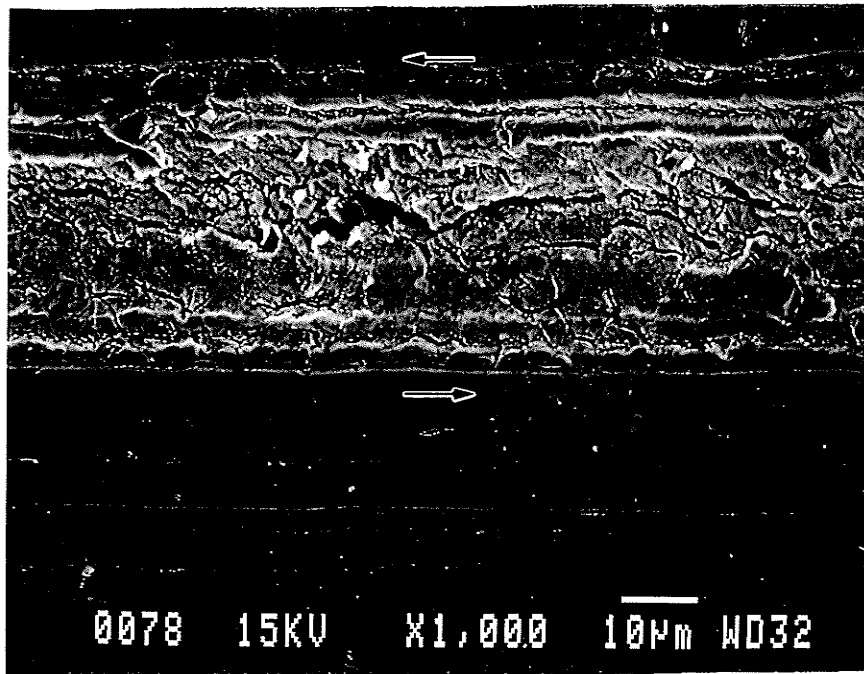


Figure 67: The etched ASB for E, -30°C.

CHAPTER 5

DISCUSSION OF RESULTS

5.1. EQUIPMENT APPRAISAL

The test apparatus functioned extremely well. Each of the tests was captured without any difficulty and periodic calibration checks revealed the system to be stable throughout the testing procedure. Post processing of the data was performed on a batch basis, meaning the acquired pulse information was consistent enough to allow the same analysis to be conducted on each set, without having to specially examine a single case.

The strain rates were all within 400 - 500 1/s and the equipment shows potential to provide higher strain rates with the modifications mentioned earlier. Generally speaking, the design and implementation of the torsional split-Hopkinson bar was a success.

5.2. YIELD CHARACTERISTICS

Examination of the stress-strain curves provided in Chapter 3 shows that, regardless of the test temperature, the behavior of the materials upon yield varied from sample to sample in a similar manner. In sample A there is a slight yield drop characteristic to stress relieved ductile materials due to the interaction of dislocation jogs. Samples B through E display continuous yielding typical to stronger or strengthened materials and progress smoothly through the elastic-plastic transition on the stress-strain curve.

5.3. HEAT TREATMENT/MICROSTRUCTURAL EFFECTS

Studying the effect of tempering temperature on shear band width, excluding the annealed and as received sample, provided the relationship shown in Figure 68. The graph shows two important pieces of information. Firstly, as the tempering temperature is increased there is an increase in the width of the observed shear band which is formed during the high strain rate test, and secondly the aforementioned effect is constant regardless of the test temperature. What this implies is that the shear band width is a property independent of test temperature, and for a given tempering condition the shear band width will remain constant over a range of test temperatures.

Another relationship which can be of interest is the effect of material hardness, regardless of microstructure, on adiabatic shear band width, Figure 69. As illustrated, with increasing hardness there is a general narrowing trend on shear band width. In addition, since the shear bands are of a constant width for a given hardness regardless of test temperature, the change in width with respect to hardness is the same for both test groups. This reiterates the independence of shear band width to test temperature.

5.3.1. Room Temperature Tests

In this section the samples have been divided into two groups, the pearlitic materials, A and B, and the martensitic materials, C, D and E. This division is based on the fact that the two groups behave differently due to the microstructures.

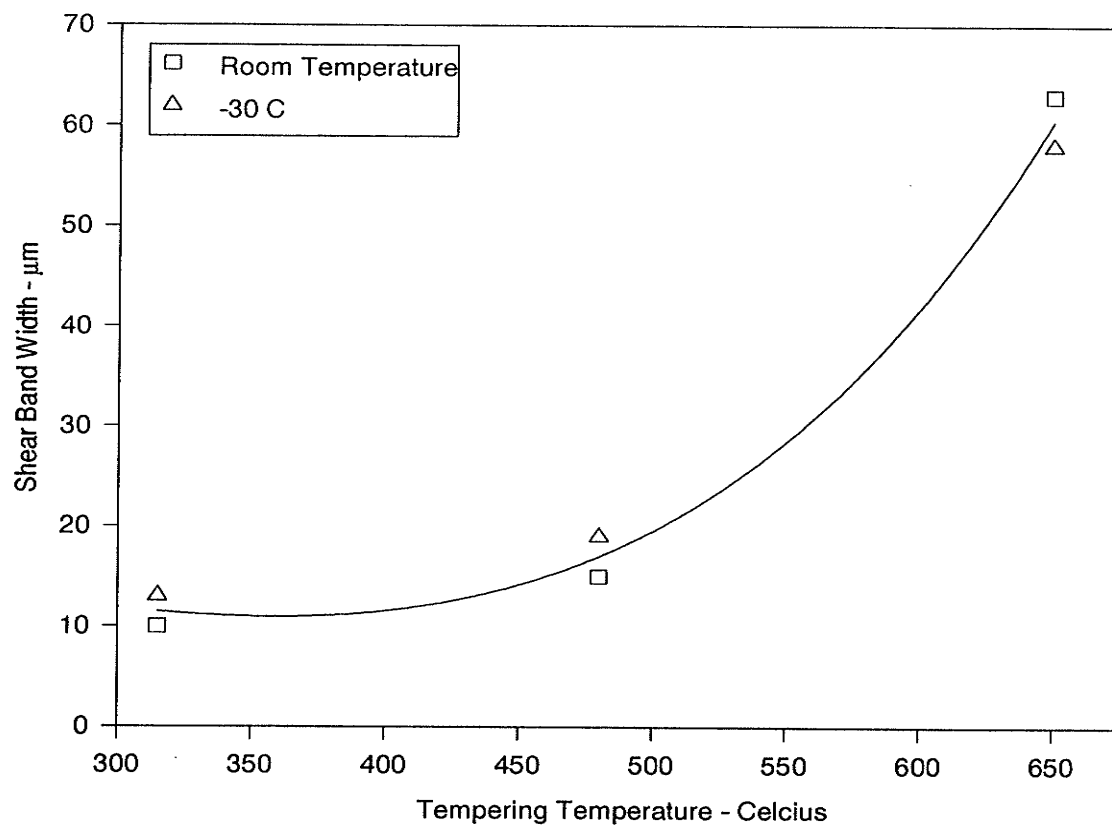


Figure 68: The effect of tempering temperature on shear band width.

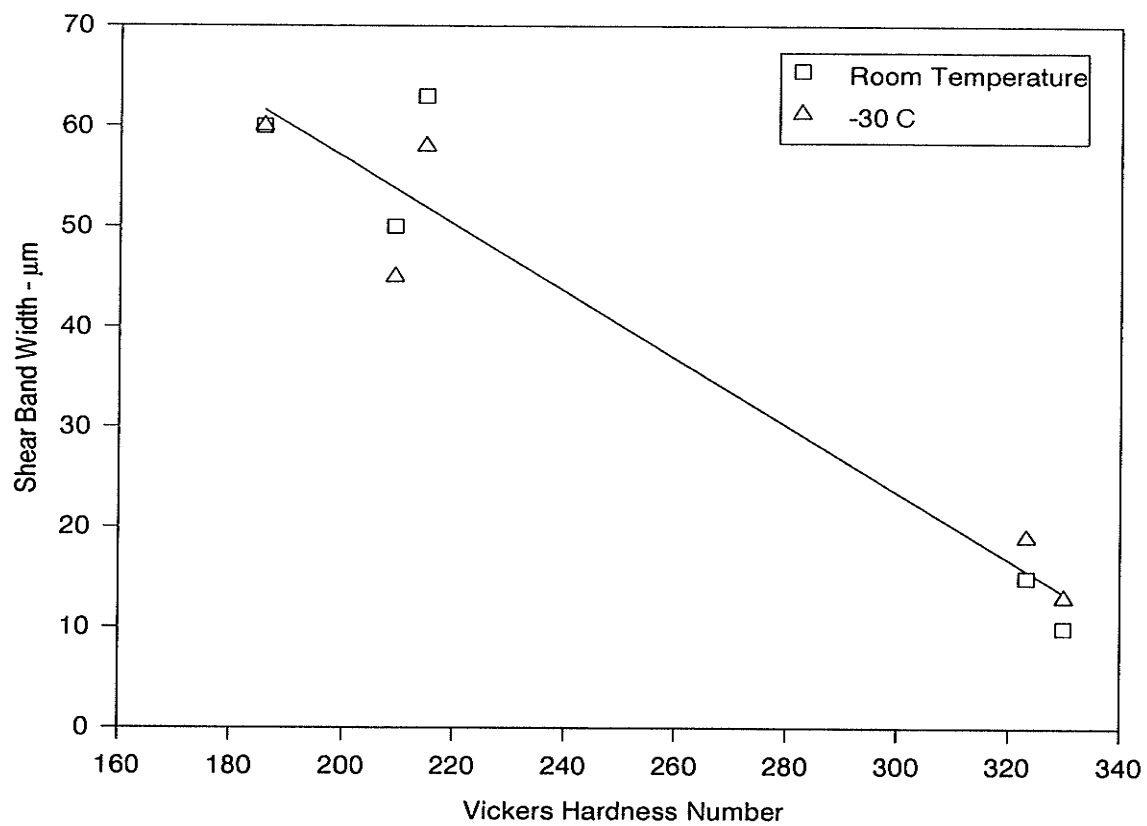


Figure 69: The effect of hardness on shear band width.

Sample A consists of typical coarse pearlite with some ferrite outlining the prior austenite grain boundaries (Figure 28). The smooth regions being ferrite. From this it can be inferred that the bar was hot rolled and slowly cooled , giving ample time for the formation of the lamellar pearlite shown. The steel with this microstructure was exhibited the lowest yield point of any of the materials tested.

Sample B portrays a microstructure indicative of a higher cooling rate than what was used in the as received stock (Figure 29) displays the microstructure of this steel showing pearlite of a very fine lamellar construction. The ferrite has formed at the prior austenite grain boundaries, similar to what is shown in Figure 28, sample A. Closer examination of the micrographs in Figures 28 and 29 reveal that the ferrite structures are very similar in appearance. The increased cooling rate did not allow for the formation of coarse lamellar pearlite. The higher cooling rate results in a finer pearlite with a hardness approximately 13% higher than was found in sample A. The cell like structures are pearlite and show resistance to the etchant while the ferrite is etched preferentially, as expected. The material had a 49% higher yield point than sample A, but at the cost of the nominal ductility reducing by 28%.

A microstructure consisting of a very fine and uniform lath type martensite with a few precipitates interspersed within the matrix is shown in Figure 30. EDS of the precipitates revealed them to be high in magnesium, aluminum and oxygen content. As is typical of martensite tempered at relatively low temperatures, the material had the highest yield point of the group and was the least ductile.

The early visible stages of recovery and recrystallization of martensite is shown in Figure 31. It appears that lath-like ferrite grains are being formed, which were visible when the microstructure was observed in the optical microscope. The micrograph shows

a coarser microstructure than the one in Figure 30, and the precipitates significantly increased in size and number. In addition, the martensitic cells appear to be increasingly segregated from each other with what is assumed to be ferrite. The overall effect on the mechanical properties is a 5% reduction in the yield strength and a 62% increase in the nominal ductility relative to sample C. In addition, the local strain decreased by 46%.

The last steel to be commented on is demonstrated in Figure 32. The trend established by samples C to D is also followed by this steel. The martensite has become very coarse and the grain boundaries compose a much larger fraction of the area than the one seen in Figure 31, corresponding to heat treatment D. In fact, the ferrite is now much more uniformly distributed throughout the matrix. The precipitates have either become very large and fallen out of the sample during preparation, or dissolved in the matrix - probably the ferritic grain boundaries. The mechanical properties fit the trend so far evident from sample C to D, E has the lowest yield strength and greatest ductility of the quenched and tempered group of samples. The relative change in E from D is a 23% decrease in yield strength and a 76% increase in sample ductility.

5.3.2. Low Temperature Tests

In this section it is convenient to change the grouping of the materials based on their original ductility rather than original microstructure. The reasoning becomes clear when considering how the materials behave under the influence of a considerably reduced testing temperature of -30°C . A and E will be in the first group with C and D in the second. B is somewhat enigmatic, and lies somewhere between the first two groups with respect to its dynamic mechanical properties at low temperatures.

Due to the fact that E was tempered at a relatively high temperature (650°C), it has been softened enough to respond similarly to A (as received) during a low temperature test. Both A and E exhibit an increase in yield strength, by 7% and 23% respectively, when tested at a temperature of -30°C as compared to the behavior at room temperature, as is expected of ductile materials [82, 83]. The interesting difference is that the nominal ductility and local strain of sample A increased by 60% and 12%, respectively, instead of dropping as is expected under the quasi-static regime. This was not the case with sample E. This anomaly may be attributed to the increased susceptibility to ASB formation, as has been observed by other researchers [2-8] and verified by the increased amount of local strain within the shear band at the low temperature test. The ASB allows greater deformation than the material would normally undergo, thereby increasing the ductility. E, in contrast, does not experience an increase in ductility, in fact its nominal ductility drops by 38%. This can be attributed to the fact that the hardening mechanism far overshadows the ASB contribution to ductility. Another possibility is the fact that the shear band in this treatment portrayed features typical of the transformed type. If this is the case, it is possible, though not verified, that the hardness of the transformed shear band was greater than the deformed shear band, and could be held accountable for the materials reduction in ductility.

The second group to analyzed consists of samples C and D, which were tempered at 315°C and 480°C. Contrary to expected behavior, the yield strength of both samples decreased, by 38% and 21% respectively, while their local ductility increased slightly, 12% for both sample C and D. The nominal ductility increased by 44% for C and decreased by 10% for sample D. Similar to the reasons cited for samples A and E, shear band formation occurs more readily in samples C and D as well. However, the effect is far more pronounced and not only results in an increase in the ductility level but affects the

yield strength adversely by causing the shear band to form at a much lower yield strength, a 38% lower for C and 21% lower for D. It is believed that the low test temperature causes a greater temperature differential to be established earlier in the test than would normally be realized at room temperature. This leads to earlier strain localization which, due to stress relaxation outside of the shear band, does not allow the material to reach its room temperature yield stress. In summary, most of the deformation process from elasticity to plasticity and finally shear banding occurs on a very localized level.

Sample type B has a microstructure responsible for standard material properties lying somewhere in between samples A and E, and C and D. The result is low temperature mechanical properties that are similar to room temperature data. The yield strength increases by 2.5% and the local strain by 3%. The most drastic change is in the nominal ductility which increases by 51% going from room temperature to -30°C tests. Tables 4 and 5 summarize the data for all of the tested samples.

5.4. SHEAR BAND CHARACTERISTICS

The first interesting aspect that becomes evident when examining Tables 4 and 5 is the fact that the width of the shear bands remained relatively constant at both of the experimental temperatures used. The second interesting finding is that the local strains, between bands, tested at the two temperatures remained essentially constant as well. This implies that for a given strain rate and a fully developed shear band, its width and local strain will remain constant regardless of the test temperature. The only anomalous point is between the room temperature and low temperature local strains for sample E. Due to the formation of what appears to be a transformed shear band, there were no deformation features that could be used to provide some indication of the strain within the shear band.

The reason for the transformed shear band forming is due to a combination of; tempered martensite increased likelihood of transforming and the additional influence of the low temperature test.

As mentioned earlier, the test temperature has no apparent effect on the width of the shear bands, however, the initial microstructure does. Figures 42 through 51 and 58 through 67 all inclusive, show the shear banded regions of each sample for the room and low temperature tests, respectively. Since the shear bands are of equal width for both the room and low temperature tests, it makes no difference which set of photos are used for reference. Generally, it can be seen that the lower ductility samples exhibited the narrowest ASB. In addition, a more uniform material microstructure results in microstructurally uniform ASB. Figures 43 and 59 are examples of highly segregated microstructures with equally inhomogeneous shear bands.

Analysis of the micrographs for sample A indicate that the presence of ferrite greatly influences both the mechanical properties and the nature of the shear band observed. The coarse pearlite structure is very rich in ferrite both within the pearlite itself and in the prior austenite grain boundaries. The post mortem micrograph shows a very fibrous, homogeneous ductile type of fracture mechanism occurring. This agrees well with the ductility expected of a coarse pearlitic material.

Sample B, as described earlier, is composed of unresolved pearlite and ferrite, of which the pearlite is much stronger. Examination of Figures 43 and 59 show what seems to be inhomogeneous intergranular deformation. The harder and stronger fine pearlite cells show more resistance to deformation than the surrounding ferrite and, thus, it is the ferrite which takes up most of the deformation of the material.

A rather large change in the ASB, was observed for sample C, when compared to the previously discussed samples A and B. This is because sample C consists of a very strong, fine martensitic structure. Examination of the shear band region shows the deformation band to be very narrow in comparison to the others, implying a lack of ductility, as well as being very uniform due to the uniform nature of the martensitic structure.

In sample D, the effects of tempering on the yield stress and ASB structure, are beginning to become much more noticeable. The previously described ferrite boundaries have begun to form and will deform preferentially over the, still very hard, martensitic cells they surround. Figure 50, which shows an etched version of the structure shown in Figure 45, supports this conclusion. Though the separation between the cells appear to be brittle type cracks, close examination reveals them to be fibrous in nature, lending credibility to the argument that the ferritic structures are responsible for the ductility of the sample.

In the sample tempered at 650°C, E , the tempering process has dramatically altered the microstructure. The presence of ferrite is far more prevalent and uniform than in sample D. For the room temperature tests the result is a shear band far more uniform and fibrous in appearance than was shown for sample D and, in fact, the most ductile sample tested. For the low temperature tests the microstructure was conducive to the formation of a transformed shear band which, apparently, cooled somewhat sooner in the test than its deformed counterpart in the room temperature tests. This resulted in an overall slightly reduced ductility.

5.5. CONSTITUTIVE MODELING

Figures 70 and 71 show the correlation between the measured shear band widths determined in the present study and predicted values according to calculations by Dodd and Bai [36]. Constants for the calculations were obtained from [36] where applicable or required. As shown in both figures, the predicted values show very good agreement with samples which developed wider and more ductile shear bands, but diverged when applied to samples of increased hardness and narrow shear bands. This result indicates that the Dodd and Bai model applies most effectively to specimens which deform within the ductile fracture regime and increases in divergence as the specimen approaches the brittle fracture regime. The graphs present shear band width as a function of material hardness and show straight line approximations through both the predicted and observed values. Ideally, the linear approximations would overlap and form a single line. The observed deviation from the ideal is greater for the -30°C test with the angle between the two lines being 37° . The deviation for the room temperature lines is 24° .

Table 7 shows the values used to obtain the predicted shear band width, the equations are detailed in [36].

Table 7: Data used for calculation of the Shear Band Width.

Test Temp.	Test Sample	Measured Width, μm	Calculated Width, μm	Flow Stress, MPa	Thermal Cond., W/mK	Coeff. Visc., kg/ms	T _m , K
room temp							
	A	60	56	535	50.191	2450	1800
	B	50	49	613	50.191	2450	1800
	C	10	44	675	50.191	2450	1800
	D	15	46	640	50.191	2450	1800
	E	63	57	520	50.191	2450	1800
-30°C							
	A	60	52	575	50.191	2450	1800
	B	45	50	598	50.191	2450	1800
	C	13	61	490	50.191	2450	1800
	D	19	56	530	50.191	2450	1800
	E	58	46	640	50.191	2450	1800

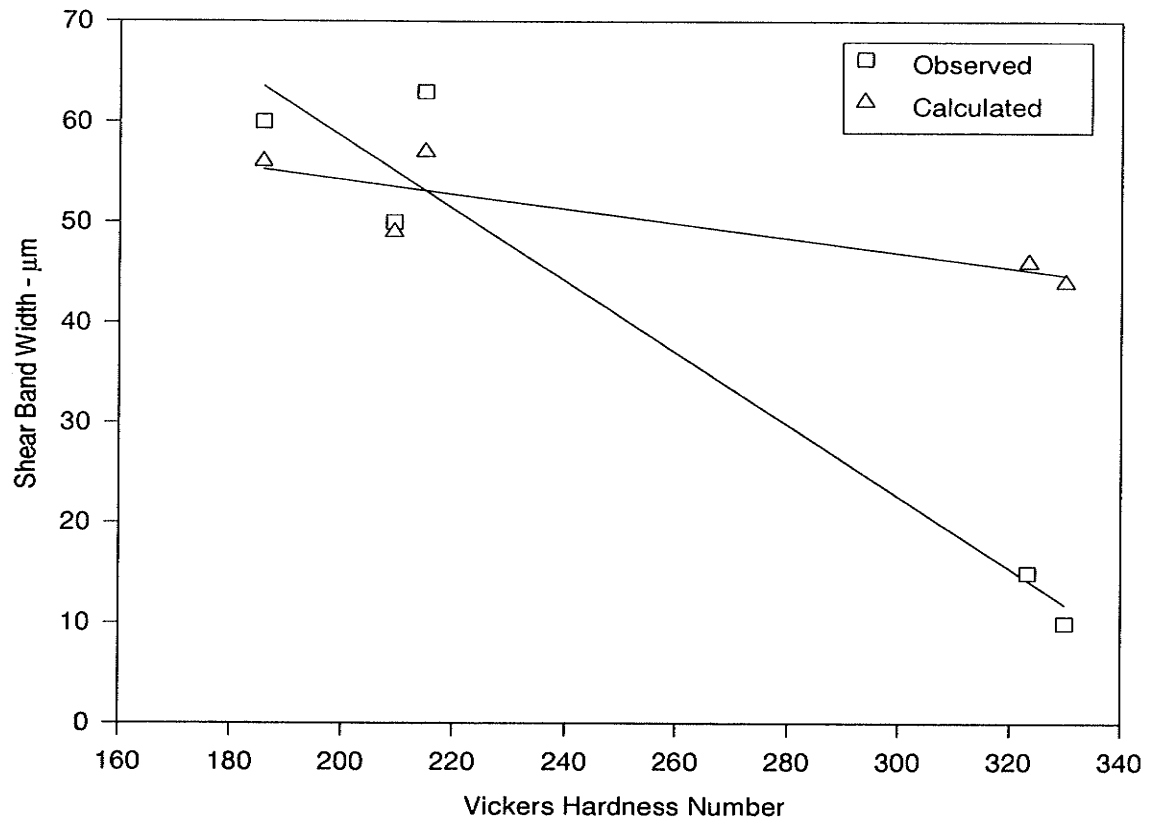


Figure 70: Room temperature correlation with Dodd and Bai's model.

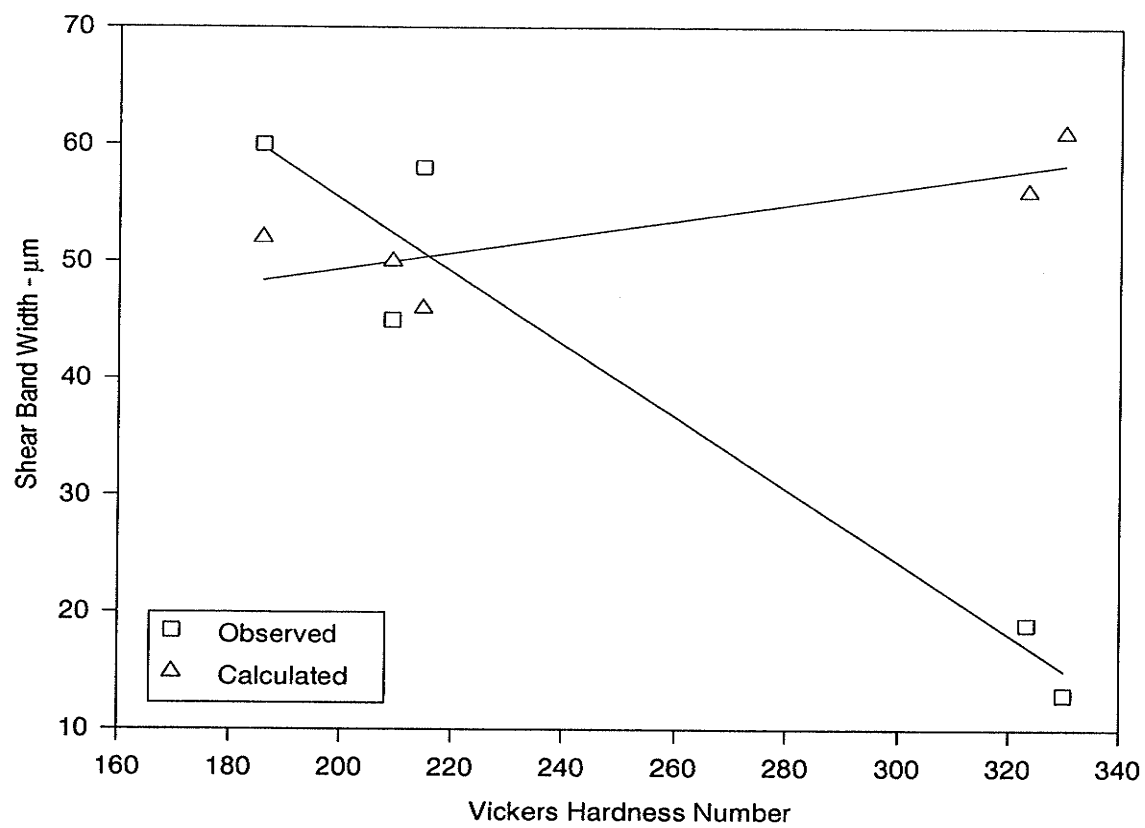


Figure 71: -30°C correlation with Dodd and Bai

CHAPTER 6

CONCLUSIONS

The major objective of this research project was to design and construct a torsionally modified split-Hopkinson bar which would be capable of conducting high strain rate tests. Following this, verification of the equipment performance was to be conducted through a series of tests on SPS-Plus steel. The resulting widths of the adiabatic shear bands obtained through the high strain rate tests were determined and related to the various material conditions and experimental variables used in this study.

Based on the results presented within this thesis, the following conclusions can be drawn:

1. The designed and built apparatus is reliable, simple to use and provides consistent results.
2. The general shape of the stress-strain curves is not affected by the heat treatment condition of the material studied.
3. An increase in the yield strength of the material results in a decrease of the width of the adiabatic shear band observed on the surface of the specimens tested at high strain rates, regardless of the test temperature.
4. The adiabatic shear band increases in width as the martensite tempering temperature increases, at both room temperature and -30°C test conditions.
5. There is a good correlation between the adiabatic shear band widths as measured in this study and the predicted widths based on Dodd and Bai's

model for materials which deformed in the ductile fracture regime. Brittle materials such as samples B and C diverged considerably and suggest that the Dodd and Bai model is most effective on ductile materials.

6. An increase in material hardness results in a reduced failure strain percentage, regardless of the test temperature.
7. Deformed shear bands portrayed stretch or strain lines as opposed to transformed shear bands. In a pearlitic structure, deformation occurred mainly in the ferrite resulting in a cellular appearance in the banded region. Martensitic microstructures were associated with shear bands that appeared markedly different than the surrounding matrix and could not provide local deformation information. The appearance consisted of a discretely bound network of cracks.

For future work it is recommended that replacement of the 6061-T6 aluminum bar with a 7075-T6 aluminum bar be executed to allow higher strain rate testing than is currently being realized. As well, additional modification of the machinery to allow quasi-static testing would be beneficial for studies over a wide range of strain rates.

A detailed study of martensitic steel should also be conducted in order to obtain more data in regarding the effect of tempering temperature and the subsequent effects on shear band formation, without the difficulty of dealing with a multitude of microstructures.

REFERENCES

- [1] Turley D.M., Doyle E.D. and Ramalingam S., *Materials Science and Engineering* **55** (1982) 45-48.
- [2] Lemaire J.C. and Backofen W.A., *Metallurgical Transactions*, **3** (1972) 477-481.
- [3] Dao K.C. and Shockey D.A., *Metallurgical Transactions*, **50** (1979) 8244-8246.
- [4] Itahara, M. *Impact Torsion Tests*, Technical Reports of Tohoku Imp. University, **9**, 16, **11**, 512 and **12** 173 (1933-35).
- [5] Hartley K.A., Duffy J. and Hawley R.H., *J.Mech.Phys.Solids*, **35** (1987) 283-301.
- [6] Backman M.E. and Finnegan S.A., *Metallurgical Effects at High Rates of Strain* (Plenum Press, New York, 1973) pp. 531-543.
- [7] Costin L.S., Crisman E.E., Hawley R.H. and Duffy J., *Inst.Phys.Conf.Ser.*, **47** (1979) 90-100.
- [8] Senseny P.E., Duffy J. and Hawley R.H., *Journal of Applied Mechanics*, **45** (1978) 60-66.
- [9] Olson G., Mescall J.F. and Azrin M., *Shock Waves and High Strain Rate Phenomena in Metals* (Plenum Press, New York, 1981) pp 221-247.
- [10] Rogers H.C. and Shastry C.V., *Shock Waves and High Strain Rate Phenomena in Metals* (Plenum Press, New York, 1981) pp 285-298.
- [11] Marchand A. and Duffy J., *J. Mech. Phys. Solids*, **36**, (1988), 251-83.
- [12] Semiatin S.L., Staker M.R. and Jonas J.J., *Acta Metallurgica*, **32**, (1984), 1347-1354.
- [13] Batra R.C., *Int. J. Solids Structures*, **23**, (1987), 1435-1446.
- [14] Staker M.R., *Acta Metallurgica*, **29**, (1981), 683-689.
- [15] Merzer A.M., *J. Mech. Phys. Solids*, **30**, (1982), 323-338.
- [16] Lewis, J.L. and Campbell J.D. *Experimental Mechanics*, **12**, (1972), 520-524.

- [17] Grady, D.E., *Metallurgical Transactions*, (1991), 1197-1215
- [18] Batra, R.C. and Kim, C.H., *International Journal of Plasticity*, **6**, (1990), 127-141.
- [19] Baron, H.G., *J. Iron and Steel Institute*, **182**, (1956), 354.
- [20] Bai Y.L., *J. Mech. Phys. Solids*, **30**, (1982), 195.
- [21] Campbell J.D., *Material Science and Engineering*, **12**, (1973), 3.
- [22] Nakkalil R., Hornaday J.R. and Bassim M.N., *Materials Science and Engineering*, **A141**, (1991) 247-260.
- [23] Wang L.L., Lu W.X., Hu S.S. and Tang Z.P., *Study of the Initiation and Development of Adiabatic Shear Bands for a Titanium Alloy under High Strain Rates*, IUTAM Symposium Tokyo/Japan, 1985, pp 395-406.
- [24] Timothy S.P., *Acta Metallurgica.*, **35**, 2 (1987) 301-306.
- [25] Nicholas T. and Bless S.J., in *Metals Handbook 9th Ed. Volume 8: Mechanical Testing*. ASM, Metals Park, Ohio. (1985) 208-214.
- [26] Cho, K., Chi Y.C. and Duffy J., *Metallurgical Transactions*, **21A** (1990) 1161-1175.
- [27] Cepus E., Liu C.D. and Bassim M.N., *DYMAT '94 Conference Proceedings*, to be published September 1994.
- [28] Samuels L.E. and Lamborn I.R., *Metallography of Failure Analysis*, (edited by McCall J.L. and French P.M.) Plenum Press, New York, (1978) 167.
- [29] Manion S.A. and Stock T.A., *J.Aust.Inst.Metals*, **14**, (1969) 190.
- [30] Timothy S.P. and Hutchings I.M., *Acta Metallurgica*, **33** (1985) 667.
- [31] Zener C. and Holloman J.H., *J.Appl.Phys.*, **15**, (1944) 22.
- [32] Wingrove A.L., *Metallurgical Transactions*, **4**, (1973) 1829.
- [33] Bhambri A.K., *Microstructr.Sci.*, **7**, (1979) 255.
- [34] Turley D.M., Doyle E.D. and Ramalingham S., *Mater.Sci.Engng.*, **55**, (1982) 45.

- [35] Moss G.L., in *Shock Waves and High Strain Rate Phenomena* (edited by M.A. Meyers and L.E. Murr), Plenum Press, New York (1981) 299.
- [36] Dodd B. and Bai Y., *Materials Science and Technology*, **1** (1985) 38-40.
- [37] Backman M.E., *Damage Mechanisms and Terminal Ballistics Research*, NWC TP 4835, Naval Weapons Centre, China Lake, Calif. (1969).
- [38] Bedford A.J, Wingrove A.L. and Thompson K.R.L., *J.Aust.Inst.Metals*, **19**, (1974) 61.
- [39] Rogers H.C., *Adiabatic Shearing: A Review*, Drexel University Report prepared for U.S. Army Research Office (1974).
- [40] Rogers H.C., *Ann.Rev.Mater.Sci.*, **9**, (1979) 283.
- [41] Rogers H.C., in *Material Behaviour under High Stress and Ultrahigh Loading Rates* (eds. J. Mescall and V. Weiss) Plenum Press, New York, (1983) 101.
- [42] Rogers H.C., *Deformation, Processing and Structure* (ed. G. Krauss) ASM, Metals Park, Ohio, (1984) 425.
- [43] Timothy S.P. and Hutchings I.M., in *Proc. 3rd Int. Conf. on Mechanical Properties of Materials at High Rates of Strain* (ed. J. Harding) Institute of Physics, Bristol, (1984) 397.
- [44] McIntire H.O. and Manning G.K., *Metals Prog.*, **74** (1958), 94.
- [45] Stock T.A.C. and Thompson K.R.L., *Metallurgical Transactions*, **1**, (1970), 219.
- [46] Irwin G.J., *Metallographic Interpretations of Impacted Ogive Penetrators*, DREV-R-652/72, Defense Research Establishment, Valcartier, Quebec (1972).
- [47] Seaman L., Shockey D.A., Curran D.R. and Tokheim R.E., *Development of a Shear Band Model for Fragmentation in Exploding Cylinders*, Stanford Research Institute Report, S.R.I., Menlo Park, Calif., (1975).
- [48] Winter R.E., *Phil. Mag.*, **31**, (1975), 765.
- [49] Christman T. and Shewmon P.G., *Wear*, **54**, (1979), 145.
- [50] Kunze H.D., Hartmann K.H. and Rickel J., *Prak. Metallogr.*, **18**, (1981), 261.

- [51] Stelly M., Legrand J. and Dorneval R., in *Shock Waves and High Strain Rate Phenomena* (edited by M.A. Meyers and L.E. Murr), Plenum Press, New York (1981) 113.
- [52] Timothy S.P. and Hutchings I.M., *Proc. 7th Int. Conf. on High Energy Rate Fabrication*, (ed. Blazynski T.Z.) Leeds, (1981), 19.
- [53] Timothy S.P. and Hutchings I.M., in *High Energy Rate Fabrication - 1984*, (eds. Berman I. and Shroeder J.W.), A.S.M.E., New York, (1984), 31.
- [54] Timothy S.P. and Hutchings I.M., *J. Mater. Sci. Letters*, **5**, (1986), 453.
- [55] Me-Bar Y. and Shechtman D., *Mater. Sci. Engng.*, **58**, (1983), 181.
- [56] Dao K.C. and Shockey D.A., *J. Appl. Phys.*, **50**, (1979), 8244.
- [57] Duffy J., *Mechanics of Material Behaviour*, The Daniel C Drucker Anniversary Volume, Elsevier, Amsterdam, (1984), 75.
- [58] Glenn R.C. and Leslie W.C., *Metallurgical Transactions*, **2**, (1971), 2945-2947.
- [59] Thornton P.A. and Heiser F.A., *Metallurgical Transactions*, **2**, (1971), 1496-1499.
- [60] Recht R.F., *J. Appl. Mech. Trans.*, A.S.M.E., **31**, (1964), 189.
- [61] Culver R.S., in *Metallurgical Effects at High Strain Rates*, (eds. R.W. Rhode *et al*), Plenum Press, New York, (1973), 519-530.
- [62] Yellup J.M. and Woodward R.L., *Res. Mechanica*, **1**, (1980), 41.
- [63] Leech P.W., *Metallurgical Transactions*, **16A**, (1985), 1900.
- [64] Ansart J.P., in *Proc. Int. Conf. on Fragmentation, Form and Flow in Fractured Media*, Neve Ilan, Israel, (1986), 1986.
- [65] Wittman C.L., Meyers M.A. and Pak H.-r., *Metallurgical Transactions*, **21A**, (1990), 707-716.
- [66] Wingrove A.L., *J. Aust. Inst. Metals*, **16**, (1971), 67.
- [67] Derop J.L., *Acta Metallurgica*, **35**, (1987), 1245-1249.

- [68] Manion S.A. and Stock T.A.C., *Int Journal of Fracture Mechanics*, **6**, (1970), 106-107.
- [69] Doraivelu S.M., Gopinathan V. and Venkatesh V.C., in *Shock Waves and High Strain Rate Phenomena* (edited by M.A. Meyers and L.E. Murr), Plenum Press, New York (1981) 263-275.
- [70] Merzer A. and Bodner S.R., *Mechanical Properties at High Rates of Strain*, (ed. J.Harding), The Institute of Physics, London, (1979), 142-151.
- [71] Craig J.V. and Stock T.A.C., *J. Aust. Inst. Met.*, **15**, (1970), 1-5.
- [72] Smith W.F., *Structure and Properties of Engineering Alloys*, McGraw-Hill, New York, (1981), 25-32.
- [73] Fullingham P.J., Leary H.J. and Turner L.E., in *Electron Microscopy and Structure of Metals*, (ed. G. Thomas), University of California Press, Berkely, Calif., (1972), 163-72.
- [74] Wright T.W., *J. Mech. Phys. Solids*, **25**, (1987), 269-282.
- [75] Kolsky H., *Proc. Phys. Soc.*, **62B**, (1949), 676.
- [76] Hartley K.A., Duffy J. and Hawley R.H., in *Metals Handbook 9th Ed. Volume 8: Mechanical Testing*. ASM, Metals Park, Ohio. (1985) 218-239.
- [77] Lindholm U.S., *Mech Phys. Solids*, **12**, (1964) 317-335.
- [78] *Handbook of Chemistry and Physics 53rd Edition*, (ed. R.C. Weast), The Chemical Rubber Company, Cleveland Ohio, (1972), E-41.
- [79] *Mark's Standard Handbook for Mechanical Engineers 9th edition*, (eds. E.A. Avallone and T Baumeister III), McGraw-Hill, New York, (1987), 3-26.
- [80] Samuels L.E., *Optical Microscopy of Carbon Steels* (American Society for Metals, Metals Park, 1980) pg. 169.
- [81] Samuels L.E., *Optical Microscopy of Carbon Steels* (American Society for Metals, Metals Park, 1980) pg. 375.
- [82] Dieter G.E., *Mechanical Metallurgy 3rd Edition*, McGraw-Hill, New York (1986), 476-482.

- [83] Van Vlack L.H., *Elements of Materials Science and Engineering 6th Edition*, Addison-Wesley, New York, (1989), 272-274.
- [84] Beer F.P. and Johnston, Jr. E.R.. *Mechanics of Materials*. McGraw-Hill, New York, (1981) p 97.
- [85] Zukas, S.I. *Impact Dynamics*, Addison-Wesley, New York, (1981).